LUND UNIVERSITY

On the Phase Behaviour of Soft Matter: Understanding Complex Interactions via Quantitative Imaging

Bergman, Maxime

2019

Link to publication

Citation for published version (APA):
Bergman, M. (2019). *On the Phase Behaviour of Soft Matter: Understanding Complex Interactions via Quantitative Imaging*. [Doctoral Thesis (compilation), Department of Chemistry]. Lund University, Faculty of Science, Department of Chemistry.

Total number of authors:
1

LUND UNIVERSITY

PO Box 117
221 00 Lund
+46 46-222 00 00

On the Phase Behaviour of Soft Matter: Understanding Complex Interactions via Quantitative Imaging

MAXIME BERGMAN | PHYSICAL CHEMISTRY | LUND UNIVERSITY

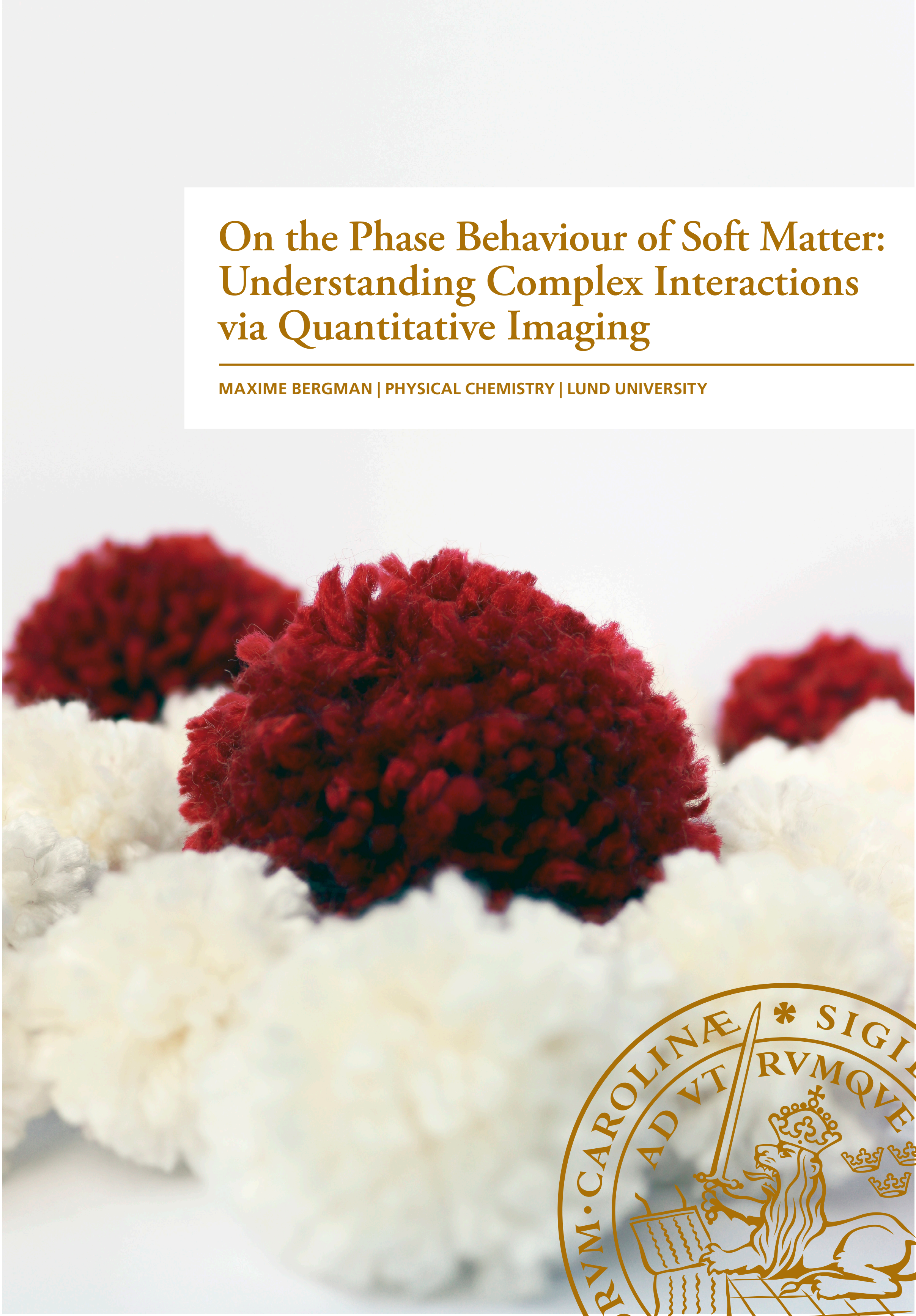

On the Phase Behaviour of Soft Matter: Understanding Complex Interactions via Quantitative Imaging

by Maxime J. Bergman

LUND
UNIVERSITY

Doctoral Dissertation

by due permission of the Faculty of Science at Lund University.
To be defended on Thursday, the 14th of March 2019 at 10:00 in lecture hall B at the Centre for Chemistry and Chemical Engineering at Lund University.

Faculty opponent

Prof. Thomas Hellweg
Bielefeld University, Bielefeld, Germany

Organization
LUND UNIVERSITY
Division of Physical Chemistry
Box 124
SE–221 00 LUND
Sweden

Document name
DOCTORAL DISSERTATION

Date of disputation
2019-03-14

Sponsoring organizations
European Research Council (ERC)

Author(s)
Maxime J. Bergman

Title and subtitle
On the Phase Behaviour of Soft Matter: Understanding Complex Interactions via Quantitative Imaging

Abstract

The effect of microscopic colloid interactions on the resultant macroscopic phase behaviour is a frequently studied topic in soft matter resarch, and lies at the heart of this thesis. Key structural and dynamic properties of colloidal model systems across liquid-solid transitions are tracked using optical imaging techniques.

The first studied system comprises of thermosensitive microgels. These are soft, crosslinked polymer networks of colloidal size, which have been used as model systems to investigate various phase transitions. They display a rich phase behaviour due to their soft potential and internal core-corona structure. Especially, their thermosensitivity allows us to use temperature as an external control to tune particle size, volume fraction and effective interaction potential in situ. However, a thorough understanding of the effective interactions between microgels is lacking, and constitutes a key research question in this thesis.

We therefore quantitatively compare experimental and numerical pair correlation functions (g(r)s) across the phase diagram, obtained from confocal microscopy and simulations. We find that neutral, swollen microgel interactions are temperature-dependent, but also hinge on whether the core or corona of the microgel is explored.

This approach is repeated for ionic microgels with varying crosslinker density, where the introduction of acrylic acid complicates the resultant swelling behaviour. For this reason, we start by decoupling the core and corona swelling response to various charge regimes via light scattering experiments, and found that dangling polymer strands can extend up to several 100 nm outside of the network. Dangling ends had a pronounced effect on the interactions and phase behaviour of ionic microgels, but their contribution is missing within the current theoretical framework.

Finally, liquid-solid transitions in concentrated protein solutions are investigated. Two well studied globular proteins, lysozyme and γ_B-crystallin, were used as model systems with completely different interactions. No unambiguous experimental demonstration of the existence of an arrested glassy state had been published so far for either protein. A combination of two passive microrheology techniques now allowed us to confirm the formation of a glass phase at concentrations above a critical arrest concentration, and to obtain quantitative insight into the concentration dependence of the zero shear viscosity prior to arrest.

Key words
microgels, proteins, phase behaviour, confocal microscopy, interaction potential

Classification system and/or index terms (if any)

Supplementary bibliographical information

Language
English

ISSN and key title

ISBN
978-91-7422-626-3 (print)
978-91-7422-627-0 (pdf)

Recipient's notes

Number of pages
270

Price

Security classification

I, the undersigned, being the copyright owner of the abstract of the above-mentioned dissertation, hereby grant to all reference sources the permission to publish and disseminate the abstract of the above-mentioned dissertation.

Signature

Date 2019-02-04

DOKUMENTDATABLAD enl SIS 61 41 21

On the Phase Behaviour of Soft Matter: Understanding Complex Interactions via Quantitative Imaging

by Maxime J. Bergman

LUND
UNIVERSITY

A doctoral thesis at a university in Sweden takes either the form of a single, cohesive research study (monograph) or a summary of research papers (compilation thesis), which the doctoral student has written alone or together with one or several other author(s).

In the latter case the thesis consists of two parts. An introductory text puts the research work into context and summarizes the main points of the papers. Then, the research publications themselves are reproduced, together with a description of the individual contributions of the authors. The research papers may either have been already published or are manuscripts at various stages (in press, submitted, or in draft).

Cover illustration front: A mixture of large fluorescently labeled microgels in a sea of tiny unstained microgels (with some artistic license).

Funding information: The thesis work was financially supported by the European Research Council (ERC-339678-COMPASS grant).

Faculty of Science at Lund University, Division of Physical Chemistry

ISBN: 978-91-7422-626-3 (print)
ISBN: 978-91-7422-627-0 (pdf)

Printed in Sweden by Media-Tryck, Lund University, Lund 2019

Contents

List of publications

This thesis is based on the following publications,
referred to by their Roman numerals:

I **A new look at effective interactions between microgel particles**
M. J. Bergman, N. Gnan, M. Obiols-Rabasa, J-M. Meijer, L. Rovigatti, E. Zaccarelli and P. Schurtenberger
Nature Communications 9.1 (2018): 5039.

II **Interactions in dense microgel systems**
M. J. Bergman, E. Zaccarelli and P. Schurtenberger
Manuscript in preparation

III **In silico synthesis of microgels**
N. Gnan, L. Rovigatti, **M. Bergman** and E. Zaccarelli
Macromolecules, 50(21), pp.8777-8786.

IV **Morphologies of charge-regulating ionic microgels**
M. J. Bergman*, J. S. Pedersen, P. Schurtenberger and N. Boon*
Manuscript in preparation

V **On the role of softness in ionic microgel interactions**
M. J. Bergman*, S. Nöjd*, P. S. Mohanty, N. Boon, J. N. Immink, J. J. E. Maris, J. Stenhammar and P. Schurtenberger
Manuscript in preparation

VI **Experimental evidence for a cluster glass transition in concentrated lysozyme solutions**
M. J. Bergman*, T. Garting*, P. Schurtenberger and A. Stradner
Under revision at J. Phys. Chem. B.

VII **Dynamical arrest for globular proteins with patchy attractions**
T. Garting*, **M. J. Bergman***, P. Schurtenberger and A. Stradner
Manuscript in preparation

* these authors contributed equally. All papers are reproduced with permission of their respective publishers.

Author contributions

Paper i: A new look at effective interactions between microgel particles

EZ and PS designed and supervised research. MB performed all experiments with help from MOR and JMM. MB, NG, LR and EZ performed simulations and modeling. All authors contributed to the interpretation and analysis of the data. MB, EZ, LR and PS wrote the manuscript with inputs from all other authors.

Paper ii: Interactions in dense microgel systems

PS designed the study and supervised research. MB did all experimental work. MB ran all simulations with help from EZ. MB wrote the manuscript with input from all other authors.

Paper iii: In silico synthesis of microgels

EZ designed the study and supervised research. Development of the simulations approach was performed by NG, LR and EZ. MB was responsible for the light scattering experiments. NG, LR and EZ wrote the manuscript with input from MB.

Paper iv: Morphologies of charge-regulating ionic microgels

NB, MB and PS designed the study and PS supervised research. NB and MB developed the Mie scattering scripts. MB was responsible for all experimental work. NB developed the theoretical model. All authors contributed to the interpretation and analysis of the data. MB and NB wrote the manuscript with input from PS.

Paper v: On the role of softness in ionic microgel interactions

PS designed the study and supervised research. SN synthesised all microgels and performed light scattering experiments. SN performed microscopy experiments together with PM and MB. MB was responsible for image analysis. MB ran simulations with help from JI, JM and JS and calculations with help from NB. MB wrote this manuscript with input from SN and all other co-authors.

Paper vi: Experimental evidence for a cluster glass transition in concentrated lysozyme solutions

AS and PS designed the study and supervised research. MB was responsible for confocal microscopy. TG performed all DLS microrheology. MB and TG wrote the manuscript with input from all authors.

Paper vii: Dynamical arrest for globular proteins with patchy attractions

AS and PS designed the study and supervised research. MB was responsible for confocal microscopy. TG performed all DLS microrheology. MB and TG wrote the manuscript with input from all authors.

Acknowledgements

My warmest thanks to my main supervisor Peter for providing me with this opportunity. I have learnt so much about myself and about science in these last four years. You have taught me a lot about how science works and how exciting it can be.

Emanuela and Janne-Mieke, you are my inspirations. This booklet would not be here if it wasn't for you. You made a real impact on how I want to be, both in terms of personal and scientific attitude.

Janne-Mieke, I still remember the first day you came into the office and how you were helping me understand image analysis within the first hour. I learnt more that day than I had in all the months leading up to it. I cannot thank you enough for your patience and neverending willingness to answer my questions and to help me think critically about my research.

Emanuela, it has been such a pleasure to collaborate with you and share ideas. Spending one month in Rome working on simulations was an absolute highlight and I remember it fondly (and not just because of the research). The way you do research has been an eye-opener for me and I am honoured to have you as my co-supervisor.

My sincerest thanks also to my co-supervisor of the earliest hour, Johan, for always signing my individual study plans without fail. We had some inspiring discussions, which helped me to get new perspectives and ideas when I needed it most.

I extend my thanks to all my collaborators, past and present: Niels, Sofi, Marc, Priti, Jasper, Nicoletta, Lorenzo, Tommy, Anna, Joakim. Together we made some real science. My thanks also to all the people at the Physical Chemistry division, especially to Helena, Maria S., Chris H. and Chris W. - you make it seem so *easy*.

A huge thank you to Peter, Tommy, Jasper, Sofi, Niels, Joakim and Emanuela for helping me to write and proofread the contents of this work - your help was immensely appreciated! And Tommy and Niels, I cannot believe all these fun 'Friday afternoon' projects turned into so much work. What happened there.

A special thank you to Marc for introducing me to the Physical Chemistry division and for setting me on the right path when I started out with my internship. The road you have set me upon has lead to many wonderful things and I cannot thank you enough for your guidance and support in the early years.

I'm also grateful to have shared so much laughs and discussion in the office over the past few years - thank you to Linda, Janne-Mieke, Erik, Adriana, Brijitta, and all of our plants for brightening the air and lifting the spirits. It's been four years, Linda, and I still can't get enough of you!

Maria, Jasper, Tommy, Linda and Feifei, we followed the same path and doing it together always brought me comfort. Thank you for sharing this time in the PhD 'rollercoaster'. How fun was it to compare deadlines and nightmares?! (maybe not so much)

João, Marta, Polina, Maria, Jordi, Jasper, Joël, Bathrobes group, the past few years wouldn't have been half as fun without you. Thank you for all the dinners, drinks, dinners, drinks, and dinners. And let's not forget the sunny dinners and drinks in various places across the world.

Marieke, Suus, Janine, Erik, Jan-Maarten, Remco, Maja, thanks for being such a bunch of pannenkoeken. Glad to know I'm in good company and I can't wait to do it again.

Joël, thanks for always pressuring me to do the things I love. Couldn't have done it without you. Also thanks for all the cheese. That was a real motivator.

To my parents and my brother, thanks for always being there when I need you.

Popular summary

A first lesson in physical chemistry invariably starts with an example of water existing in three states, or phases - gaseous (water vapour), liquid (water from the tap) and solid (ice cubes). Such phase transitions are easily observed, but their underlying cause is not so evident. Atoms and molecules are difficult to follow due to their minute size and rapid movements. So, in order to investigate phase transitions, so-called colloids are often employed. Colloids are tiny particles ranging between 1-1000nm in size: their size is large enough, and their dynamics are slow enough to be detectable with various instruments, yet at the same time, their motion and interactions still resemble molecules and atoms. Like magnets, interactions can either cause colloids to move away from each other (repulsive interactions) or draw closer to each other (attractive interactions). The microscopic interactions between colloids drive their macroscopic phase transitions, and so by investigating the phase behaviour of colloids with different interactions, we can learn more about what triggers phase transitions in atomistic and molecular matter. In recent years, the phases and phase transitions of increasingly complex colloids have been researched.

My thesis follows suit, and focuses on two vastly different systems, for which we try to predict phase behaviour based on the interactions between the colloids. The first system consists of so-called microgels, which are tiny, soft polymer networks. The microgel is comparable to a microscopic sponge saturated with water, which can be squeezed (relatively) dry. Changes in sample environment, for example an increased temperature, will lead to the squeezing out of water, which can also be done via the packing of many microgels in a small space. A swollen microgel softly repulses its neighbour, while a so-called collapsed microgel, i.e. a compressed sponge, experiences attractions. As a result, the macroscopic behaviour of a microgel sample will change significantly as the temperature is increased. The aim of my thesis is to find a model which correctly predicts the interactions between microgels as a function of temperature and packing fraction.

The second leg of my thesis revolves around the interactions and phase behaviour of two proteins, lysozyme and γ_B-crystallin, which occur naturally in the body. Proteins - consisting of many different amino acids, each with their own specific interactions - can be considered as very complex colloids. A recurring theme in physical chemistry is therefore the attempt to describe proteins with models based on simpler colloids. In the absence of salt, lysozyme is slightly attractive but mainly repulsive, and these mixed interactions leads to the formation of clusters. There is an ongoing debate whether these clusters will eventually jam and stop moving with increasing protein concentration, i.e. transitions from a liquid state into a solid one. γ_B-crystallin possesses attractive patches on its surface. Under physiological conditions, these patches dominate its phase behaviour and at high enough concentration, a network is formed. Any simple colloid with an overall attractiveness - as opposed to patches - would not form such a network. Predictive theories describing at what concentrations such patchy particles will arrest, and how the concentration affects the macroscopic viscosity, are not readily available. The second aim of my thesis is therefore to experimentally explore the liquid-solid transitions for these two proteins.

1 | Introduction

1.1 A state of being

Atoms and molecules are the building blocks of the physical world. Their particular (dis)order on the microscopic scale leads to various macroscopic phases. A simple example is crystal formation of water upon freezing: with decreasing temperature, the molecules arrange in an orderly fashion as it is energetically favourable. However, the driving force behind some phase behaviours remains an open question. For example, it is unknown how the composition of multiple constituents in metal alloys sparks changes in load-bearing capacities (see for example Ref. (1)). There is a strong link between the interactions on a single-atom level, and the resultant phase properties of the macroscopic matter. Clearly in this case it would be convenient to know which interactions govern the phase behaviour, as predictions of the strongest alloys are easier than trial-and-error.

Unfortunately, experiments on the nanoscale are challenging. Instead, physical chemists employ colloids, which are defined as particles with a size between 1-1000 nm, as model systems. Colloids are still affected by thermal motion - and so behave similarly to atoms and molecules - but in contrast, since they are much larger and move much slower, the relevant length and time scales are much more easily accessible in experiments (2). They can conveniently be monitored and tracked using optical imaging techniques such as confocal laser scanning microscopy *in-situ* and in real time, and the interaction potential between the particles can be varied greatly and quite easily. The idea of colloids as big atoms was first introduced in the 80's in the seminal work by Pusey and Van Meegen, and has gained traction ever since (3).

The focus of this thesis lies on the interplay between microscopic interactions and macroscopic phase behaviour of soft colloidal matter. Two types of colloids are under scrutiny: (I) the so-called microgels and (II) proteins. The aim of this thesis - in the case of the microgels - is to link the experimentally observed phase behaviour to proposed interaction potentials, where a strong effect from the particle architecture on interactions is expected. In the case of the proteins, the aim is to map how underlying interactions alter the (debated) phase transitions, and trace this back to colloidal theory. The rest of this introduction is therefore devoted to a short description of the phase diagram for hard spheres (Section 1.2) and identifying key knowledge gaps in microgel research (Section 1.3) and protein research (Section 1.4).

1.2 The hard sphere paradigm

Hard spheres can be considered the cornerstone of colloidal research; these 'ideal' particles experience zero interactions, until contact, where the repulsion becomes infinite (Figure 1.1a). Because they are impenetrable spheres with a well-defined size, it is physically impossible for particles to draw nearer beyond contact. For this reason, hard sphere interactions are sometimes referred to as excluded-volume interactions. Such interactions closely follow atomistic behaviour (2). Pusey and Van Meegen investigated the phase behaviour of hard spheres (Figure 1.1b). They published the first experimental proof of the existence of entropic crystals (3) and the glassy state (4), as was previously predicted by theoretical models (5; 6). Because hard spheres do not show any interactions until contact, this phase diagram can be considered the cornerstone for all other (exotic) phase diagrams. A schematic of the paradigm hard sphere state diagram is therefore shown in Figure 1.1b and will be described in more detail below.

At low volume fraction ϕ, the sample is in a gas-like state. Only a few particles are suspended in the solvent so that the probability of particles meeting is low. As a result, they undergo simple Brownian motion, which means they follow a random walk in the sample without being hindered: their diffusivity is maximal. As ϕ increases, the liquid becomes denser. The chances of two particles coming into contact increases - simply because of the larger number of particles. At even higher concentrations, a hard sphere system will form a crystal, due to it excluded volume interactions. Such an ordered phase might seem counterintuitive, until we consider that this structure allows each particle space to rattle in their cage: although long range order will increase, each hard sphere can explore the maximum number of microstates in its cage. At high densities, a crystalline order is thus the equilibrium state with the lowest free energy. If the onset of crystallisation is very slow or suppressed, increased number density will restrict the diffusivity of a particle by the close proximity of other

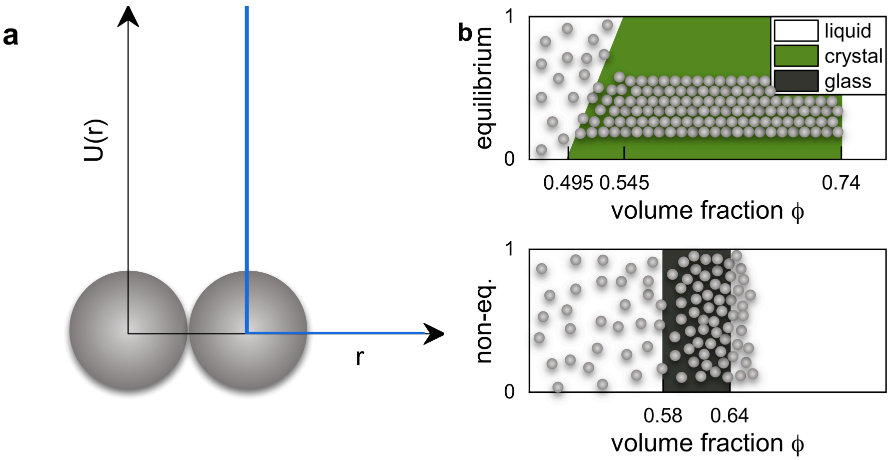

Figure 1.1: **Hard spheres.** **a**: interaction potential $U(r)$: no interactions are felt until the point of contact, where the repulsion becomes infinite. **b**: state diagram. Phases are colourcoded, and the particles indicate the appearance of each phase. Two routes are shown; the out-of-equilibrium route above and the thermodynamic equilibrium below. The only variable affecting the phase behaviour is volume fraction ϕ.

particles. This eventually leads to an arrest transition due to the persistent nearest neighbour cage, accompanied by a viscosity increase of multiple magnitudes. This so-called glassy phase is highly disordered and possesses a higher free energy than the crystal. However, particles are kinetically trapped, so that they are prevented from structuring themselves into the lowest energetically favourable state, i.e. the crystal. Because the key difference between the liquid and glassy state is the dynamics of the particles, the structural signature of liquid and glassy states are very similar (7–9).

Because the interactions are based solely on particle-particle contact, the hard-sphere phase diagram possesses only one relevant state variable, the volume fraction. This case is also referred to as the athermal limit, as it does not depend on temperature. Hard spheres are quite difficult to create, as it implies that all other interactions are eradicated while particles remain stable. After van Megen and Pusey's work the field of colloidal interactions and phase behaviour of hard spheres grew enormously, with a vast amount of work generated in the 90s. In recent years, the focus has shifted from hard sphere systems to soft and responsive colloids (10) as well as anisotropic particles (11; 12). Such systems offer new phases and interesting materials properties, which in some cases can be tuned externally.

1.3 Part I: The complex phase behaviour of thermoresponsive microgels

The soft colloids studied in this thesis are so-called microgels. Microgels are miniature, covalently crosslinked polymer networks (10; 13–16), typically suspended in water. Their colloidal size but polymeric nature places microgels at the interface of colloid and polymer science (17–19).

The key characteristic of microgels is their fast response to external stimuli. Depending on the monomers incorporated in the polymer network, a microgel will adapt its network swelling to parameters such as temperature (20), pH (21) and salinity (13; 22). A change in network swelling cascades into an altered volume fraction, and here lies the root of the popularity of microgels in current research. The facile way of tuning the volume fraction *in situ* - simply by varying the sample temperature, for example - leads to elegant experiment design. For example, microgels have been used to study phase transitions (23–27), and glass or jamming transitions (10; 28–31). In other studies, the variable size of microgels is conveniently used to tune directed self-assembly. A sophisticated application of this can be found in Sacanna *et al.*'s work, where microgels are used as agents to switch on at off at will the selective binding of two anisotropic colloids. (32; 33). Another example of directed self-assembly can be found in the preparation of thermo-responsive colloidal molecules, where each 'atom' constitutes one microgel (34).

The inherent open structure and softness of the polymer network results in markedly different interactions and phase behaviour compared to the classical hard sphere system. Microgels interact via soft repulsion (35; 36) and are very forgiving for polydispersity in the crystalline phase (37). A rich phase behaviour is predicted for various types of microgels (38; 39), while the application of an electric field causes unique phase behaviour (27; 40–42). In addition, because of their polymeric nature, microgels can interpenetrate, deform or shrink, allowing packing fractions $\phi > 1$ (43–47). Such behaviour is highlighted by work from Hendrickson *et al.*, who show that loosely crosslinked microgels are able pass through pores up to 10x smaller in particle diameter (48). Clearly, microgels are a versatile class of colloids.

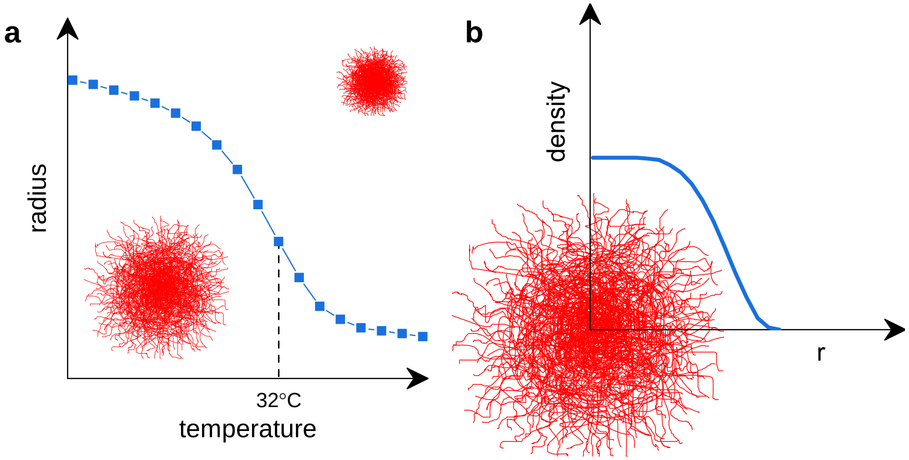

Figure 1.2: **Characteristics of neutral microgels.** **a**: Swelling behaviour of neutral microgels is governed by temperature. Microgels are swollen below $T<32\,^{\circ}$C and show a collapse beyond $T>32\,^{\circ}$C. **b**: the inhomogeneous radial density profile for microgels shows a gradual decay towards the outer surface of the particle, leading to a dense core and soft shell structure.

1.3.1 Neutral microgels

In this thesis, specifically two types of microgels have been studied. On one hand, the interactions and phase behaviour of neutral poly(N-isopropylacylamide) (PNIPAM) microgels are scrutinised, which we introduce in this section. On the other hand, the effect of internal structure on the phase diagram of ionic poly-(N-isopropylacylamide)-co-acrylic acid (PNIPAM-co-AAc) microgels is investigated (see next section). The swelling response of neutral PNIPAM microgels suspended in aqueous solution hinges solely on temperature, with the volume phase transition temperature (VPTT) typically given as 32 °C (Figure 1.2a). This value is based on the study by Heskins and Guillet in 1968 on linear PNIPAM chains in water (49), although it has not proven entirely reproducible in later studies (50). The temperature influences solvent quality, which in turn affects polymer-solvent interactions. Below the VPTT, polymer-solvent interactions are favourable and so the microgel network contains up to 80% solvent (20; 51–54). Above the VPTT, polymer-polymer interactions dominate and so some fraction of solvent is expelled from the network - although a reasonable amount of solvent (20-30%) is retained within the polymer (52; 55; 56). The first microgels created from PNIPAM are reported by Pelton in 1986, and their work is still widely referenced in the synthesis of microgels (52; 57). In recent years, a lot of research has been performed with this archetypical microgel, not in the least because their LCST is biologically relevant and experimentally accessible (58–62).

For neutral microgel structure, a pivotal paper from Stieger *et al.* (63) coined the fuzzy sphere model to describe the form factor as extracted from microgel scattering experiments. It relates the microgel scattering profile to a spherical particle with a dense inner core, surrounded by a lower-density corona. This particular core-shell structure is caused by the inhomogeneous crosslinker distribution throughout the microgel network, due to the high reactivity of the crosslinker during microgel synthesis (64; 65). The fuzzy sphere model has gained traction since its conception, and has lead to the generally accepted idea of neutral microgels as a densely crosslinked core with a loosely crosslinked shell, with dangling ends decorating the surface (63; 66–69) (Figure 1.2b). Of course, changing synthesis parameters to a continuous feed of crosslinker, or monomer, or both, will lead to particles with a homogeneous inner structure (70–74). In addition, the amount of added crosslinker will affect network flexibility (75).

It is precisely this inhomogeneous structure that sparks the interesting phase behaviour of neutral microgels mentioned before. Surprisingly, despite the vast body of work utilising microgels in some way, their interaction potential - and its connection to the core-shell structure of the microgel - is still under debate. The phase diagram is complex, because of the gradually decreasing solvent quality with increasing temperature, and because the microgel can be packed to ultra high densities (Figure 1.3c). It is difficult to establish the actual volume fraction in the system, or to study microgel conformation under such closely packed conditions. These issues hamper studies into mapping the interaction potential of neutral microgels.

In broad strokes, first experiments relating the viscosity to interaction potential concluded a temperature independent hard sphere-like interaction for swollen microgels at volume fractions $\phi \sim 0.3 - 0.5$, while at higher packing fractions a deviation from hard sphere viscosity behaviour was observed, suggesting soft sphere interactions (20; 76–78). Early experiments on the effect of transgressing the VPTT showed that an attraction emerges for collapsed particles, due to the increasingly favourable polymer-polymer interactions, as well as stronger van der Waals attractions due to a compacter microgel (56; 63; 76; 79; 80) (Figure 1.3a). The stability of the suspension depends on ionic strength at elevated temperatures, as residual charges from the synthesis can lead to electrostatic repulsions preventing gelation (22).

Although the attraction beyond the VPTT is universally recognised, recent work has indicated that swollen microgels interact via a soft repulsion, rather than a steep hard sphere-like repulsion (35; 36; 56; 81; 82) (Figure 1.3b). The evolution of the interaction potential starting from a particle with soft repulsion ($T <$VPTT) leading to a compacter microgel with considerable attractions ($T >$VPTT) remains unclear. Clearly,

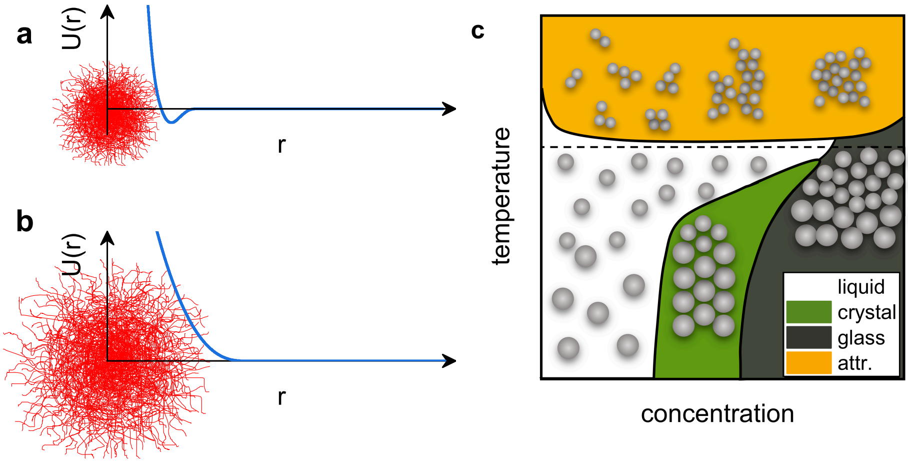

Figure 1.3: Neutral microgels. a: Interaction potential $U(r)$ above VPTT. Particles are collapsed and attractive. b: Interaction potential $U(r)$ below VPTT. Particles are swollen and interact via soft repulsion. c: State diagram. Phases are colourcoded, and the particles indicate the appearance of each phase. The dashed line corresponds to the VPTT. Increasing temperature causes deswelling of soft repulsive microgels, until beyond the VPTT attractions reign. Increasing volume fraction allows ultra-high packing fractions beyond $\phi = 1$.

this emerging picture of microgels with complex, temperature dependent interactions forces us to look at previous work in a different light. Most research simply uses microgels as a tool, with an easily variable volume fraction, under the assumption that microgels are temperature-independent hard-sphere like colloids until $T = 32°\mathrm{C}$ (10). Therefore there is a sense of urgency in mapping the interactions of microgels across temperature and volume fractions, so that we may correctly (re-)interpret previously published results.

We now see what literature has to offer us in terms of proposed interaction potentials, tailored for microgels. Linked to the core-shell structure, a two-component brush-like model was proposed, with either an incompressible (81) or compressible core (82) surrounded by soft polymer brushes according to a modified Alexander-De Gennes model. This model highlights the colloid/polymer duality of the microgel, where key elements from colloidal and polymer science are combined. The model was tested on a single microgel sample at varying temperatures, spanning $\phi = 0.2 - 0.9$ (81). Despite the refinement in the model, which incorporates many aspects of typical microgel architecture, the theoretical predictions did not correspond to experiments performed by Mohanty *et al.*, where numerous samples were examined at constant temperature $T = 15°\mathrm{C}$. (36).

More promising candidates include soft repulsion potentials such as the harmonic potential (83) or the Hertzian potential (35). Such potentials decribe the interaction between elastic particles upon (slight) compression, and can thus be linked back to the network flexibility of the microgel network (84). However, the internal architecture of the microgel is neglected in such an approach, which casts doubt on the applicability of these models at high volume fractions. The same study by Mohanty *et al.* shows that both a harmonic and a Hertzian interaction potential correctly predicts the experimental order in liquid microgel suspensions (36), where the authors concluded that a Hertzian soft repulsion finds more root in the nature of the microgel.

The unique characteristics of neutral thermoresponsive microgels open up many exciting avenues of research, but at the same time the high sensitivity to temperature and possibility to overpack complicates the interaction landscape. Microgels are known to transform from soft repulsive polymer network to more compact attractive colloids with increasing temperature, yet no attention has been given to mapping how interactions change across the phase diagram. The aim of this thesis is to extract an interaction potential which is valid throughout the rich phase diagram of microgels.

Testing the validity of the Hertzian interaction potential for swollen neutral microgels lies at the heart of Paper I , where we present a more complicated form of the model to include crucial core-shell effects. We show that the (multi-)Hertzian captures structural correlations across a broad range of volume fractions and temperature. In addition, we demonstrate that the Hertzian indeed breaks down due to lack of a significant core repulsion, once particles reach the overpacked state (Paper II). A theoretical basis for the suitability of the multi-Hertzian model is laid in Paper III, which elevates it from a phenomenological model to one supported by theory.

1.3.2 Ionic microgels

Co-polymerising functional groups into the microgel network adds a layer of complexity. The resultant microgels become responsive to additional external stimuli, and their swelling response will consequently depend on many factors. Although this increases the applications and tunability of the system, it also makes it more difficult to tightly control the size - and thus volume fraction.

Hoare and Pelton have extensively shown that the nature of the incorporated comonomer can have a pronounced effect on the internal structure of the microgel, where the reaction kinetics, hydrophilicity and affinity for NIPAM play a crucial role, and lead to non-intuitive trends (85–89). In our research, we focus on NIPAM copolymerised with acrylic acid (AAc), so-called PNIPAM-co-AAc microgels. From

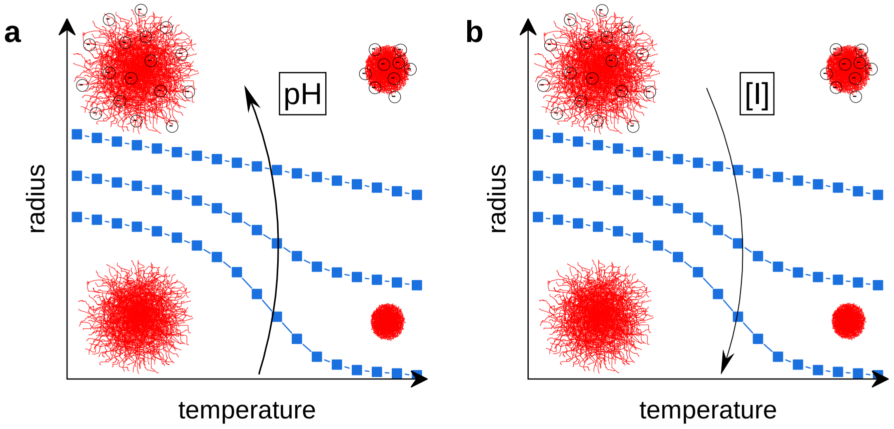

Figure 1.4: Swelling behaviour of ionic microgels is governed by temperature, pH (panel **a**) and salinity (panel **b**).

Hoare and Pelton's research, it is known that the acrylic acid groups distribute quite evenly throughout the microgel network (87; 88).

In literature, the internal structure of these type of microgels is often related back to the fuzzy sphere model as introduced for neutral microgels, with a dense core, loose corona and dangling ends (82; 90–93). Surprising morphologies are sometimes presented (93). In addition, changes in the *overall* size of the ionic microgel caused by tuning external factors (i.e. salinity, pH, temperature) have been reported, highlighting the complex swelling response (Figure 1.4) (21; 94–96). However, to our knowledge, the influence of such external parameters on the *internal* structure has been left unexplored. Because of the core-shell architecture, a different swelling response from the core compared to the shell can be reasonably expected, which in turn will affect any proposed interaction potential.

Especially when considering the internal morphology of large (neutral or ionic) microgels, the available research is limited. Generally, static light scattering data is obtained, from which the form factor can be extracted. The form factor can then be related back to structural models. Although the fuzzy sphere model reasonably works for large swollen microgels, once the composition of the microgel changes, there are no alternative models (54; 71). A few reverse-engineering approaches exist, which determine the structure of the scattering colloid based solely on the form factor, bypassing the need for a theoretical model (97–99), but these have yet to be used for ionic microgels.

The unexplored internal swelling response of PNIPAM-co-AAc microgels hampers further investigation into their interactions. After all, it remains to be seen how internal and external factors affect shell and core swelling, and the consequent interaction potential. The sensitive size of PNIPAM-co-AAc microgels poses another challenge: the actual volume fraction ϕ at any given temperature, concentration, pH or ionic strength is always a point of contention. The volume fraction is the only relevant parameter when it comes to hard sphere phase diagrams, and it is common for authors to describe in depth how they have reached it. Poon, Weeks and Royall describe in detail the difficulties of establishing ϕ already for hard colloids (100).

Temperature, salinity, pH and volume fraction are all state variables which affect microgel swelling and the resulting phase behaviour. Evidently, capturing ϕ for systems where the size is so responsive and ill-defined as for ionic microgels - and possibly constantly varying - is problematic. Therefore in some papers the effective volume fraction ζ is used, where the hydrodynamic radius of the particle at high dilution is assumed constant even at high concentration, where the particle size may decrease (see e.g. (101; 102)). The resultant phase diagrams cannot be related between studies, which has lead to difficulties comparing to theoretical predictions. In fact, the additional charges within the microgel generate a predicted rich phase diagram with many exotic crystal phases (Figure 1.5b) (38). Despite numerous studies on the phase behaviour of ionic microgels, the existence of nearly all of these crystal phases still needs to be (dis)confirmed (91; 92; 101–103). The uncertainties surrounding volume fraction and size make it impossible to pinpoint why these crystals have yet to be found.

It is not known how ionic microgel interactions drive the phase behaviour, or how this depends on innate properties such as charge and crosslinker density. Theoretical studies on ionic microgels suggest that in addition to the elastic Hertzian soft repulsion - similar to neutral microgel - the ionic microgel also possesses an electrostatic repulsion, caused by the charged groups on the polymer backbone (42; 104–107). Most of the charges are 'inaccessible' to any neighbouring particles, because counterions are tightly bound to the backbone within the core of the microgel (108). Regardless, an appreciable electrostatic repulsion is expected, especially at low dilutions (Figure 1.5a, denoted with U_Y for Yukawa-type repulsion). With increasing concentration, the elastic soft repulsion will take over the baton as particle contact becomes more and more frequent (Figure 1.5a, denoted with U_H for Hertzian repulsion) (42; 104–107). The proposed cross-over between these two governing forces has never been scrutinised over a full concentration range. Rather, the model has been tested with good results on single state points (42; 105).

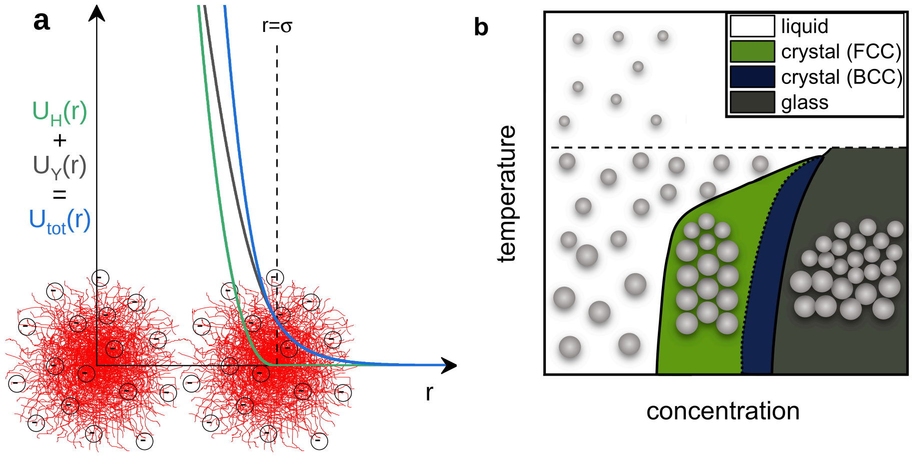

Figure 1.5: Ionic microgels. **a**: Different contributions make up the total interaction potential $U(r)$ for ionic microgels. Dashed lines represent Hertzian soft-repulsion, dotted lines indicate the Yukawa-type electrostatic repulsion. Under dilute conditions, the electrostatic repulsion dominates (inset 1) while in denser systems, particle contact increases and the Hertzian repulsion emerges (inset 2). **b**: Proposed state diagram at constant size, charge, pH and salinity. The existence of an additional crystal phase is suggested. Changing size, charge, pH or salinity will result in a different state diagram, highlighting the complexity of the system.

The internal structure of ionic microgels - and their response to various charge regimes - is a crucial ingredient in the interaction potential. In Paper IV , we therefore present a detailed light scattering study where we explore the core and shell swelling as function of network charges for loosely crosslinked PNIPAM-co-AAc microgels. We demonstrate that charges have a pronounced effect mainly on dangling end conformation. Surprisingly, all microgels possess a persistent low density core, which we couple to the overlooked role of the initiator during synthesis. Polymer theory captures the network swelling as function of both the innate and external factors, and gives us the necessary tools to predict the internal structure of ionic microgels.

Paper V describes an extensive study on the effect of ionic microgel softness on the resultant phase behaviour. Combining theory and experiments, we see a consistent short ranged repulsive interaction for rigid microgels, while extremely soft microgels display the strongest elastic-electrostatic interactions. The interactions, dictated by the corona and dangling ends of the microgels, lead to distinctly different phase behaviours. The theoretical comparison allows us to extract a 'true' volume fraction for each state point, so that we can present the first realistic experimental phase diagram for ionic microgels, which does not rely on the size at extreme dilutions. Again, no exotic crystal phase was observed.

1.4 Part II: Liquid-solid transition in dense protein systems

Twenty-two different amino acids constitute the building blocks for all proteins. Any protein consists of a long chain of covalently linked amino acids, and folds up in a specific way. The interactions of the protein therefore depend on the type of amino acids incorporated, as well as the folding pattern. It follows that proteins are highly responsive, and their conformation and interactions can change based on their environment. This is the molecular basis for lots of protein functionality (109).

It is thus no surprise that physical chemists are treating proteins as complex colloids with mixed interactions, and that proteins can display a wide range of phases. Under low ionic strength conditions, a protein can possess a long-ranged repulsion, in combination with a short-range attraction (SALR potential). For proteins interacting via the SALR potential, a new and unexpected phase has been discovered, the so-called cluster phase. The first report suggesting the equilibrium cluster phase exists has been hotly debated, as it initially seemed counter-intuitive that such a structure could arise in equilibrium (110). However, with continuous efforts to (dis)prove the clustering at volume fractions as low as $\phi = 0.1$, the picture has emerged of a widespread phenomenom observed for various proteins and colloids (111–120).

Physical chemists are exploiting the link between proteins and colloids: by coarse-graining the protein (i.e. averaging out microscopic details), the cluster phase can be understood using colloidal science (113; 115; 121–125). Here we can make some distinctions on the level of coarse-graining. Because proteins are highly heterogeneous in composition, their interactions are complex, and it would be too computationally intensive to follow each amino acid for each protein separately. Therefore, the question arises which colloidal theory accurately reflects protein interactions. Models with a high level of detail, for example patchy particle models which include the hydrophobic patches and charge of the protein, will likely approximate interactions and resultant phase behaviour better than models with a high level of coarse graining.

In this work, we focus on liquid-solid transitions in dense protein suspensions. We investigate how the repulsions between equilibrium clusters in lysozyme suspensions are the driving force towards arrest. This is a key question in formulation science, for example in the preparation of monoclonal antibody suspensions for cancer treatment (126; 127). The viscosity behaviour of γ_B-crystallin, which occurs in high concentrations within the eye lens, is also followed (128–130). This protein has attractive patches on its surface, which are likely to dominate interactions and phase behaviour under physiological conditions, where long range electrostatic repulsions are screened (117).

Unfortunately, investigations into the rheological properties of proteins is challenging, as achieving sufficiently concentrated samples is often a hassle. In addition, biological samples can be precious, with only small amounts available. Only with the advent of new micro-liter technologies has it become possible to look closer at densely packed protein samples, as minute samples are sufficient for analysis. One example is active or passive microrheology, where the motion of a tracer particle embedded in the medium of interest is monitored (for a review of microrheology see Refs. (131; 132)). Such techniques require only < 0.1 ml of sample, which is much more manageable compared to > 1 ml needed for conveniental rheology. Our research utilises passive micorheology only, which is non-invasive and so-called 'passive' because particle motion is left undisturbed (in contrast to active microrheology, where tracer particles are dragged actively through a medium). Instead, the Brownian motion (and by extension the diffusion coefficient) of tracer particles is followed for example via optical microrheology or multiple particle tracking. Because the size of the particles is well defined, the obtained diffusion coefficient can then be linked to the zero shear viscosity η_0 of the medium, via the well-known Stokes-Einstein relation (132; 133). These techniques are described in more detail in the Experimental section.

1.4.1 Lysozyme

The first protein under investigation is lysozyme, which is a part of the innate immune system as it lyses the bacterial wall (134). Because of its high accessibility - it is easily won from chicken eggs - lysozyme has become a much-studied model system. Under low ionic strength, the electrostatic interactions are left unscreened, and the balance between the short range attractions and long range repulsion results in the equilibrium cluster phase at moderate to high volume fractions (112–115; 121; 125; 135–142). In fact, the first notable research on the existence of equilibrium clusters was performed on lysozyme (110). In Figure 1.6, the characteristic phases of lysozyme (under low ionic strength, as is used for this work) are shown.

Surprisingly, despite the vast amount of studies dedicated to lysozyme and its cluster-forming behaviour, very little is known about its cluster driven arrest. The typical issues concerning sample densification described above also plague lysozyme research, so that most studies concerning the zero shear viscosity η_0 of lysozyme investigate up to volume fraction $\phi \approx 0.25$ (110; 112; 114; 135). A mere two studies are available which characterise how lysozyme (interacting via the SALR potential) suspensions forms glasses, and these present opposing conclusions. Cardinaux *et al.* (115) find

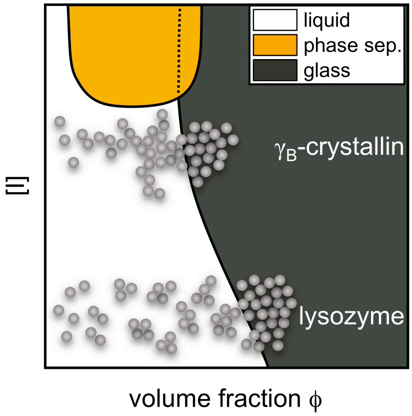

Figure 1.6: State diagram for colloids interacting via a mixed potential. The depiction is not entirely fair, as such a state diagram has three axes (attraction strength U_a, repulsion strength U_r and temperature T). We simplify it by keeping U_a constant, to highlight the different interactions between lysozyme and γ_B-crystallin under the studied conditions. Under low ionic strength, the SALR potential exhibited by lysozyme leads to repulsions at large distances but attractions at short distances. In the presence of buffer to mimic the physiological pH, the electrostatic repulsion is entirely screened for γ_B-crystallin. While both proteins display the states shown in the diagram (liquid phase, liquid-liquid phase separation and glassy), the pathways and underlying structures are thus significantly different.

indications of an arrest at $\phi_{\max} = 0.26$ at 5°C. Godfrin *et al.* (141) concluded that while on the short time scale, lysozyme displays a glassy behaviour, the long time scales revealed a long-lived macroscopic fluid, even at $\phi = 0.35$ at 5°C. In both cases, the experimental findings could be explained within a theoretical framework (115; 140; 142). Evidently, colloidal theory offers no explanation for how such different conclusions could be drawn, and so the existence of a cluster driven glass transition for dense lysozyme suspensions at low ionic strength is still under debate.

(Dis)confirming the possible liquid-solid transition in dense salt-free lysozyme solutions is the topic of Paper VI. We combine microrheological tools with novel sample preparation techniques to achieve volume fractions beyond $\phi = 0.25$, where we take strong advantage of the minute sample requirements. The zero shear viscosity behaviour of concentrated lysozyme samples is followed upon approaching the glass transition. We unambiguously confirm the existence of a glass transition, and demonstrate how micro-litre based sample preparation and measurements open up new avenues in exploring dense protein dynamics.

1.4.2 γ_B-crystallin

The second protein under scrunity is γ_B-crystallin, which belongs to the family of γ-crystallins. Together with α-crystallins and β-crystallins, γ-crystallins are the main constituents of the vertebrate eye lens (129). In the vertebrate eye lens, protein concentrations are up to 500 mg/ml in order to facilitate a high refractive index (128; 130). It is essential for such dense concentrations to remain in a liquid-like state in order to retain the flexibility of the lens, which is necessary to focus on objects both nearby and far away (143). As we age, the quality of the eye lens - its flexibility and capability to focus - decreases, leading to presbyopia (143). The question thus arises if we can identify processes underlying the stiffening of the eye lens, which is intrinsically linked to arrest transitions of the eye-lens proteins.

Under physiological conditions, γ_B-crystallin interactions are dominated by attractions rather than repulsions, due to the presence of attractive hydrophobic patches on its surface (117; 144; 145). These anisotropic interactions lead to string formation and open, transient networks at relatively low volume fraction (Figure 1.6). The dynamics of γ_B-crystallin has been shown to slow down dramatically in the vicinity of a neighbouring protein (117; 145). The patchy attractions thus affect the structural ordering and short time diffusion of γ_B-crystallin, but no studies on the macroscopic viscosity behaviour have been performed (which is linked to long time diffusion).

In Paper VII we investigate the temperature dependence of the arrest line of γ_B*-crystallin, utilising the same techniques as for Paper VI. Again, the zero shear viscosity is tracked using two complementary microrheology technique, and we employ evaporation-mediated sample preparation to reach volume fractions beyond the arrest transition. Viscosity values are obtained between 20-35° C and display a minimal temperature dependence of the glass line. The divergence of the viscosity close to the arrest can be captured with a power-law approach. The early onset of the arrest is caused by the anisotropic patchy interactions.*

2 | Materials and Methods

2.1 Confocal microscopy and image analysis

Confocal laser scanning microscopy (CLSM) is an effective tool to study state diagrams. The main advantage of CLSM is the direct measurement of structures in real space as opposed to working in reciprocal space for scattering experiments. In addition, both structural and dynamic information can be obtained, although data acquisition needs to be adjusted based on the particular quantity one is after. Most importantly, the recorded data can be analysed quantitatively through dedicated image analysis scripts, opening up avenues to theoretical and numerical comparison.

2.1.1 Basic principles

Like any other microscope, the basis of the confocal lies in illuminating a sample, and recording the resultant image. A confocal microscope can be seen as a specialised type of epi-fluorescence microscope. The contrast often stems from fluorescence, and detection is sensitive because even very low fluorescence signals can be detected. In epi-fluorescence microscopy, the entire sample is flooded with light and any and all emitted photons are detected. As a consequence, the sample photobleaches easily and resolution is generally low. The resolution of the confocal microscopy has been enhanced in several ways, which we will expand upon below.

The basic set-up of a confocal microscope is shown in Figure 2.1. A laser source is focused onto the sample via lenses and mirrors. The lenses ensure that the laser beam is focused on a specific spot in the sample, i.e. point illumination. The laser - with an excitation wavelength compatible with the fluorophore - thus excites only a small focal volume, and the elicited photons are guided via mirrors and lenses to the detector

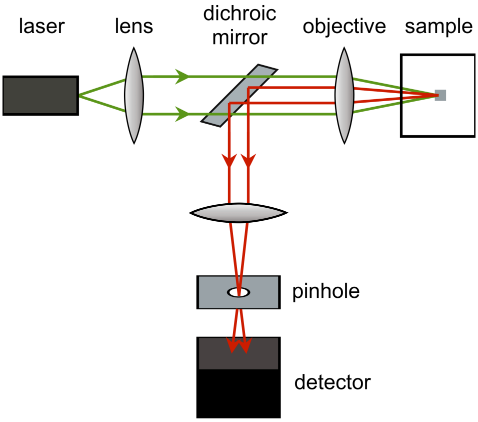

Figure 2.1: **Schematic of a confocal microscope.** The incident laser beam (green) is focused on a particular spot in the sample via lenses and the objective. The resultant fluorescence signal (red) is guided to the detector. The pinhole prevents any light from out-of-focus planes to hit the detector.

(photomultiplier tube). A key ingredient is the placement of a pinhole in front of the detector, which filters out any out-of-focus light. In addition, the point illumination allows for scanning of the sample pixel-by-pixel. These factors greatly enhance the spatial resolution of the microscope.

2.1.2 Resolution

Although the resolution is decidedly higher in confocal microscopes than standard issue fluorescence microscopes, the resolution limit - ubiquitous in microscopy - is a limiting factor. The resolution limit basically describes the minimal distance between two features necessary to distinguish them; any features that lie closer together cannot be resolved. It depends on the numerical aperture (NA) of the used objective and the excitation and emission wavelength of the laser and fluorophore λ_{ex} and λ_{em}, respectively. The resolution of a microscope is often captured via the Rayleigh criterion, which is defined as $R_{\mathrm{x,y}} = \frac{0.62}{\mathrm{NA}}\sqrt{\lambda_{\mathrm{ex}}\lambda_{\mathrm{em}}}$ for the $xy-$plane, and $R_{\mathrm{z}} = \frac{2n}{\mathrm{NA}^2}\sqrt{\lambda_{\mathrm{ex}}\lambda_{\mathrm{em}}}$ for the $z-$direction, where n is the refractive index of the sample medium (146). In the case of confocal microscopy, the additional pinhole will increase resolution two-fold (147).

In this research, an objective with $\mathrm{NA} = 1.4$, a laser with wavelength $\lambda_{\mathrm{ex}} = 543\mathrm{nm}$ and a fluorophore with $\lambda_{\mathrm{em}} = 660\mathrm{nm}$ was used. The resolution in the xy-plane

$R_{x,y}$ then becomes 134nm, and the resolution in the z-direction $R_z = 516$nm. The Nyquist-Shannon sampling requirement then states that the pixel size should be $\frac{1}{2.8}$ times the resolution limit in the xy-plane, and $\frac{1}{2}$ time the resolution limit in the z-direction (146; 148). The ideal pixel size, or so-called pixel pitch, then becomes ∼50nm in the xy-plane and ∼260nm in the z-direction (148).

2.1.3 Image analysis

The main set of image analysis scripts (and also the ones that are used in our research) are the particle tracking scripts written in the Interactive Data Language (IDL) from Crocker and Grier (149), which have been developed in the 90's and are widely used to track particles (29; 30; 101; 150–152). These scripts are powerful, because the position of the particles can be determined beyond the pixel size. As it is known a priori that the particles are spherical, the centroiding algorithm will first detect the highest intensity pixels in a given micrograph, and will then consider all pixels surrounding these local maxima (within a region specified by the user). Using all pixels constituting one particle will refine its precise centre of mass. In addition, much more information can be gathered on the brightness and eccentricity of the particle (149).

In practical terms, the feature finding algorithm finds all features - based on a given size - in a bandpassed image. It is then up to the researcher to select the correct features, i.e. to 'throw' away features which are not exactly in the focal plane (36; 148; 149; 153). The 'clean' dataset can then be used to calculate structural and dynamical information. A detailed guide to image analysis can be found in the Appendix, where the entire approach is explained from start to finish.

In this thesis, we focus on two main properties distilled from quantitative image analysis: the pair correlation function $g(r)$, which signals the structural ordering in the system, and the mean squared displacement MSD, which is a measure of the particle mobility. The MSD will be explained in conjunction with the microrheology methodology (Section 2.4.2), as it is instrumental in deriving rheological properties from the sample.

The pair correlation function $g(r)$ is a probability density function, describing the probability to find a particle at a certain distance r away from a reference particle placed at the origin. A schematic representation of the $g(r)$ for a dense liquid is shown in Figure 2.2. Essentially, the $g(r)$ is nothing more than a histogram: the number of particles in a shell of dr around the reference particle are counted, and the values are normalised by the shell area or volume and the number density within the sample.

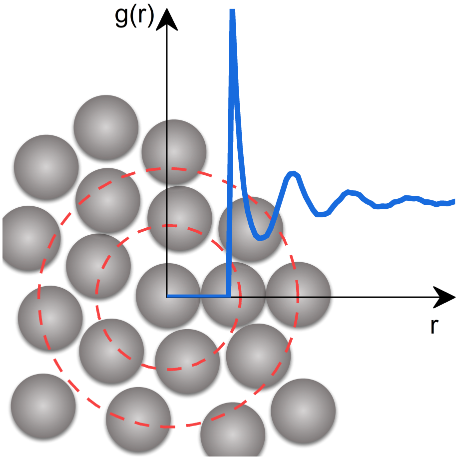

Figure 2.2: Pair correlation function for a dense liquid.

Typically, a sharp first peak occurs around a distance equivalent to (or larger than) the particle diameter: as particles possess a finite size, it is physically impossible for a neighbouring particle to occupy the same position. The first peak position of the $g(r)$ thus signals the characteristic nearest neighbour distance. In the liquid state, the short range ordering around the reference particle becomes more and more diffuse with increasing r, so that the likelihood of finding a random particle at large distances is always unity. For glassy states, a similar short-range order is found. Crystalline states, on the other hand, possess long range structural ordering, as each particle is situated onto a lattice. Therefore, characteristic peak positions will be found for the crystal $g(r)$.

2.2 Light scattering techniques

The experimental premise for light scattering experiments is straightforward: the sample is illuminated by a light source, and the resultant scattered photons are recorded as a function of scattering angle (see also Figure 2.3a). Based on the detected photons, information can be derived about the size, shape and interactions of the particle suspension. Both dynamics and static light scattering (DLS and SLS) analyse the scattered photons, but in different ways. The incoming beam is scattered due to the refractive index mismatch between the scatterer and the surrounding medium.

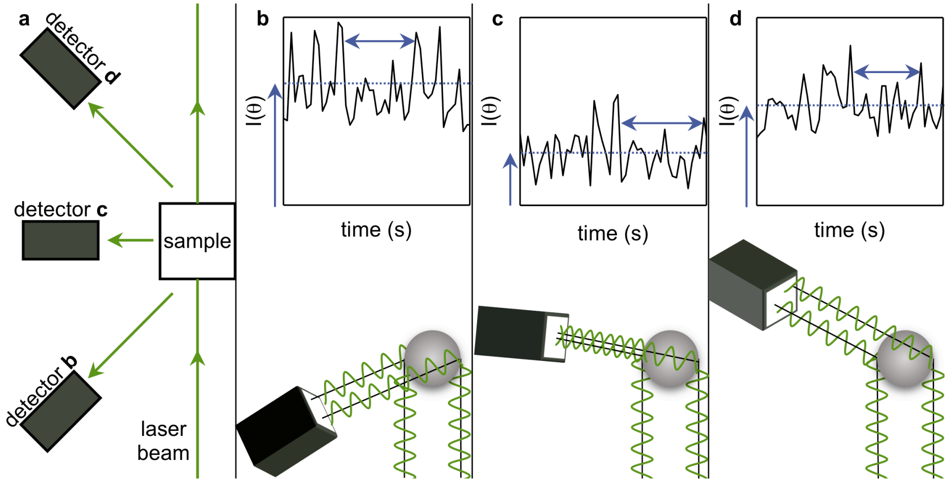

Figure 2.3: **Typical set-up for a light scattering instrument.** **a**: Schematic overview. A laser illuminates a small part of the sample. Using detectors at various angles θ the intensity of the scattered light is collected for a certain period of time. **b-d, top**: Typical data obtained at various scattering angles. The average scattered intensity is related to the form factor and dependent on angle. The fluctuations in the signal are related to the diffusion speed of the colloids. **b-d, bottom**: Depending on scattering angle, constructive or destructive interference between scattered waves will arise, which leads to distinct maxima and minima in scattered intensity.

2.2.1 Static Light Scattering

In static light scattering, the intensity of scattered light I is related to the scattering angle θ, or angular position of the detector. The intensity of scattered light is related to the size of the colloids, their volume fraction, refractive index mismatch and colloid-colloid interactions according to

$$I(q) \propto n_c V_c^2 \Delta\rho^2 P(q) S(q). \tag{2.1}$$

Here, n_c corresponds to the number density of colloids, V_c is the volume of a single colloid, $\Delta\rho$ denotes the difference in scattering length density (i.e. the refractive index mismatch in the case of SLS), $P(q)$ the so-called form factor and $S(q)$ the structure factor. Rather than using the scattering angle θ, the scattering vector $\vec{q}$ is used (a generalised form of the scattering angle) so that results from different instruments may be compared: $\vec{q} = |q| = \frac{4\pi n_s}{\lambda}\sin(\frac{\theta}{2})$. Here n_s corresponds to the refractive index of the solvent, and λ is the laser wavelength.

In our research, we are not interested in the absolute value for $I(q)$, but rather in the information $I(q)$ contains on the shape and size of the colloids. This comes back in the form factor $P(q)$. In order to ensure a genuine scattering profile to relate back to

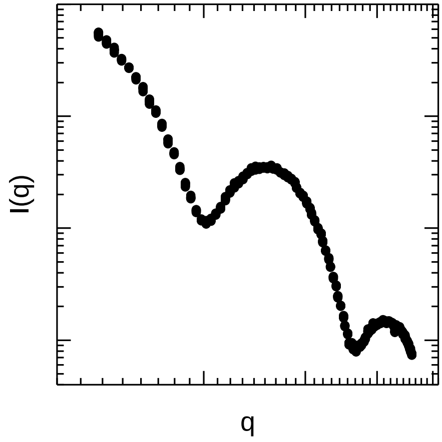

Figure 2.4: Typical formfactor ($I(q) \sim P(q)$ obtained from SLS measurements.

$P(q)$, very dilute samples are measured. This has two reasons: (1) the probability of particles meeting and interacting reduces so that the structure factor $S(q) \rightarrow 1$ and (2) only single scattering events are recorded. Multiple scattering will smear the recorded data and reduce data quality, but can be overcome by using 3D light scattering, and is thus not really relevant in our case (154).

The shape of the colloids affect the scattered intensity as follows. A coherent beam hits the sample. If we consider one scattering event, the photon will be returned to the detector with a certain phase. However, if another scattering event occurs exactly out of phase, the two events will essentially cancel each other out (destructive interference, see for example Figure 2.3c). If we consider one scattering angle q, the out-of-phaseness depends solely on path difference of the light scattered by both events, which is then related to the size and shape of the colloid. Because the intensity at a certain angle q is a superposition of all scattering events in the scattering volume, we then end up with specific minima and maxima in the scattered intensity (see Figure 2.3, 2.4). The scattering pattern $I(q)$ can then be fitted using structural models.

Some care needs to be taken in selecting the appropriate structural model, as the scattered intensity depends on which scattering regime the colloids are in. In our research, two distinct elastic scattering regimes need to be considered. Elastic scattering indicates that the wavelength of the incident beam and scattered beam are equivalent (in contrast to for example fluorescence). First we discuss Rayleigh-Gans-Debye (RGD) scattering. In this scattering regime, the particle can be represented by many point scatterers, so that the scattered intensity is simply the sum of the amplitude of all scattered photons. We assume that the incoming incident wave is not distorted within the particle (so-called first Borne approximation). Such an approximation simplifies creating analytical models. In order to fall within the RGD scattering regime, two criteria have to be fulfilled:

$$\begin{aligned} |1 - n_\mathrm{c}/n_\mathrm{s}| &\ll 1 \\ k2R_\mathrm{c}|1 - n_\mathrm{c}/n_\mathrm{s}| &\ll 1 \end{aligned} \tag{2.2}$$

where $k = 2\pi n_\mathrm{s}/\lambda$ and n_c and n_s are the refractive indices of the colloids and solvent, respectively (71; 99). In the case of microgels, $R_\mathrm{c} \sim \lambda$ but refractive index mismatch is assumed relatively low due to the high solvent content of the microgel. For this reason, many studies employ the fuzzy sphere model (based on RGD scattering) on SLS data (54; 66; 71).

The fuzzy sphere model essentially comprises the scattering from a homogeneous sphere, upon which some Gaussian smearing is placed to account for the rather soft microgel surface (as opposed to a clearly defined boundary). The resultant form factor P_fuzzy is thus given by:

$$P_\mathrm{fuzzy}(q) = \left[\frac{3[\sin(qR_\mathrm{c}) - qR_\mathrm{c}\cos(qR_\mathrm{c})]}{(qR_\mathrm{c})^3} \times \exp\left(- \frac{(\sigma_\mathrm{surf} q)^2}{2} \right) \right]^2 \tag{2.3}$$

where the first term is the analytical solution for scattering from a homogeneous sphere and the second term denotes the Gaussian smearing of the particle surface with width σ_surf (63). Although this gives some idea on the fuzziness of the particle, no further comment on the internal structure can be made.

We therefore employed scattering analysis based on the Mie scattering regime. In Mie scattering, the incident wave is distorted by the large size and inhomogeneous refractive index of the colloid. Depending on the location of the scattering event, the incident beam will have a different strength, so that the resultant scattered intensity is not a simple sum of the amplitudes of the scattered photons. Rather, the inward-moving and outward-moving waves need to be considered for each scattering event within the particle. Evidently, such calculations are more involved and numerical recursion is necessary to find a convergent solution. Yet, the resultant analysis will yield a wealth of information on the refractive index profile of the scattering particle.

We performed analysis based on Mie scattering from layered spheres, where each layer possesses its own refractive index (155).

2.2.2 DLS

In dynamic light scattering, it is not the average intensity as function of angle which is considered, but the temporal fluctuations of the scattered intensity as function of angle. Over time, due to particle diffusion the relative distances between particles within the scattering volume change, causing variations in the destructive and constructive interference generated. As a result, the total scattered intensity will fluctuate with time (Figure 2.3). Large colloids diffuse slower, and so the measured fluctuations will take longer to de-correlate. We therefore quantify the dissipation of light fluctuations via the intensity auto-correlation function g_2, defined as:

$$g_2(q,\tau) = \frac{\langle I(q,t)I(q,t+\tau)\rangle}{\langle I(q,t)\rangle^2} \tag{2.4}$$

where $I(q,t)$ is the intensity of scattered light at a certain scattering vector q and time t and τ is the lag time. Such an auto-correlation quantifies the time necessary to lose all correlation between two intensity signals. i.e. how long it takes for a colloid to move over a characteristic length $\frac{1}{q}$ (Figure 2.5). The intensity auto-correlation function g_2 is rewritten to the field auto-correlation function g_1 via the Siegert equation:

$$\beta[g_1(q,\tau)]^2 = g_2(q,\tau) - 1 \tag{2.5}$$

with β the intercept of the intensity auto-correlation function g_2. g_1 can be related to the diffusion coefficient D of monodisperse, spherical particles via the following analytical equation:

$$g_1(q,\tau) = e^{-\Gamma\tau} \text{ with } \Gamma = q^2 D \tag{2.6}$$

where Γ is the so-called decay rate. This data can be used to extract the hydrodynamic radius R_H in two ways. First, the found diffusion coefficient can be related to R_H via the Stokes-Einstein equation:

$$D = \frac{k_\mathrm{B} T}{6\pi\eta R_\mathrm{H}} \tag{2.7}$$

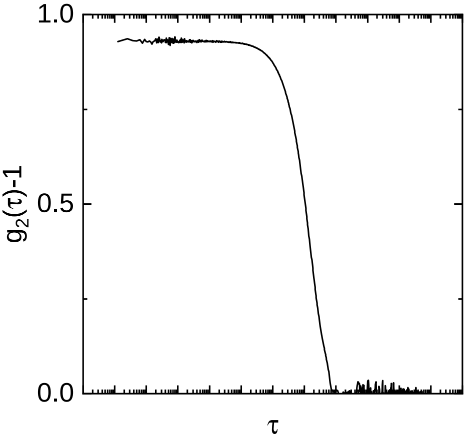

Figure 2.5: Typical intensity autocorrelation function $g_2(\tau)$ obtained from DLS measurements.

with η the viscosity of the medium and k_B the Boltzmann constant. A key assumption in the Stokes-Einstein equation is that particles experience unhindered diffusion, i.e. particle interactions are negligible. In this way, a single DLS measurement yields an estimate of the hydrodynamic size of the investigated colloids.

Secondly, the decay rate Γ can be plotted versus several q^2, so that the slope of the function is equal to D. So-called multi-angle DLS is more robust against artefacts introduced for example by measuring at angles which display a minimum in the form factor, i.e. where colloids do not scatter much, inviting unwanted scattering contributions otherwise suppressed by the colloid scattering signal.

2.3 Simulations

The algorithms and thermodynamic theory underlying simulations are expansive, and beyond the scope of this thesis (156; 157). Instead, we provide a brief description of relevant simulation approaches, to provide context for the chosen approach.

In any simulation the position $\mathbf{r}_i$ and velocity $\mathbf{v}_i$ of a given particle i must be tracked. In molecular dynamics (MD) simulations, the future properties are predicted based on the current properties. Since the central question is: how do the position and velocity change over time, Newton's equation of motion needs to be solved (for Cartesian coordinates):

$$m_i \frac{d\mathbf{v}_i(t)}{dt} = -\nabla_{\mathbf{r}_i} V = \mathbf{f}_i \tag{2.8}$$

with m_i the mass of particle i and f_i the forces acting upon particle i. $\mathbf{f}_i$ is the derivative of the imposed interaction potential V (essentially, the interactions with all neighbouring particles will exert forces onto particle i). Very small integration steps are used to calculate $\mathbf{r}_i(t+\delta t)$ and $\mathbf{v}_i(t+\delta t)$ and after each calculation the forces acting upon the particles are re-evaluated to prepare for the next step. The most commonly used forward integration scheme is the velocity Verlet approach, which utilises Taylor expansions.

From these considerations, macroscopic quantities of the simulated system can be determined, such as the equilibrium structure of the particles or for example the pressure of the system.

In the current research, the interactions of colloids suspended in a solvent need to be evaluated. Such systems are difficult to simulate using MD, as inclusion of explicit solvent molecules (generally vastly outnumbering the particles of interest) will result in very costly simulations.

For this reason, we also employ Langevin dynamics (LD) simulations, which are generally used to simulate exactly this kind of system. Because the properties of the fast-moving solvent molecules are not of interest, their averaged effect on the colloid is added to the equations of motion. The colloid thus experiences two additional forces: the frictional drag force γ (also know as drag coefficient) and a random force $\mathbf{R}$, which represents thermal motion. So through these two forces, the interactions of all solvent molecules are included into the simulations. If we are only interested in the dynamics of the large colloids, this approximation works well, as it is based on time scale separation: we focus on the dynamics of the large, sluggish colloids rather than the small, fast solvent molecules.

The Langevin equation of motion for a particle i are thus:

$$m_i \frac{d\mathbf{v}_i(t)}{dt} = -\mathbf{f}_i - \gamma \mathbf{v}_i(t) + \sqrt{2\gamma k_{\mathrm{B}} T}\mathbf{R}_i(t) \tag{2.9}$$

where $\mathbf{R}_i(t)$ is the random force, whose strength is related to the drag coefficient γ via the fluctuation-dissipation theorem. The random force is uncorrelated in time and space, and its time average is zero. It is also known as white noise, and simulates the large number of random solvent-colloids collisions that occur in a time step δt.

The drag coefficient γ can be related to the diffusion D of the colloids (under dilute conditions) according to the Einstein relation $\gamma = \frac{k_B T}{D}$. This connection is used to map the simulation time scale onto real time, as it all comes down to how fast the colloids move through the solvent.

We note that if the colloids experience no inertia (i.e., the overdamped limit), so that $\frac{d\mathbf{v}_i(t)}{dt} = 0$, the Langevin equation simplifies and the position $\mathbf{r}_i$ of particle i can be directly computed:

$$\frac{d\mathbf{r}_i(t)}{dt} = -\frac{\mathbf{f}_i}{\gamma} + \sqrt{2D}\,\mathbf{R}_i \tag{2.10}$$

which is known as Brownian Dynamics.

For the structural properties at equilibrium, the results from LD and MD will be equivalent: particle position is dictated by the set interaction potential only. However, when considering the dynamical properties, LD simulations are able to simulate realistically the velocity of microgels suspended in aqueous solution, in contrast to MD simulations. Therefore, LD and MD will yield the same resultant pair correlation function $g(r)$ while LD can provide the mean squared displacement MSD as well. In the research described in Paper I, particles were simulated with 4% polydispersity to mimic the real-life experiments. In addition, for all described simulations, the z-coordinate from the configuration was randomly displaced with Gaussian noise centered around unity with standard deviation 0.005-0.02. This approach is taken to ensure that the experimental 2D and 3D $g(r)$s can be successfully compared to the simulated 3D $g(r)$ (36). The simulation time scale of the MSDs is mapped onto real time using the same diffusion coefficient D for all state points at at similar temperature and solvent viscosity.

2.4 Passive microrheology

Microrheology is a relatively new tool in rheological studies, which focuses on the flow of matter. Instead of conventional rheology, for which 1-10ml of sample is needed, microrheology requires only 1-500 μl, which opens up new avenues for studies on precious material, such as eye lens proteins. Rather than following the visco-elastic behaviour of a sample directly, in microrheology tracer particles are embedded into the suspension: as the particles explore their local surrounding, their diffusion coefficient will indirectly reflect the rheological properties of the medium. In this work, we concentrate only on tracking the zero shear viscosity η of the medium. Because viscosity is linked to long-time diffusion, the long-time diffusion coefficient of the tracer particles needs to be measured.

Although it sounds straightforward, there are several requirements that the system need to meet. The tracer particles need to be well-defined in size and non-interacting. Generally, charge stabilised polystyrene (PS) particles are used, but these aggregate in protein samples where the buffer screens charges. More successful are sterically stabilised particles. Tracer particles need limited interactions with the medium they probe, which can be a challenge in protein systems.

Two main classes of microrheology exist: active and passive microrheology. In 'active' microrheology the response of the sample is measured while the tracer particle is actively dragged around, for example utilising optical tweezers. 'Passive' microrheology is aptly named, as the motion of embedded tracer particles is simply followed in time. This is a non-invasive technique, which relies solely on thermal motion of particles. We depended exclusively on passive microrheology for Papers VI and VII, which we will expand upon in more detail.

2.4.1 DLS-based microrheology

One branch of passive microrheology involves optical techniques such as dynamic light scattering (DLS). In short, samples are created with a relatively high tracer particle concentration, so that scattering from the particles dominates compared to scattering from the medium of interest (which can still scatter a lot by itself). It is an elegant way to drown out the sample medium response, and track the motion of tracers solely. The autocorrelation function g_2 can then be used to obtain the diffusion coefficient of the tracer particles, as explained before. However, a key difference with size determination via DLS is that in optical microrheology, the size of the particles is known and well-defined. Thus, we extract a different variable from the Stokes-Einstein equation: $\eta = \frac{k_B T}{6\pi D R_H}$. Dividing the found η by the viscosity of the solvent η_0 then leads to the relative viscosity η_r of the examined sample.

2.4.2 MPT-based microrheology

A second branch of passive microrheology involves multiple particle tracking (MPT) based on confocal microscopy videos. Using confocal laser scanning microscopy (CLSM), videos are created of fluorescent tracer particles submerged in the sample.

Unlike DLS-based microrheology, additional resolution is won as the individual tracer particles can be observed, which opens up avenues for exploring heterogenous samples.

Particles are tracked using the standardised Crocker and Grier scripts in IDL (149). From this analysis, the 2D mean squared displacement (MSD) can be calculated (Figure 2.6a-c). The 2D MSD is defined as $\langle \Delta x^2 + \Delta y^2 \rangle = 4D\tau + (V\tau)^2$ (with V error introduced by instrument drift), and describes how much a particle moves on average in the x- and y-direction during a certain time step τ. The slope of the MSD is related to the diffusion coefficient D of the particles. For example, in Figure 2.6c the MSDs of three distinctly different regions (as indicated in Figure 2.6a) are shown. This particular video follows the crystallisation of a sample. In region 1 (yellow), the tracked particles show unhindered diffusive motion, as indicated by their slope. Region 2 (green) shows slowed down dynamics and the MSD of region 3 (blue) has plateaud, signifying an arrest.

The MSDs in this work have been time- and ensemble-averaged. In other words, the displacements of all tracked particle have been considered throughout the entire video, and averaged to create one MSD. The MSD can be plagued with low statistics and the diffusion coefficient is sensitive to small changes in the MSD slope, which can have far-reaching effects on any rheological properties derived from it (158).

Therefore, we do not extract D from the initial slope of the MSD, but instead calculate the so-called Van Hove function, and extract the diffusion coefficient from the general width of the Van Hove function.

In short, the one-dimensional Van Hove function $P(\Delta x, \tau)$ is a probability density function, describing the probability of a particle moving a certain distance Δx during a certain lagtime τ. The shape of the Van Hove function is thus instrumental in determining whether tracer particles experience a heterogeneous or homogenous sample environment: any trapped particle displays a low chance to move a certain distance, while any 'free' particle can move large distances (159). For example, Figure 2.6d shows that for each region separately, a Gaussian of different width can be fitted to $P(\Delta x, \tau)$. The width is then related to the different local diffusion coefficient. However, if the displacements from all three regions are considered in one overarching $P(\Delta x, \tau)$, the shape becomes distinctly non-Gaussian (red symbols).

For purely diffusive motion, the Van Hove function will take a Gaussian distribution, so that:

$$P(\Delta x, \tau) = (4\pi D\tau)^{-1/2} \exp(-\langle \Delta x^2(\tau) \rangle / 4D\tau) \tag{2.11}$$

The non-Gaussian parameter α_2 indicates how well the experimental Van Hove function fits to a theoretical Gaussian function: if $\alpha_2 = 0$, the distribution is perfectly diffusive and suggests a homogeneous sample environment. If $\alpha_2 > 0$, the tracer particles experience heterogeneous micro-environments (159). In one dimension, it is defined as $\alpha_2 = (\langle \Delta x^4(\tau) \rangle / 3 \langle \Delta x^2(\tau) \rangle^2) - 1$.

Following Josephson et al. (Ref. (160)), we test at which lag time τ the non-Gaussian parameter α_2 statistically speaking indicates a Gaussian shape of the Van Hove function, and choose the lag time with the highest statistics. Only the motion at this particular lag time is then taken into consideration to calculate the diffusion coefficient. Using the Stokes-Einstein equation (Eq. 2.7) as shown previously, the viscosity of the sample can be calculated.

2.5 Densification of samples

2.5.1 Preparation of highly concentrated microgel suspensions

The long-term storage of microgel needs to be given some thought, as bacterial growth within the microgel stock suspension is a reality (161). After synthesis and purification, the microgels used in this research were freeze-dried to increase shelf-life. An advantage of lyophilisation is the precise control over the wt% of the sample. Other preservation techniques include a small addition of NaN3, which inhibits bacterial growth, or the acidification or alkanisation of the batch.

The freeze-drying process does not affect the microgels (162), but during the lyophilisation the microgel networks get entangled. Therefore, a long time needs to be allocated for microgel redispersion in sample preparation. The densification of microgel samples can thus lead to some headaches: a suspension of freeze-dried microgels is unlikely to homogenise at extremely high volume fractions (beyond ∼10wt%) despite continuous sample agitation for weeks/months.

In order to create the dense samples used in Paper II, we therefore rely on a different approach. The stock solution was created at low density, e.g. 150ml of a 1wt% microgel suspension. After several weeks of continuous agitation, the sample was checked in the confocal microscope for aggregates. Once the number of dimers and trimers is sufficiently reduced, the sample is transferred into a dialysis membrane (Biotech CE Membrane tubing 24 mm, 0.1-0.5 kDa). The dialysis membrane contains tracer

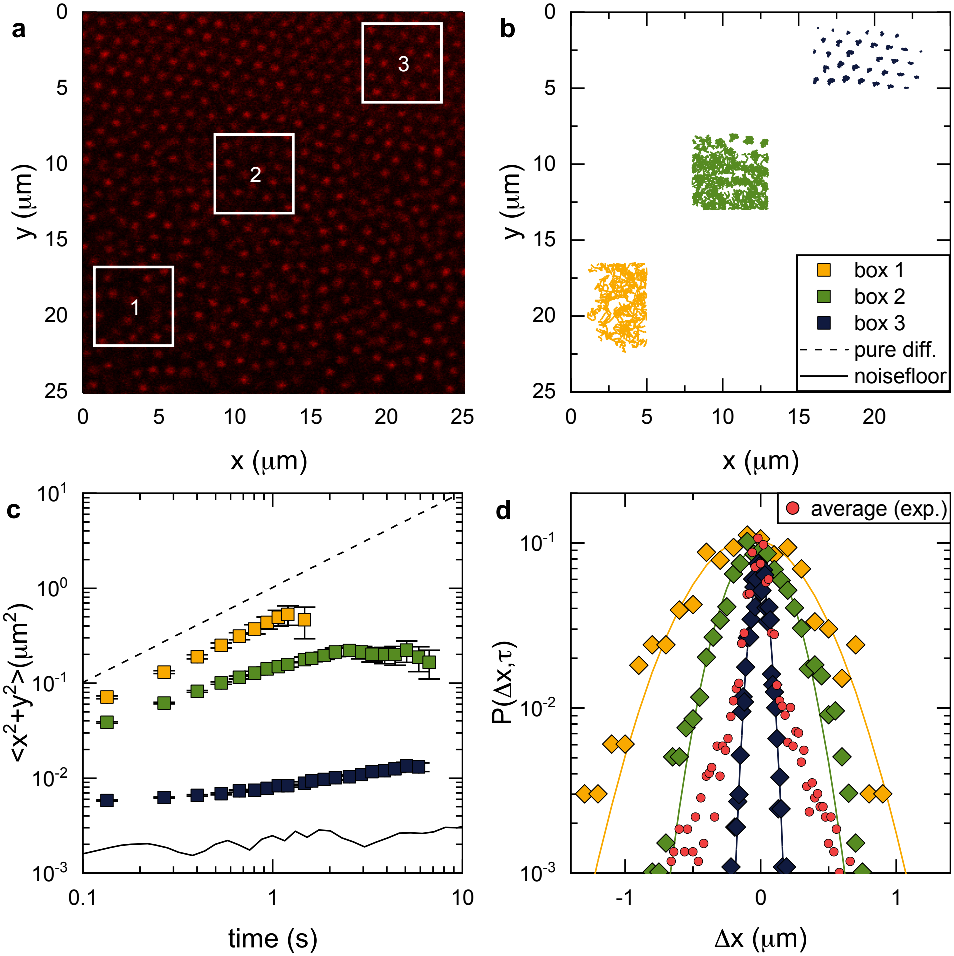

Figure 2.6: **Dynamical analysis of a heterogeneous sample.** a: Typical confocal micrograph, with three boxes indicating different states (1: liquid, 2: liquid-crystal, 3: crystal). b: Particle tracks for each box obtained from quantitative image analysis. c: Mean squared displacements for each regime reveal their different diffusivity. The liquid state is purely diffusive, while the crystalline state is arrested. d: Corresponding Van Hove functions. Each separate region can be fitted with a Gaussian, indicating homogeneous diffusion within the region. The average Van Hove function for all traced microgels is also shown (red), which possesses a clearly non-Gaussian shape.

amounts of NaN_3 and was rinsed before use; we note that if used in pure water, bacterial growth will commence and affect the sample within weeks.

Instead of using pure water, the dialysis membrane is submerged in 8wt% poly(ethylene glycol) (PEG) solution. PEG is known for its strong osmotic pressure, and at 8wt% it exerts an osmotic pressure of ~ 2 atm. The pressure forces the water out of the dia-

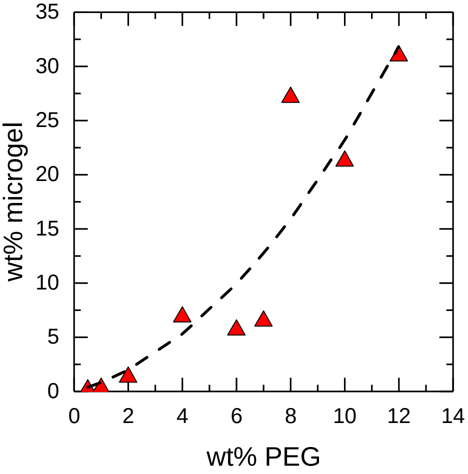

Figure 2.7: Effect of PEG on microgel concentration. Increasing PEG leads to increased concentration of microgel. Red triangles are datapoints, the dashed line is a polynomial fit.

lysis membrane over the course of a few days. By choosing different concentrations of PEG, the sample can be concentrated at will to any volume fraction, although this remains system-dependent (Figure 2.7). In order to keep reproducibility high, the dialysis setup should be temperature-controlled.

Once the sample is sufficiently dense, the dialysis membrane can be rinsed with MilliQ water to prevent contamination with PEG. The sample can then be retrieved from the dialysis membrane and stored accordingly. The approach knows several disadvantages. First, because of the high concentrations involved, the sample dries out rapidly. Secondly, the extremely small sample volume after densification (< 5ml) obstructs a thorough gravimetrical determination of the wt%. Thirdly, the obtained sample from the dialysis tube can be somewhat heterogeneous, and mixing of the sample is troublesome due to its paste-like properties. The resulting uncertainty or error in concentration can be corrected by subsequently measuring the number density directly in-situ using CLSM on arrested or (ideally) crystalline samples.

2.5.2 Creating protein samples beyond the arrest transition

Protein samples, the key players in (Papers VI and VII), are extremely difficult to handle at volume fractions close to the arrest transition. Not only is the lack of sample often a problem (γ_B-crystallin), during densification via centrifugation the protein can clog up the filters (lysozyme). Although not irreversibly clogged, this blocks solvent

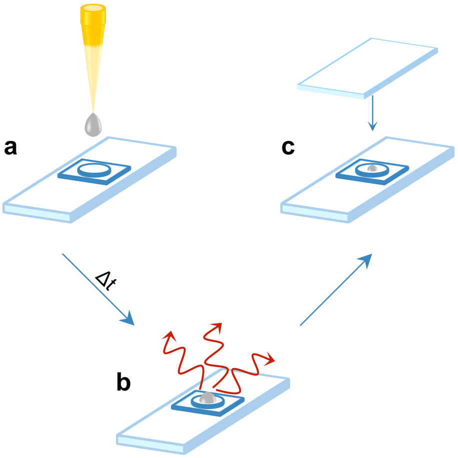

Figure 2.8: Schematic of evaporation procedure. **a:** A droplet with moderate protein concentration is carefully pipetted onto a glass slide with spacer sticker cell. **b:** Water evaporates from the droplet over time. **c:** The sticker cell is sealed with a coverslip to halt evaporation.

from passing through the filter and thus limits further concentrating. In order to create protein concentrations necessary to experimentally scrutinise the liquid-solid arrest in these systems, we therefore need a different approach.

We created moderately dense samples via ultra-centrifugation, and mixed in the tracer particles - which infers a dilution on the protein samples. A confocal sample cell was fully cleaned, dried and prepared beforehand. The procedure is described graphically in Figure 2.8. We placed the sample cell including cover slip on a balance with 5 decimal accuracy, deposited a 5 μl protein sample droplet, and recorded the weight immediately after deposition. Simultaneously, we note the evaporation starting time. After waiting several minutes, the cover slip is carefully pressed onto the sample cell, which breaks the droplet structure. Especially at higher concentrations, considerable force had to be applied to fully seal the sample cell. The moment of sealing is noted so that the exact evaporation time can be calculated, and the sample cell is weighed again to determine how much solvent has evaporated. We confirmed that once sealed, the sample cell does not reduce in weight over the span of 7.5 hours. In this way, we use evaporation to densify the protein samples, and reach extremely high volume fractions (Figure 2.9).

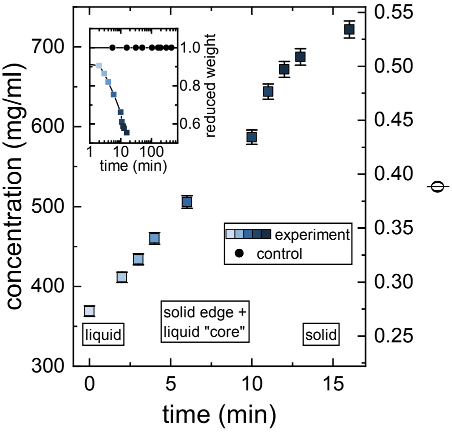

Figure 2.9: Increase in concentration as function of evaporation time. The concentration of the samples is given on the left y-axis, the corresponding volume fraction on the right y-axis. The different macroscopic appearances are indicated also. Inset: the control experiment did reduce in weight over the span of 7.5 hours.

3 | Results

3.1 Interactions between neutral microgels

3.1.1 Exploring microgel interactions via depletion attraction

The relationship between the rich phase diagram of microgels and their temperature-dependent interactions is a knowledge gap in microgel research; many works have used microgels under the incorrect assumption that they interact via hard sphere-like repulsions until the VPTT. The first key question of this thesis is therefore to define an interaction potential for neutral microgels which captures both the temperature-dependent and concentration-dependent phase behaviour.

In order to answer this question, we carried out several studies which encompass both experimental and numerical work. In the first work (Paper I), we created 12 samples, where 3 samples contained one type of large, fluorescently labeled microgels and 9 were mixtures with an additional population of smaller, unstained microgels. The small microgels - unseen by confocal microscopy - induce a depletion attraction on the large microgels. For this reason, the small microgels are referred to as 'depletants' and the large microgels as 'colloids'. Using CLSM and quantitative image analysis, we can thus extract structural and dynamic information of the colloid microgels over a range of concentration and temperature. The depletion attraction effectively forces the colloid microgels together, so that we can reveal the 'hidden' effect of the dense core, loose shell paradigm structure.

The experimental structural and dynamical information - which spans the liquid regime of the microgels and T=15-30°C - is then compared to their numerical counterparts, generated via molecular dynamics (MD) and Langevin dynamics (LD) simulations. We first test the Hertzian interaction potential, for which literature has shown

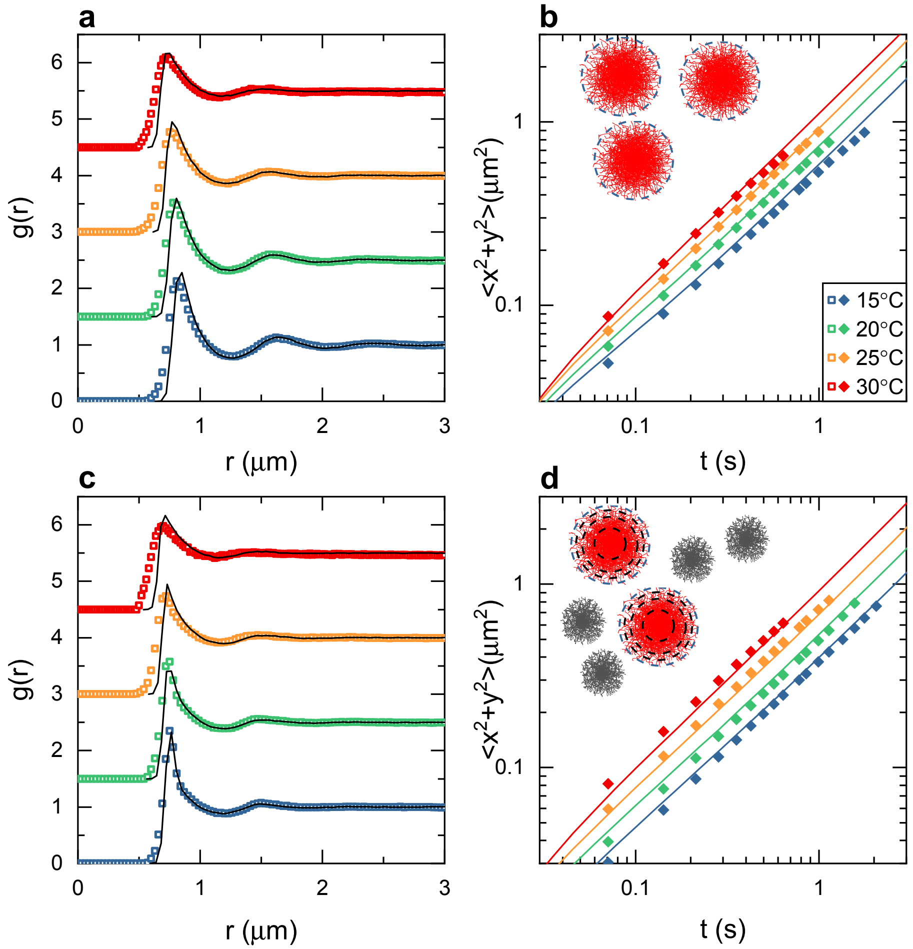

Figure 3.1: Temperature-dependent structural and dynamical signature of the liquid phase for two microgel samples. Symbols denote experimental data, solid lines are fits. The colour legend indicates temperature and applies to all panels. **a:** $g(r)$s for one sample containing only large fluorescent microgels with $\phi_{\mathrm{eff}} = 0.49$, 0.42, 0.37, 0.29 at 15, 20, 25, 30 °C. Structural correlations decrease with increasing temperature, as the volume fraction is lowered. A good fit is obtained using an increasing Hertzian soft-repulsion for interactions. **b:** Dynamics for the same sample. The motion of the microgels increases with higher temperature, which is followed by the Hertzian prediction. **c:** $g(r)$s for one mixture with $\phi_{\mathrm{colloid,eff}} = 0.49$, 0.42, 0.37, 0.29 and $\phi_{\mathrm{depletant,eff}} = 0.30$, 0.28, 0.26, 0.24 at 15, 20, 25, 30 °C. The $g(r)$ becomes more asymmetrical and sharply peaked compared to panel **a**. Data is fitted with the multi-Hertzian model. **d:** Dynamics for the same sample with fits based on multi-Hertzian.

the most promise (36). The Hertzian has been thoroughly tested at a single temperature before, which raises the question if it can capture temperature-dependent interactions. In addition, the Hertzian repulsion does not consider the core-shell structure of the microgel, so that we expect the model to break down once microgels probe denser, inner regions. The Hertzian repulsion can be described as:

$$\begin{aligned} V^{\mathrm{H}}(r,T) = {} & \epsilon_{\mathrm{H}}(T)(1-\frac{r}{\sigma_{\mathrm{eff}}})^{5/2}, \quad (r \leq \sigma_{\mathrm{eff}}) \\ = {} & 0. \quad (r > \sigma_{\mathrm{eff}}) \end{aligned} \tag{3.1}$$

An advantage of this potential is that the parameters required for the Hertzian repulsion can be obtained mostly experimentally: the temperature T can be set, and the effective diameter σ_{eff} is equal to the temperature-dependent hydrodynamic diameter σ_{H}, which can be obtained via DLS. Combined with the experimentally determined number density N_{p}, the volume fraction can be calculated as $\phi_{\mathrm{eff}} = N_{\mathrm{p}}\frac{\pi}{6}\sigma_{\mathrm{H}}^3$. The only 'free' parameter which remains is then the Hertzian interaction strength $\epsilon_{\mathrm{H}}(T)$, which has been empirically determined to be around 500-1000 $k_{\mathrm{B}}T$ (35; 36).

We scrutinised the $g(r)$s for the 3 samples containing colloid microgels only. As shown in Figure 3.1a, the $g(r)$ becomes more correlated with increasing volume fraction and decreasing temperature. The volume fractions at 15 °C were adjusted until good correspondence was found, using initial estimates based on viscometry. Based on the microgel swelling, volume fractions at 20-30 °C could be inferred. The Hertzian interaction strength was varied starting with the literature value of 500 $k_{\mathrm{B}}T$ at 20 °C (36). We find that the Hertzian model captures all g(r)s (Figure 3.1a), and that the soft repulsion becomes steeper with increasing temperature, suggesting that the repulsions between microgels grow before the VPTT (Figure 3.2a). Yet, beyond the VPTT, literature tells us that van der Waals-attractions dominate. The data shown in Figure 3.1b also confirms that the Hertzian potential captures the dynamical behaviour.

If we add the depletion attraction to the simple repulsive Hertzian to describe the large microgel interactions, the calculated interaction potentials predict instantaneous aggregation of all mixtures: the depletion interaction - even at minimal attraction strength U_{depl} = 20 $k_{\mathrm{B}}T$ - completely overshadows the soft repulsion as established for one-component microgel systems (Figure 3.2b left column; the steep negative curves indicate strong attractions). However, all experimental mixtures are stable. The Hertzian interaction potential coarse grains any inhomogeneity in the microgel internal structure, and instead paints an oversimplified picture of the network. Once microgels begin to interpenetrate each others' networks, the dense core is expected to start influencing the interactions. It is therefore no surprise that as soon as microgels are forced closer together, the Hertzian model breaks down. In other words, the core repulsion of the large microgels - neglected by the Hertzian model - prevents the predicted aggregation.

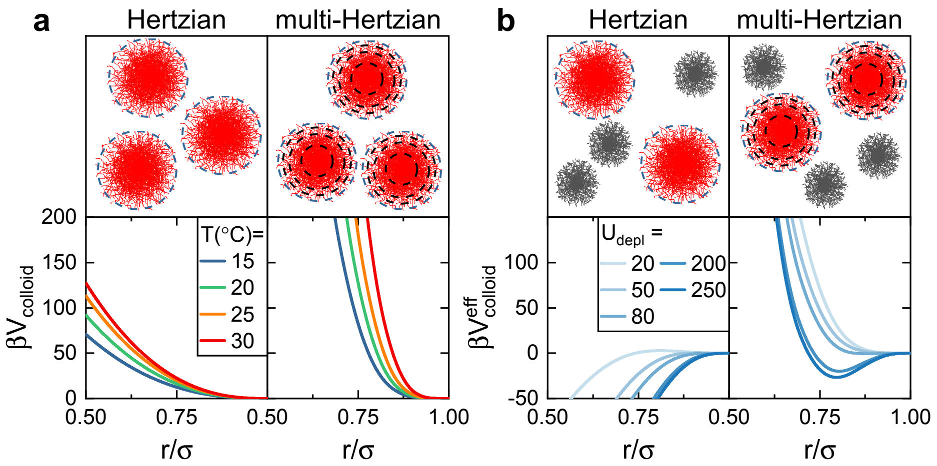

Figure 3.2: **Theoretical interaction potentials for neutral microgels based on a simple Hertzian or a multi-Hertzian.** **a:** Temperature dependence of microgel-microgel interactions in a one-component system. **b:** Effective interaction between microgels experiencing an additional depletion attraction at 15°C. Even at low attraction strength $20 k_B T$, the system is predicted to aggregate.

We therefore develop a multi-Hertzian model, which in basis is a series of shells, each with its own elastic properties, defined as:

$$\begin{aligned} V^{\mathrm{MH}}(r,T) = &\quad \epsilon_{\mathrm{core}}\left(1-\frac{r}{\sigma_{\mathrm{core}}}\right)^{5/2}, && (r \leq \sigma_{\mathrm{core}}) \\ + &\quad \epsilon_{\mathrm{mid}}(T)\left(1-\frac{r}{\sigma_{\mathrm{mid}}}\right)^{5/2}, && (r \leq \sigma_{\mathrm{mid}}) \\ + &\quad \epsilon_{\mathrm{corona}}(T)\left(1-\frac{r}{\sigma_{\mathrm{corona}}}\right)^{5/2}, && (r \leq \sigma_{\mathrm{corona}}) \\ + &\quad \epsilon_{\mathrm{H}}(T)\left(1-\frac{r}{\sigma_{\mathrm{eff}}}\right)^{5/2}, && (r \leq \sigma_{\mathrm{eff}}) \\ = &\quad 0. && (r > \sigma_{\mathrm{eff}}) \end{aligned} \tag{3.2}$$

Each shell (defined by the distances σ_{core}, σ_{mid}, σ_{corona}, σ_{eff}) corresponds to the elastic properties of a region of the microgel (Figure 3.3) and contributes its own Hertzian strength (ϵ_{core}, ϵ_{mid}, $\epsilon_{\mathrm{corona}}$, ϵ_{eff}, respectively). The outer shell is equivalent to the previously established Hertzian, and describes the elastic contributions from the corona and dangling ends. In this way, we ensure that in the liquid regime where shell interactions prevail, the multi-Hertzian model reproduces the earlier findings based on the Hertzian model. The inner-most shell is assigned a strong elastic interaction, as

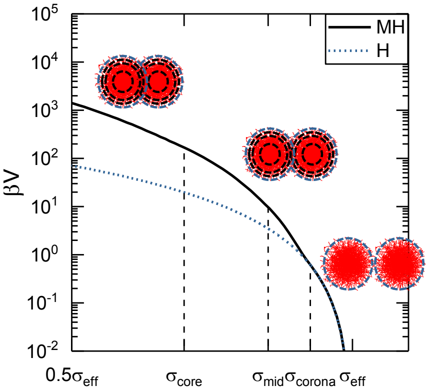

Figure 3.3: Differences between the simple Hertzian (blue dashed line) and multi-Hertzian (solid black line), where an additional interaction term becomes active at length scales σ_{core}, σ_{mid}, σ_{corona}.

the crosslinker density is much higher in the core. We then added two more shells to create a gradual increase of the interaction potential - mimicking the distribution of crosslinker - rather than a sharp step function. The resultant potential is steeper compared to the simple Hertzian, but it will only have an effect once microgels start to interpenetrate (Figure 3.3). The multi-Hertzian is thus a more realistic representation of the microgel structure, and finds root in theoretical considerations, as we will describe in a later section. Ideally, the model can be filled in using mostly experimentally available parameters, retrieved from small angle x-ray scattering (SAXS) experiments - as described in more detail in Paper I.

We ensure that the multi-Hertzian model is equivalent to the Hertzian model in the liquid regime by setting the shell interactions to the same Hertzian strength as found for the one-component system. When we now consider an additional depletion attraction, we find that the core repulsion of the multi-Hertzian counterbalances the attraction, so the stable experimental mixtures are reproduced (Figure 3.2b, right column). The effect of depletion attraction on the $g(r)$ is noticeable: the first peak of the $g(r)$ becomes more asymmetrical, with a peak shift to lower r and a taller first peak (Figure 3.1c). These effects are captured by the multi-Hertzian for all investigated state points, i.e. 12 samples at 4 different temperatures. In addition, the dynamical signature of the system is reproduced by the interaction potential (Figure 3.1d).

We have thus created a model which follows the crosslinker density of the microgel, so that dense inner regions are difficult to compress while the outer shell possesses softer repulsion. The correspondence to experimental data shows that such a multi-Hertzian model is better than a simple Hertzian to reproduce the structural and dynamical signature of the microgel system, although the true effect will remain somewhat hidden for single component systems where the core region is not necessarily accessed. We expect that the core repulsion will become important for systems where microgels are drawn close together, for example at ultra-high density or in the presence of an external field.

3.1.2 Does the (multi-)Hertzian hold for dense systems?

In the second work revolving around the interplay between microgel interactions and phase behaviour, we test the applicability of the (multi-)Hertzian model on dense, one-component microgel systems. A large range of samples was created to span the entire phase diagram, i.e. from $\phi_{\text{eff}} = 0.05$ to $\phi_{\text{eff}} = 1.95$, which we then characterised at $T = 15, 20, 25, 30°\text{C}$ using confocal microscopy and quantitative comparison to theory. The aim of this work is three-fold. First, we further test the (multi)-Hertzian potential and its ability to correctly reproduce key structural and dynamic properties of microgels over a large range of volume fractions and temperatures. Second, we hope to pinpoint at which volume fraction the Hertzian starts to deviate, signifying the concentration at which microgels start to significantly interpenetrate. Third, we explore the phase behaviour of soft microgels in overpacked state, which is an interesting region of the phase diagram, but experimentally difficult to reach.

Confocal microscopy videos were collected from 22 samples at 4 temperatures, so that a total of 88 state points can be considered. We therefore start our investigation in the dilute regime of the phase diagram. We first specify the two key parameters σ_{eff} and ρ (interaction diameter and number density, respectively) which are essential to calculate the effective volume fraction $\phi_{\text{eff}} = \frac{4\pi}{3}\rho\left(\frac{\sigma_{\text{eff}}}{2}\right)^3$ of the experimental system. From our previous considerations, we have established that the hydrodynamic diameter σ_{H} works fairly well as interaction diameter σ_{eff}, at least in the liquid regime. Therefore, dynamic light scattering measurements on dilute samples containing solely fluorescent microgels were performed. The confocal microscopy study is executed in the presence of 0.1 M KCl, to suppress any possible contributions from residual charges to the interaction potential. For this reason, two swelling curves (in the presence and absence of 0.1 M KCl) are shown in Figure 3.4 (red squares and circles). Indeed, a small effect of increased salinity can be noted.

Two crystalline samples at 15 °C allow us to extrapolate the experimental number density ρ towards the extremely dilute regime. Combined with the (temperature dependent) hydrodynamic diameter, ϕ_{eff} can thus be calculated.

The resultant structural correlations (Figure 3.5, left) and dynamical properties (Figure 3.5, right) compare well to their numerical counterparts, based on the Hertzian model with parameters as described in Section 3.1.1. The results reproduce our previous findings, so that we can confirm extended use of the Hertzian model throughout the entire liquid regime, at temperatures below the VPTT (35; 36; 163).

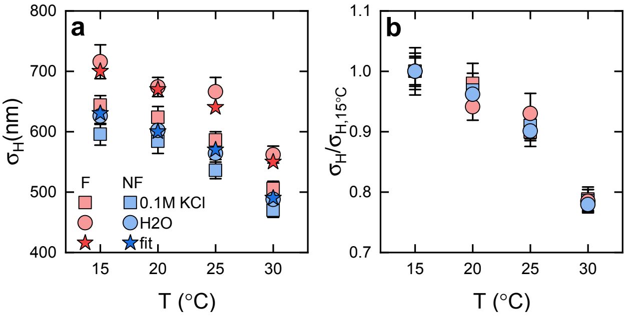

Figure 3.4: Absolute (a) and relative (b) hydrodynamic diameter σ_H as function of temperature. Fluorescent (F) microgels are indicated with the red symbols, non-fluorescent microgels (NF) with the blue symbols.

Any deviations between the multi-Hertzian (includes core repulsion) and the Hertzian (excludes core repulsion) signal that microgels start to experience interactions beyond the shell. We therefore confront the numerical results for the densest liquid state point at 15°C for both models (Figure 3.6). Indeed, only a marginal difference is found, reasserting that throughout the entire liquid phase, shell interaction dominate.

We thus shift our focus to interactions in the arrested state. To this extent, samples were created based on a mixture of 28% fluorescent and 72% non-fluorescent microgels, which have been synthesised in the same way. By measuring on a mixture with an 'invisibile' component, we hope to alleviate typical imaging issues at high densities such as a high background fluorescence and signal overlap between neighbouring particles. Unfortunately, dynamic light scattering measurements signify that the unstained microgels are slightly smaller ($\sigma_\mathrm{H} = 0.6\mu$m at 15°C) than the fluorescent ones ($\sigma_\mathrm{H} = 0.7\mu$m at 15°C) so that the effective polydispersity within the system is larger compared to the single-component system.

Despite the differences in make-up, samples from both concentration series with equivalent weight percentage overlap well in number density and mean squared displacements. Yet, the increased polydispersity carries two consequences. First, crystallisation is suppressed, which becomes evident when considering the MSDs (Figure 3.7) and $g(r)$s (Figure 3.8) from the densest liquid state points at 15°C: the single component system resides in a crystalline order, while the polydisperse binary mixture still follows liquid behaviour. Secondly, the $g(r)$ appear markedly different at first glance: the binary mixture $g(r)$ displays a softened and broadened first peak ((Figure 3.8).

We therefore increase the polydispersity within the theoretical framework. In the single component system, the particles possessed a size polydispersity of 4%, with 0.5% of noise in the $z-$coordinate. In order to approximate the binary system as a one-

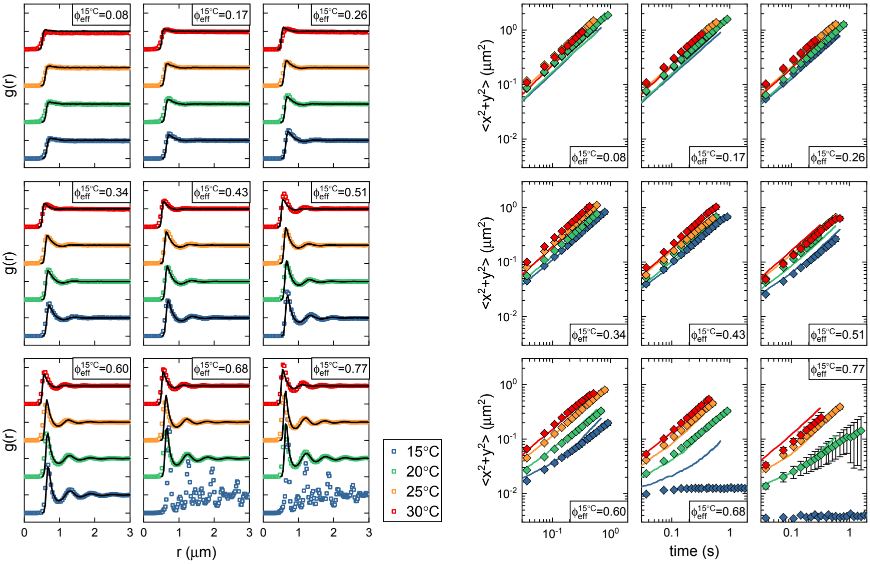

Figure 3.5: **Structural correlations and transport properties in the liquid regime of charge neutral microgels.** Each panel contains the experimental (symbols) data overlaid with numerical results from the Hertzian model (solid lines) for the same sample measured at 15-30 °C as indicated by the colour legend, depicting either the $g(r)$ (left set) or MSD (right set). Effective volume fractions at 15 °C are given for each panel. The two densest state points crystallised at 15 °C.

component system, the noise is increased to 3%, which is equivalent to the theoretical polydispersity of 2.9% arising from the mixture and not unreasonable (36). In this way, we recover the correspondence between experiment and theory.

Unfortunately, because only 28% of particle positions are captured, statistics are low - for this reason, only experimental structural data at 15 and 20 °C are shown for $\phi_{\text{eff}} = 0.58 - 1.30$. Data at higher ϕ_{eff} or temperatures displayed a marked decrease in $g(r)$ quality.

Regardless, we compare the remaining data with either the Hertzian or the multi-Hertzian in Figure 3.9. The theoretical $g(r)$ have a tendency to overestimate the first peak height in the dense liquid, echoing findings for the single component system. In contrast, once the system arrests, the non-monotonic rise and fall of the first peak maximum g_{max} is not reproduced with either model; rather, the simulated peak height plateaus. On the other hand, first peak positions are consistent (whereas higher order maxima appear slightly out of sync). The position of the first $g(r)$ peak can be related to the number density according to $a_s \sim \rho^{-1/3}$ in case of soft potentials, or isotropic compression of the particles.We recall that the polymeric nature of the mi-

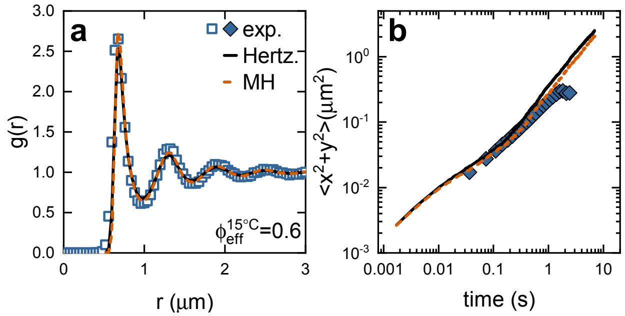

Figure 3.6: Comparison of Hertzian and multi-Hertzian model for state point $\phi_{\text{eff}}^{15^\circ\text{C}} = 0.77$. Panel **a** and **b** display the structural and dynamical information, respectively. Experimental data is represented with symbols, the models are indicated with lines.

crogel lends it an inherent softness and flexibility. Using the size of the microgel under high dilution to represent dense packings is therefore, perhaps, a naive assumption. Recent efforts underline how the deformability of the microgel network results in various morphological regimes under dense packing, so that we will consider several scenarios for the microgel diameter in the arrested state (46; 47; 164).

In the work by Mohanty *et al.* (47), the onset of isotropic shrinking was determined at $\phi_{\text{eff}} = 1.05$ (at 15°C). Ghosh *et al.* (165) identified this turning point as the first glassy state point, i.e. where g_{max} is maximal. In both cases, the isotropic compression essentially means that once more microgels are added to the system, all particles shrink so that the effective volume fraction remains constant.

However, as shown in more detail in Paper II, fit quality is not necessarily improved adopting a flexible radius. If we follow the route from Ghosh et al. (165), the resultant $g(r)$ consistently underestimates the oscillations, although the peak positions are still correct. Between the constant size scenario and a reduced size starting at $\phi_{\text{eff}} = 1.04$, differences are not particularly notable. This is partly due to the moderate decrease in size between $\phi_{\text{eff}} = 1.04 - 1.3$ as dictated by the $\sim \rho^{-1/3}$ dependency. Effectively, our results signify that within the Hertzian elastic framework, a constant size works well to describe structural correlations up to $\phi_{\text{eff}} = 1.3$. Yet, the mismatches at higher order maxima remain, and are an indication that an additional contribution to the interaction potential might be lacking. We suspect an additional attractive component, caused by chain entanglements at such high packing fraction.

The reason for this suspicion can be found when examining the resultant phase diagram, based on all 88 state points (Figure 3.10). Crystallisation is only found for the single component system, so that we cannot comment on its appearance. The arrest

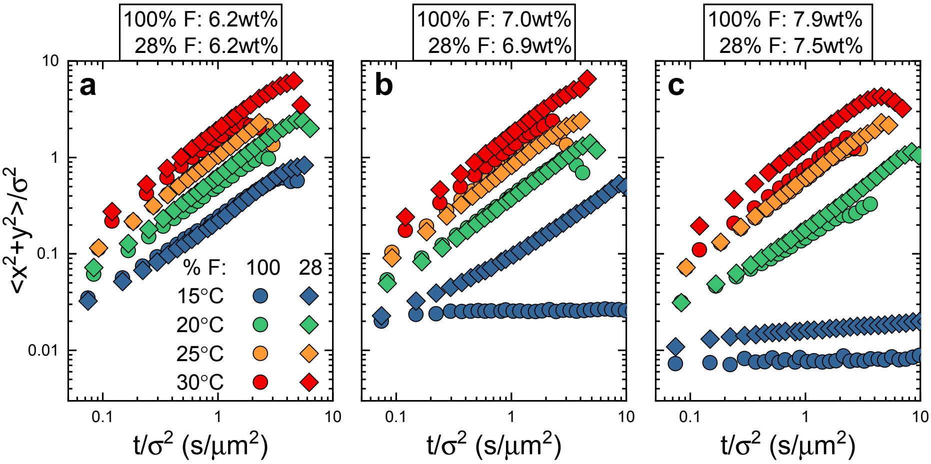

Figure 3.7: **Mean squared displacements for single component samples (circles) and binary mixtures (diamonds) with equivalent wt%.** Panels **a**, **b** and **c** indicate the three densest state points measured for the 100% fluorescent microgel samples. Axes are normalised by the temperature-dependent diameter of the microgels

line moves to higher volume fractions with decreasing temperature (i.e. increasing softness), which has been noted before and is in line with expectations. Most interestingly, perhaps, is the emergence of a strongly heterogeneous state at high packing fraction and temperature. In this state, the sample appears macroscopically turbid with large fracture lines. Such effects have been observed before, and have been related to the strong polymeric entanglements of the network at room temperature at such high packings (47). If the temperature is subsequently elevated, the microgel network attempts to shrink and so the interpenetrating polymer strands will exert forces on eachother. This willa ppear as an effetive attraction, so that we wonder how these entanglements willa ffect the structural ordering of the system.

Our result confirm once more the applicability of the 'standard' Hertzian model for describing microgel interactions spanning all corners of the liquid phase. Although additional experimental data is obviously required to observe changes in interaction at denser volume fractions and higher temperatures, up to effective volume fractions $\phi_{\text{eff}} = 1.3$, a constant size in combination with the rubberliker Hertzian response reproduces experimental structural ordering reasonably well. Testing various descriptions for microgel compression, we found that microgel compression likely occurs deep in the glass region rather than at the onset of the glass transition, in line with previous work (47). In addition, we note the emergence of a strongly heterogeneous, interpenetrated state which appears to have been relatively unnoticed in microgel research thus far. This peculiar state is a clear demonstration of the softness and ther-

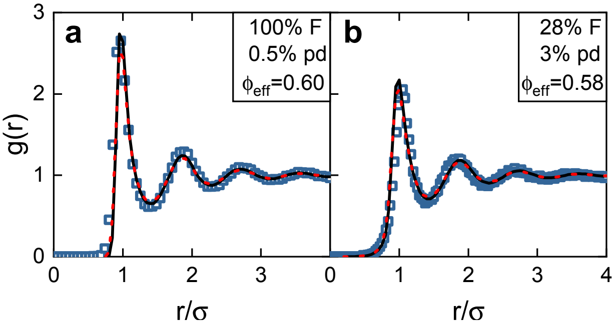

Figure 3.8: Structural correlations for samples from both concentration series with similar wt% at 15 °C. Panel **a** depicts the 100% fluorescent series while panel **b** shows the 28% fluorescent microgels in the presence of 72% unstained microgels. Experimental data is represented by squares. The solid black and dashed red line indicate fits with the multi-Hertzian and Hertzian, respectively. Axes are normalised by the temperature-dependent diameter of the microgels.

moresponsivity hosted by the microgel, and so the 'history' of a dense microgel sample is likely to have strong consequences for its exhibited properties.

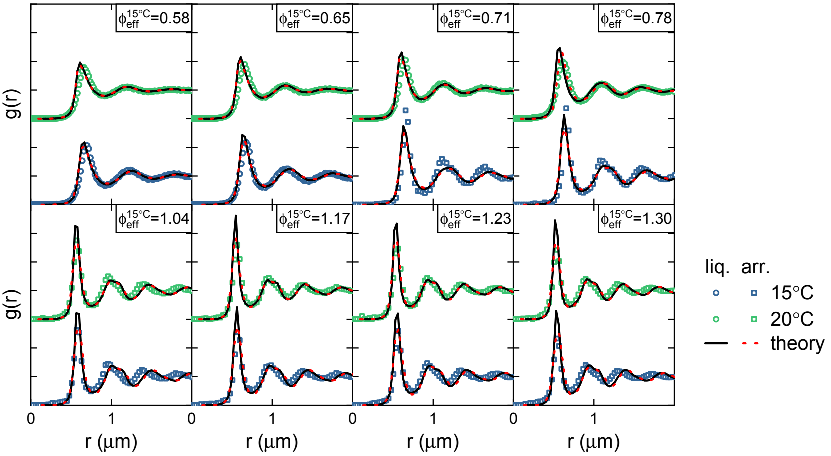

Figure 3.9: Structural correlations for mixtures at 15 and 20 °C. Experimental data is colour coded according to temperature conditions and symbol shapes indicate the liquid (circles) or arrested state (squares). Solid black and dashed red line represent fits with the multi-Hertzian and Hertzian, respectively. Each panel contains one sample.

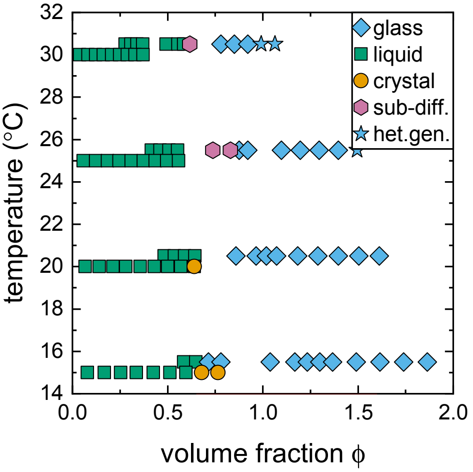

Figure 3.10: Experimental phase diagram based on all measured state points. The binary mixtures with 28% fluorescent microgels has been offset slightly in the y-direction (plus 0.5 °C) to distinguish from the 100% fluorescent, single component samples. Effective volume fraction is based on the constant effective diameter.

3.1.3 In silico synthesis of microgels creates realistic microgels

Although the Hertzian and multi-Hertzian model reproduce the elastic properties of the microgel network, they are in essence still rather phenomenological, i.e. a solid theoretical basis for the choice of this interaction potential is somewhat lacking. In Paper III, we therefore investigated the possibility of re-creating microgels *in silico*, where building a microgel from the ground up can tell us something about the predicted shape and interactions. In the Hertzian model, each microgel is considered as one unit, so that they possess only 1 degree of freedom each. In the simulations employed in this study, each microgel possesses N monomers (i.e. N degrees of freedom), where every monomer corresponds in size to the Kuhn length from polymer theory. A major advantage is thus the much smaller level of coarse-graining, which leads to a higher level of details within the microgel.

The microgels are created in a two-step approach. In the first step, a mixture of bivalent and tetravalent patchy particles is confined to a sphere and allowed to self-assemble. The particles with two patches represent the monomer, while the four-patches particles correspond to the crosslinker. Monomer-monomer and monomer-crosslinker connections are allowed, whilst crosslinker-crosslinker connections are restricted. After self-assembly is completed, the second step entails fixating all created bonds. The directional interaction between patches is replaced with a Kremer-Grest bead-spring model, which has been shown to realistically reproduce polymer interactions in a good solvent. Finally, an extra term in the interactions is added to all monomers, mimicking the solvopobic potential which provides the thermoresponsiveness to the microgel.

This approach results in simulated microgels with strikingly similar properties to real-life microgels (Figure 3.11a): by tuning the size of the confining sphere, larger or smaller microgels are created. A large number of crosslinker units results in a denser microgel with a smaller swelling response. The transition across the VPTT is also captured through the solvophobicity term.

The follow-up research (166) after the initial creation of simulated microgels reveals that the effective interactions between the simulated microgels can be described well with a cascade of Hertzians, as shown in Figure 3.11b: the open symbols denote the numerically calculated interaction potential, and the different lines correspond to Hertzian potentials with various strength and range. We can thus assert that the multi-Hertzian is more than just a phenomenological model.

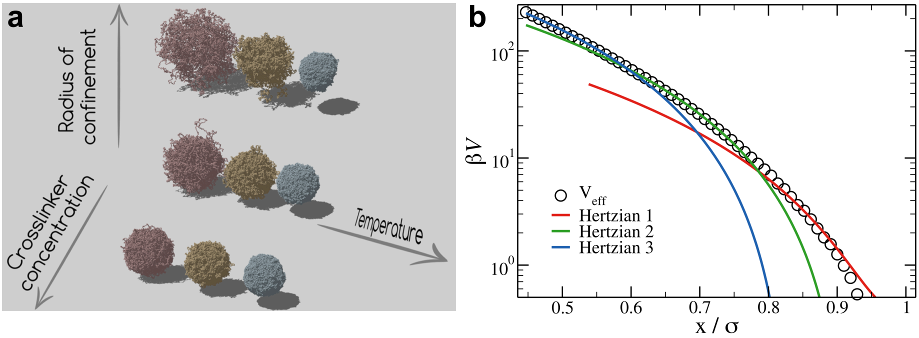

Figure 3.11: Characteristics of simulated microgels. **a**: Schematic detailing how the size and stiffness of simulated microgels can be altered following real-life parameters such as temperature and crosslinker concentration. **b**: The numerically calculated interaction potential derived from simulated microgels (open symbols) can be described well with a cascade of Hertzians of varying range and strength (solid lines), mimicking the multi-Hertzian developed in Paper I.

3.1.4 Key conclusions

- Hertzian interactions describe temperature-dependent shell interactions throughout all corners of the liquid phase below the VPTT
- The multi-Hertzian interaction potential captures the core repulsion, which is necessary when evaluating microgel systems with an additional attractive component
- In the overpacked state, both models work more or less, and adoption of a flexible size does not improve fit quality
- Deep polymeric entanglements at room temperatures can lead to a heterogeneous state at elevated temperatures with large internal stressess, so that the ‘history’ of a dense microgel suspension will affect its properties significantly
- In silico synthesis of microgels creates realistic microgels which exhibit multi-hertzian-like interactions

3.2 Interactions between ionic microgels

Intimate knowledge on the internal architecture - facilitated by literature efforts relating scattering experiments to the fuzzy sphere model - has allowed us to build a realistic interaction potential for neutral microgels, which hinges on the innate crosslinker density gradient and temperature-dependent solvent quality. In contrast, the incorporation of functional groups within the microgel generates a much more complex swelling response, sensitive to crosslinker density and charge distribution, as well as temperature, pH and salinity. The specific effect of each external trigger on the internal structure of PNIPAM-co-AAc (ionic) microgels has never been investigated in detail. In addition, no in-depth study has been performed to test the proposed interaction potential for ionic microgels. We must first understand the internal structure before we can explore the connection between interaction potential and phase diagram. The second key question of this thesis therefore revolves around the swelling response of ionic microgel networks to various charge regimes, and whether the proposed interaction potential is suitable for the swollen ionic microgel.

3.2.1 Influence of charge on microgel swelling

In Paper IV, we describe a light scattering study involving large, loosely crosslinked (1.5mol%) PNIPAM-co-AAc microgels suspended in different ambient environments, which lead to different charge regimes within the polymer network. The results allowed us to decouple the effect of salinity and pH on the core and corona swelling of the microgel. Using dynamic and static light scattering (DLS and SLS), we retrieved the hydrodynamic radius R_H and the form factor under dilute conditions at 15 °C. The hydrodynamic radius relies on the diffusivity of the particle, and so encompasses the dense core and loosely crosslinked corona. The dangling ends do not contribute much to the mass of the particle, and so they are 'invisible' in SLS. The experimental form factors were fitted using a Mie scattering algorithm (which includes factors such as polydispersity and backscattering), which allowed us to track the mass distribution within the microgel. The experimentally observed structural changes could be connected to classic polymer theory (Flory-Rehner), which describes the governing forces driving polymer network swelling.

In short, for neutral polymer networks, the steric repulsion between monomers leads to a certain degree of gel pressure, i.e. monomers position themselves as far away from each other as possible. This outwardly pointing force is counter-acted by the network elasticity, which can be controlled via crosslinker density (as the monomers are covalently bound to each other, they can only move so much). The Flory-Rehner theory has been used before on microgels, yet we note that in the classic sense, it does not consider the inhomogeneous crosslinker density of the microgel (68; 167). We therefore calculated swelling profiles of microgels with a radially varying crosslinker density using a multi-shell approach. Here, the radial and orthogonal extension of every single shell depends on its radial position, as well as the radial positions of the neighboring shells (68). We employ a modified Flory-Rehner theory with an additional third swelling term, representing the pressure Π_{charge} caused by electrostatic repulsion from deprotonated acrylic acid moieties. The pressure within the polymer network $\Pi(\phi)$ can then be described as follows:

$$\Pi(\phi) = \frac{3}{5} B_{\mathrm{ref}} \left[\left(\frac{\phi}{\phi_{\mathrm{ref}}} \right)^{2} - \left(\frac{\phi}{\phi_{\mathrm{ref}}} \right)^{1/3} \right] + \Pi_{\mathrm{charge}}(\phi), \tag{3.3}$$

where ϕ is the gel volume and the positive terms denote outward-pointing forces, while the negative term indicates the counterbalancing network elasticity. The elastic modulus B_{ref} is a material property and so contains all chemical aspects (i.e. crosslinker density, acrylic acid content), and is set to $\sim$ 70kPa (68; 168). An immediate corollary to this equation is that Π_{charge} needs to be of the order 70 kPa to have a noticeable impact on microgel swelling. In the absence of electrostatic contributions, i.e. $\Pi_{\mathrm{charge}} = 0$, the steric and elastic forces will counterbalance each other so that $\phi = \phi_{\mathrm{ref}}$, i.e. we obtain the size of the microgel in charge neutral state.

In order to investigate how electrostatic contributions affect the swelling and structure of the microgel, we therefore start by considering light scattering data of microgels suspended in 0.1 M KCl, which screens all charges.

The experimental form factor for the neutral microgels is shown in Figure 3.12a as red symbols, with the corresponding fit from Mie analysis as the solid line. From the experimental fit, a radial density profile can be derived (Figure 3.12b, red curve). The radial density profile is converted into a radial mass distribution, which describes more intuitively how the mass is located within the network (Figure 3.12c, red solid line). Using the described Flory-Rehner theory we can compare the experimental mass distribution to its theoretical counterpart (Figure 3.12c, red dashed line).

We note that a persistent low density core is apparent for all samples (cf. the black dashed line in Figure 3.12c corresponding to homogeneous mass distribution). This is in sharp contrast with the previously established internal composition of neutral microgels: the classic fuzzy sphere model describes a dense core surrounded by a loose

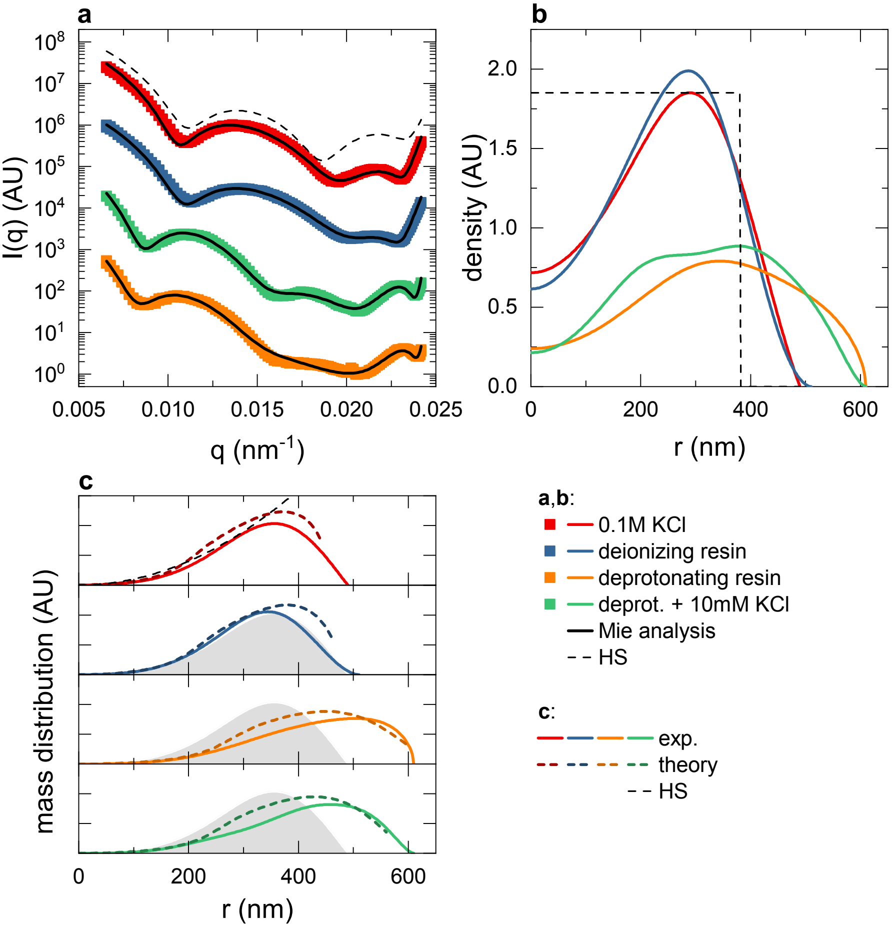

Figure 3.12: **Experimental and theoretical internal structure for loosely crosslinked microgels.** The colour legend indicates charge regime and applies to all panels. **a:** Experimental form factors (symbols) obtained from static light scattering. Solid lines are the best fits from the Mie scattering analysis. The dashed black line represents the pattern caused by hard sphere Mie scattering and is shown for comparison. **b:** Radial density profiles derived from the Mie scattering analysis (solid lines). The dashed black is again a hard sphere reference case. **c:** Corresponding mass distribution profiles for each regime (solid lines), with the 0.1M KCl mass distribution (i.e. solid red curve) shown as a light grey area in the remaining panels. Also shown is the mass distribution inferred from the theoretical model (short dashed lines). The 0.1M KCl panel includes the hard sphere reference case (black dashed line).

corona (63). Scattering data from several different syntheses were created to confirm the inverted profile. The hollow structure is linked to the role of the initiator during the synthesis (169), and indeed the size of the cavity increased with elevated initiator concentration. For this reason, an additional (constant) swelling pressure is included in the model.

We can now turn towards charging of the network. In a first attempt, microgels were suspended in the presence of deionising resins; these resins convert any and all ion species to H^+ and OH^- (which recombines to form water) so that salt content becomes minimal. We thus introduce the electrostatic term to the network pressure $\Pi_{\text{charge}}(q, 0) = qk_B T$ where q is the net electrostatic charge of the microgel network, determined by the amount of deprotonated acid groups.

The experimental form factor is colour coded in blue in Figure 3.12. When considering the radial density profile and mass distribution, only subtle differences can be found compared to the charge neutral microgel composition. The weak charging of the network does not significantly impact the internal structure, except for a minor shift of mass towards the outer edge of the microgel. However, the increase in hydrodynamic radius R_H in Figure 3.13 is unmistakable, and suggests an unfolding of dangling ends in response to the created charges within the network. In contrast, R_H and $R_{\text{form factor}}$ more or less overlap for the neutral microgel, suggesting only a modest contribution of dangling ends to the outer periphery of the microgel. Such a trend has been observed before, but not been noted so explicitly (96).

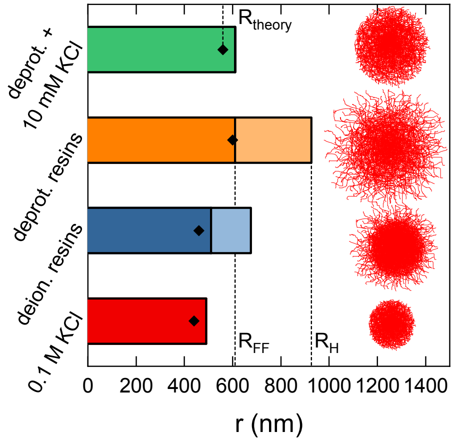

Figure 3.13: Size estimates for various charging regimes. Each charging regime is indicated with a label as well as colour. The core size from SLS is shown as darker shaded area. The additional hydrodynamic length from dangling ends is shown as a lighter shaded area. An impression of the microgel swelling is shown also for each case. R_{theory} is represented by the diamonds.

Deionising conditions do not correspond to fully charged microgels, as only a small fraction of the acid groups will dissociate. With H^+ the only mobile counterion, the charge density in the microgel equals the H^+ concentration, which is governed by the equilibrium constant of acrylic acid (pKa $\sim$ 4.5). We therefore take it one step further, and suspend the previously deionised microgels in the presence of deprotonating resins, which convert all cations to Na^+ and all anions to OH^- (as before). Because the sample was equilibrated under deionising conditions, in effect all H^+ is converted to Na^+. As a consequence, once an acrylic group is deprotonated, the charge will remain more or less bare, because Na^+ cannot form hydrogen bonds. The shifted equilibrium will lead to an increased contribution from the electrostatic swelling term in Eq. 3.3, suggesting a strong network swelling.

The resultant microgel structure is colour coded with yellow in Figure 3.12. The experimental form factor shows a large peak shift to lower q (indicating a larger size), and almost no scattering features can be resolved, suggesting that the microgels barely scatter. Indeed, macroscopically the sample was almost transparent. It is no surprise that the radial density profile and mass distribution display an extremely stretched out network. The strong charging of the network increases the core size of the microgel, and extends dangling ends slightly further (Figure 3.13).

So far, we have thus shown the effect of salinity: a low ionic content will lead to unfolding of the dangling ends but does not result in sufficient charge on the core network to generate swelling. Subsequent deprotonation causes a strong swelling of the core network as the pH increases. The question arises whether the effect of these two external parameters (salinity and pH) can be fully decoupled. Indeed, when adding a small amount of salt (10 mM KCl) to the deprotonated sample, the core swelling remains intact while dangling ends collapse (Figures 3.12 and 3.13, green data).

In summary, our scattering results thus show a decoupling between dangling end response and core response to various charging regimes. The corona conformation is highly sensitive to ambient ionic conditions, and they will unfold readily as evidenced by the changes in hydrodynamic radius. In contrast, the bulk of the network resists charge-induced swelling under deionised conditions, suggesting that dangling ends will dominate the interactions and phase behaviour in this regime. At high pH, the core network swells notably while dangling ends can be collapsed at will by adjusting the ionic strength of the suspension.

These trends also indicate that in order to fully characterise the network swelling of a microgel, both hydrodynamic and static (light) scattering analysis is required: a simple tracking of hydrodynamic radius under changing temperature, pH and salinity does not necessarily reflect changes in the majority of the microgel network. Analogously, studies that solely rely on static light scattering measurements to scrutinize ionic micogels may have overlooked the response of dangling ends.

Finally, our study showcases that even though fine-tuning of 'the perfect' microgels via synthesis is a notoriously difficult task, an easier alternative can be to fine-tune synthesised particles using different salt/ionic resins ingredients. Combined with predictions from classic polymer theory, this allows for studies on microgels with extremely tightly controlled swelling and interactions.

3.2.2 Effect of softness on the phase behaviour of ionic microgels

Equipped with information on the internal structure of the ionic microgels, we can now focus on mapping the phase diagram of ionic microgels. The variable and sensitive size of the ionic microgel network - as illustrated above - can be a detrimental factor for determining the volume fraction of any given sample and is a classic problem in ionic microgel research. In Paper V, we tackle this issue by retrieving the interaction radius R_{eff} from fits to a dedicated theoretical model, so that we can construct a more realistic phase diagram. In addition, we comment on the validity of the model. Because relatively robust results are found, the analysis allows us to draw conclusions on the effect of softness on the effective charge and phase behaviour of ionic microgels.

In order to do so, four sets of PNIPAM-co-AAc microgels were synthesised with cross-linker density 1.5, 3, 5 and 10 mol%. A large concentration range of samples (spanning the entire phase diagram) was created under de-ionised conditions and characterised at 20 °C using confocal microscopy. In addition, dilute samples were measured with dynamic light scattering in order obtain more information on the size of the microgels.

Keeping in mind that for neutral microgels, we have shown that the hydrodynamic radius R_H - which encompasses dangling ends - works well as interaction radius R_{eff}, we

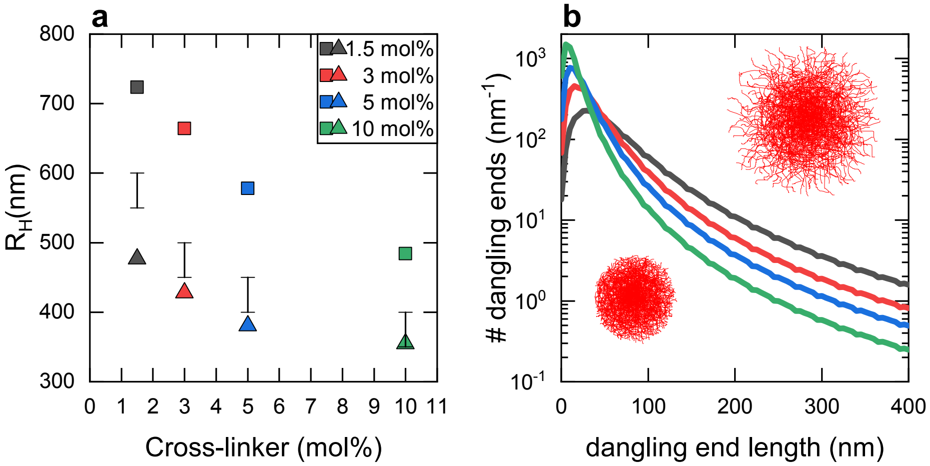

Figure 3.14: **Size estimates for ionic microgels with varying crosslinker density.** Colour legend applies to both panels. **a:** Dynamic light scattering measurements under deionised conditions (upper limit for size R_H, squares) and at pH = 3 (lower limit for size R_{lower}, triangles). The indicated margin represents the range of best-fitting R_{eff} from the fit analysis. **b:** Calculated number and length of dangling ends decorating the microgel surface as function of crosslinker density.

now ask the question how this framework carries over to ionic microgel systems. Under the deionised conditions used in this study, we know that the microgel possesses a porcupine configuration (see also Paper IV). But does this conformation correspond to the interaction radius? DLS measurements were made of dilute samples under deionised conditions (so that dangling ends are extended) to obtain an upper boundary R_H. Samples were also measured at elevated pH, which fully collapses the dangling ends, to generate the lower boundary R_lower. It follows that the interaction radius R_eff should fall within this range. The results in Figure 3.14a show that loosely crosslinked microgels possess the largest core size as well as longest dangling ends, while the 10 mol% crosslinked microgels display the shortest dangling ends. We corroborate this with calculations based on the approach describes in Ref. (68), which predict long dangling ends for loosely crosslinked microgels (Figure 3.14b).

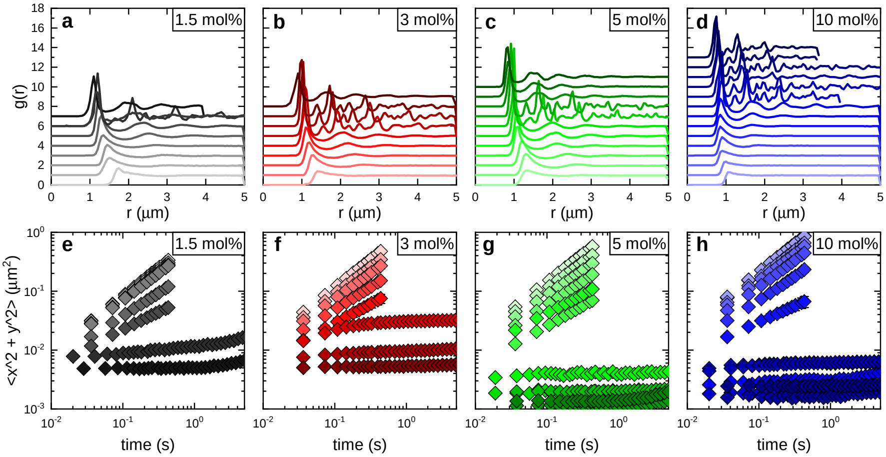

Figure 3.15: Equilibrium and transport properties of ionic microgels. **a-d:** Pair correlation functions for the full concentration range characterised for each type of microgel as indicated in the figure. **e-h:** Corresponding MSDs, which show the transition from liquid to arrested state.

Via confocal microscopy and subsequent quantitative image analysis, structural ($g(r)$) and dynamical (MSD) information across the phase diagram could be derived, with the results shown in Figure 3.15. Based on this data, a phase diagram can be constructed using weight percentage (wt%) as state variable (Figure 3.16a). It becomes apparent that with increasing softness, the crystal phase is suppressed in favour of a glass phase, and crystals were only accessible for 1.5 mol% crosslinked microgels through temperature annealing. However, the phase diagram as it stands is not particularly useful, as the differing sizes of the four microgel sets are not considered. Instead, the effective volume fraction $\phi_\mathrm{eff} = \frac{4}{3}\pi\rho R_\mathrm{eff}^3$ (with ρ the number density) should be used as state variable, so that we loop back to the previous discussion: how is the interaction radius

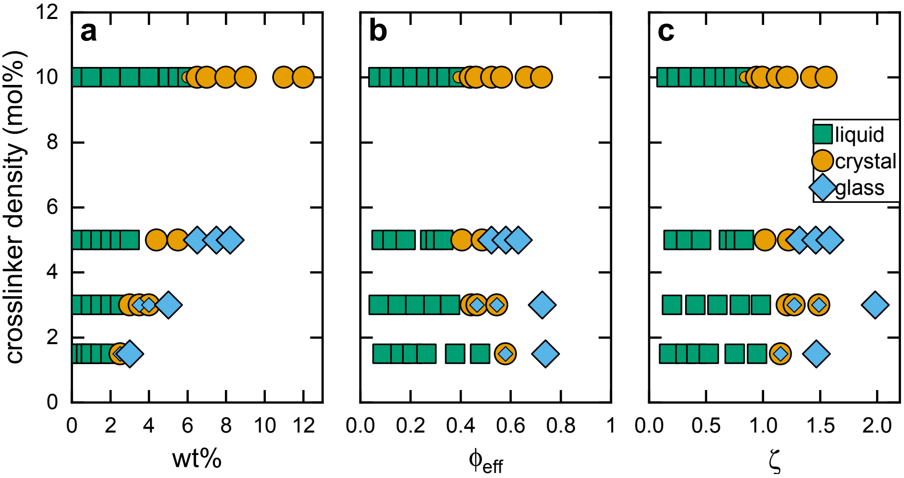

Figure 3.16: Phase diagrams constructed for ionic microgels based on different state variables. Green squares, yellow cirlces and blue diamonds indicate a liquid, crystal and glass phase, respectively. The state variables wt%, effective volume fraction ϕ_{eff} and generalised packing fraction ζ are shown in respective panels **a**, **b** and **c**.

R_{eff} defined for ionic microgels?

Often, as a stop-gap solution, the generalised packing fraction $\zeta = \frac{4}{3}\pi\rho R_{\text{H}}^3$ is employed, but this does not necessarily take into consideration the differences in dangling end length as observed in Figure 3.14. In order to answer this question, we test a dedicated model on all liquid data, using individual fits based on 4-5 radii to span the range between R_{lower} and R_{H}. The model is a superposition of an elastic Hertzian contribution, to mimic network deformation upon particle contact and an electrostatic Yukawa contribution, which represents the charged moieties within the microgel (105). In essence, the interaction potential is thus built up as schematically shown in Figure 1.5a. In addition, the microgel is modeled as a large macro-ion with homogeneous charge to allow free diffusion of the ionic counter species. Although successful before on one or two state points, the model has yet to be thoroughly tested (42; 105).

For each state point, the salt concentration is set to 2.54e-6 M, corresponding with literature values for de-ionised conditions (108) (although we note that the actual confocal samples do not contain any de-ionising resins to avoid salt gradients). In addition, each type of microgel has been assigned a Hertzian interaction strength corresponding to either experimental or literature values. Because the long tail from the Yukawa interaction prevails in the liquid state (there is simply very little particle contact), an estimate for the Hertzian strength suffices.

The only free fit parameters left are then the effective charge Z_{eff}, the effective radius R_{eff} and effective volume fraction ϕ_{eff} (or number density). As mentioned before, each state point is fitted with 4-5 different values for R_{eff}. The numerical $g(r)$ can be shifted by adjusting ϕ_{eff}, while Z_{eff} is employed to match the height of the second order maximum.

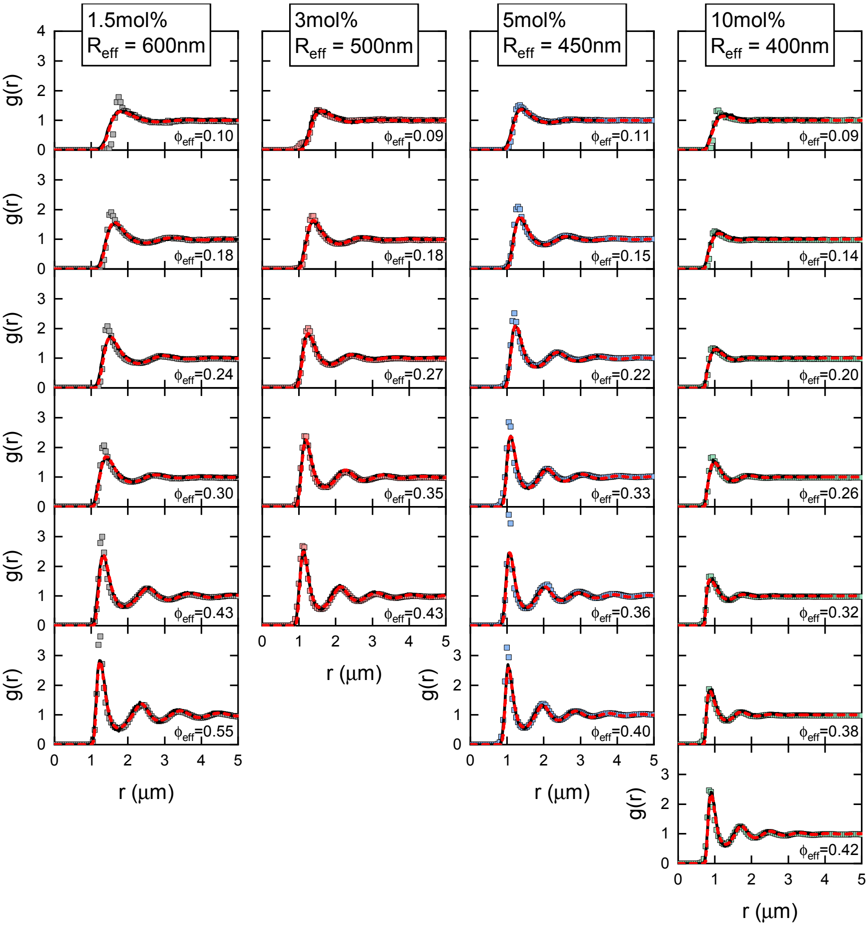

Figure 3.17: **Best fits obtained for each crosslinker series.** From left to right, the crosslinker content increases. From top to bottom, the concentration increases (note that each panel displays a different wt%). R_{eff} values used were 600, 500, 450 and 400nm for 1.5, 3, 5, 10 mol% respectively. Experimental data is represented with squares. The solid black line corresponds to the $g(r)$s derived from the simulated system while the dashed red line reflects the calculated $g(r)$.

The results are encouraging: although a persistent underestimation of the first peak height is found for nearly all considered state points, the model produces reasonable agreement between experimental and simulated $g(r)$ (Figure 3.17). This mismatch is most flagrant for the softest microgel, and cannot be resolved by increasing the effective charge, suggesting that a short-range component due to long dangling ends is missing from the model. Nevertheless, fit parameters are robust over the range of radii canvassed: the effective charge does not vary much between sizes probed and in all cases, the calculated number density collapses onto a master curve (Figure 3.18). Evidently, the model is extremely sensitive to number density.

Unfortunately, the model is less discerning when it comes to radii, with a small range of contenders producing equally good fits. Fits based on the lower boundary R_{lower} and upper boundary R_{H} lead to under- and overestimation of the higher order maxima and minima, respectively. We therefore discard these candidates (and any others causing a similar effect). Only the R_{eff} range shown in Figure 3.14 remains (their values are noted in Figures 3.17 and 3.18). Typical fits are shown in Figure 3.17 for each crosslinker series.

The fitting results also disclose some information on the effect of softness on effective charge. For each microgel type, the trend of Z_{eff} is non-monotonic with increasing concentration, which has been observed before for charged colloids (170). In addition,

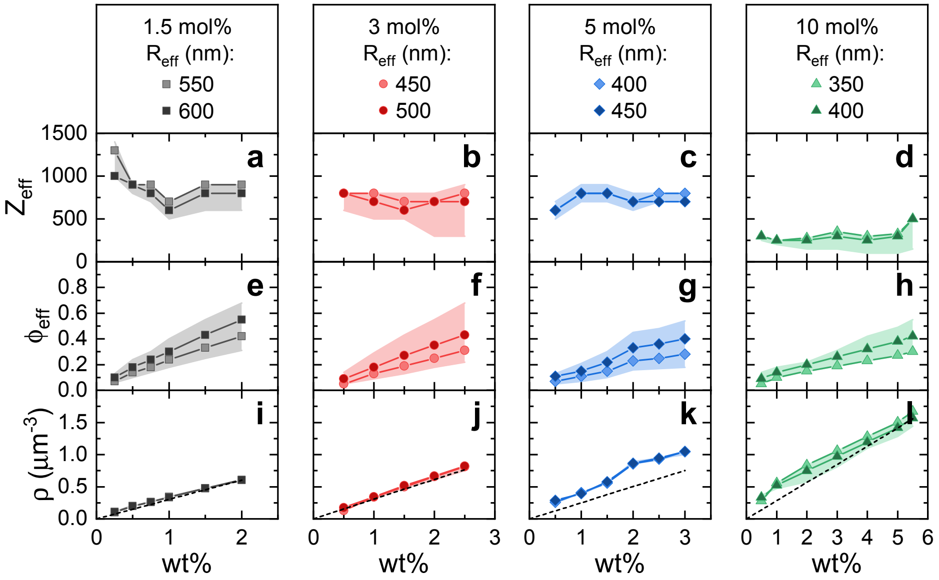

Figure 3.18: Fit parameters obtained for (nearly all) considered radii. Crosslinker content is indicated from left to right. Shaded areas corresponds to values obtained for discarded radii to highlight the robust results. The connected symbols display the results for the best-fitting R_{eff} as denoted in the legends. Panels **a-d**, **e-h**, **i-l** show effective charge Z_{eff}, effective volume fraction ϕ_{eff} and number density ρ, respectively.

Z_{eff} is around ~ 800 for 1.5 mol% crosslinked microgels and around ~ 250 for 10 mol% crosslinked microgels, which appears counter-intuitive at first: small particles loaded with the same amount of acrylic acid should possess a higher charge density compared to large particles. However, this effect has been observed before when comparing swollen and collapsed ionic microgels (171) and is related to charge regulation mechanisms. Acrylic acid is a weak acid, so that a continuous (de)protonation equilibrium will determine particle charge. Because the charges are distributed throughout a smaller microgel volume in the case of the stiff microgels, the equilibrium will shift towards a decreased deprotonation, and so a smaller total charge.

With this information in hand, we reconstruct the phase diagram using ϕ_{eff} as state variable (Figure 3.16b). Because a range of suitable R_{eff} was found, the average value was used to compute ϕ_{eff}. For comparison's sake, the phase diagram has also been plotted as function of ζ which is based on R_{H} (Figure 3.16c).

Not surprisingly, the entire phase diagram has shifted compared to our original construction (Figure 3.16a). We stress also the large difference in x-axis values for Figures 3.16b-c, which exemplifies the difficulties in creating a reliable phase diagram for systems with a diffuse size. Notable is also the slight relative shift for soft microgels in these two phase diagrams, which show how using ζ will skew the phase diagram a soft microgels more strongly than for stiff microgels.

We thus take a closer look at Figure 3.16b, which displays the most reliable phase diagram. The freezing line is more or less stable for stiffer microgels, but with sufficient softness, the onset of crystallisation is delayed. In addition, glass formation is more readily attained for soft microgels whereas the 10 mol% crosslinked microgel does not even display any glassy phase. Evidently, the high network flexibility of soft microgels leads to a delayed arrest, where they get easily trapped in a glassy phase rather than crystallise.

This effect is underlined when considering the dynamics of the system. In Figure 3.19, the normalised diffusion coefficients are shown for each crosslinker. It is immediately evident that dynamics differ strongly between the crosslinker series. The stiffest microgels (green data) display a sharp transition between liquid and arrested state, characteristic of repulsive colloids. On the other hand, the soft microgels display a gradual transition, suggesting that polymeric entanglements are causing the kinetic arrest, rather than any electrostatic or steric repulsion.

Our results thus indicate that while soft microgels possess the flexibility and charge to reach the predicted exotic crystal phase predicted by theory, their softness also leads to long dangling ends which frustrate crystallisation and instead push the system towards a glassy phase. On the other hand, densely crosslinked microgels possess shorter dangling ends so that they crystallise easily, but as a corollary, the contribution from steric repulsion to the overall potential is too big to result in interesting crystalline order.

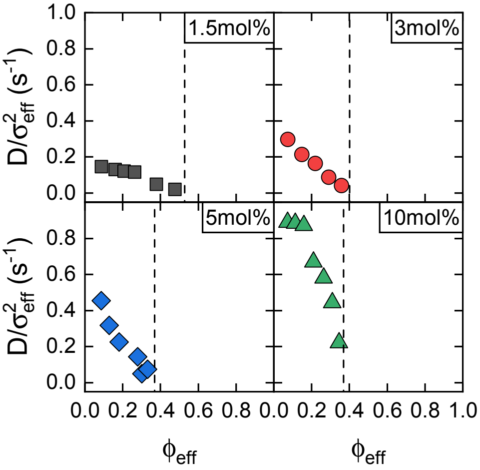

Figure 3.19: **Normalised diffusion coefficient D/σ_{eff} for each state point investigated.** Each panel indicates a different crosslinker series. Dashed lines indicate the arrest transition.

3.2.3 Key conclusions

- The internal structure of ionic microgels is not necessarily described by the fuzzy sphere model, due to neglected initiator effects.
- The swelling response of ionic microgels to internal charges can be decoupled for its structural components: salinity does not impact the core and corona network but has a strong effect on dangling end conformation, which possess a smaller charge density. pH, on the other hand, drives the core and corona swelling. Evidently it is imperative to characterise the swelling response of ionic microgels through a combination of DLS and SLS (or DLS combined with small angle neutron or x-ray scattering in the case of small microgels), to capture both contributions from core/corona and from dangling ends to the resultant size.
- The hydrodynamic radius R_H, often adopted to calculate the generalised packing fraction ζ, is not a good indicator of effective size for ionic microgels due

to their sensitive dangling ends.

- The proposed theoretical model is missing a component due to dangling ends, which are longer for soft microgels. Dangling end interactions are likely to prevent the formation of exotic crystal phases.
- In the ionic microgel phase diagram, increased softness pushes the freezing line to higher volume fractions, and the crystal region narrows. The much longer and strongly extended dangling ends of these microgels drive the sample into kinetic arrest and thus hinder nucleation and growth of crystals.

3.3 Proteins

3.3.1 The existence of a cluster glass transition in dense lysozyme solutions

The actual existence of a glass transition in cluster-forming protein solutions is disputed (115; 141). Because of experimental difficulties in obtaining the relevant volume fractions, only two experimental studies have reported on the zero shear viscosity of dense lysozyme samples, with opposing conclusions. For this reason, in Paper VI we map the liquid-solid arrest using two passive microrheology techniques, in combination with a new method for concentrating lysozyme samples.

Commercial lysozyme contains a large amount of ionic impurities, which can significantly alter the resultant interaction potential. For this reason, the protein was washed in ultra-centrifugation tubes with HEPES buffer until the conductivity reaches a plateau value. The same ultra-centrifugation tubes were used to concentrate small amounts of lysozyme solution to $\phi = 0.35 \pm 0.03$, which is already a leap forwards compared to previous research, where large sample requirements halted sample densification beyond $\phi = 0.25$. The extremely viscous sample was then mixed with a few microlitre of tracer particle suspension, which imparts a finite dilution upon the sample. The tracer particles were surface modified as described in earlier work (172), to reduce interactions. The final samples were portioned into samples for DLS-based microrheology ($\sim 100\mu$l) and MPT-based microrheology ($\sim 5\mu$l), which are described in more detail in the Materials and Methods (Section 2.4).

From both techniques, the tracer particle MSDs were obtained (Figure 3.20a), which show first of all excellent overlap between the two approaches. Secondly, all MSDs are linear in the observed time frame, which indicates that the tracers are in a purely diffusive regime and that the long-time diffusion of the tracers is captured. The long-time diffusion is necessary in order to calculate the relative zero shear viscosity η_r of the lysozyme samples, as detailed in Section 2.4 and Paper VI. In Figure 3.20b, Van Hove functions are plotted for samples with increasing lysozyme volume fraction. The probability density function narrows to zero, indicating the slowing down of the tracer particles (which is reflected in the decreasing motion of the MSDs in Figure 3.20a). The shape of each function is captured well with a Gaussian fit, which signals that the tracer particles explore a homogeneous sample environment.

Next, η_r was calculated via the Stokes-Einstein equation based on the tracer diffusion coefficient from both techniques (Figure 3.20c). The resultant viscosity behaviour was fitted with the Quemada model for repulsive colloids (173):

$$\eta_{\mathrm{r}} = \left(1 - \frac{\phi}{\phi_{\mathrm{max}}}\right)^{-2} \tag{3.4}$$

with ϕ the volume fraction of the protein, leading to a predicted $\phi_{\mathrm{max}} = 0.34$. The excellent agreement with the Quemada model signifies that the repulsion between clusters controls the macroscopic viscosity of the protein samples.

Because the addition of tracer particles will always impart a finite dilution upon the sample, another road to fully arrested samples had to be taken. We deposited a droplet of moderately concentrated sample (containing lysozyme and tracer particles) on a confocal microscopy sample cell, and allowed solvent to evaporate (see also Material and Methods). Although the sample volume is small ($< 5\mu$l), it can still be characterised with MPT-based microrheology. In this manner we created lysozyme concentrations far beyond the glass transition, and the solidification of the droplet - i.e. a macroscopic arrest - was readily observed (Figure 3.20d). The sample becomes heterogeneous, due to the drying front at the air-sample interface, but all motion from tracer particles dropped below the detection limit between $\phi = 0.34 - 0.37$, confirming the prediction from the viscosity fit.

Our study is thus a clear demonstration of the efficacy of our relatively simple evaporation-mediated sample densification in combination with microrheology. Yet, we also caution on the dangers of evaporation when using microlitre-based techniques in combination with concentrated samples. Evaporation occurs fast enough to induce significant concentration changes - and so the associated viscosity - on the timescales involved in sample handling.

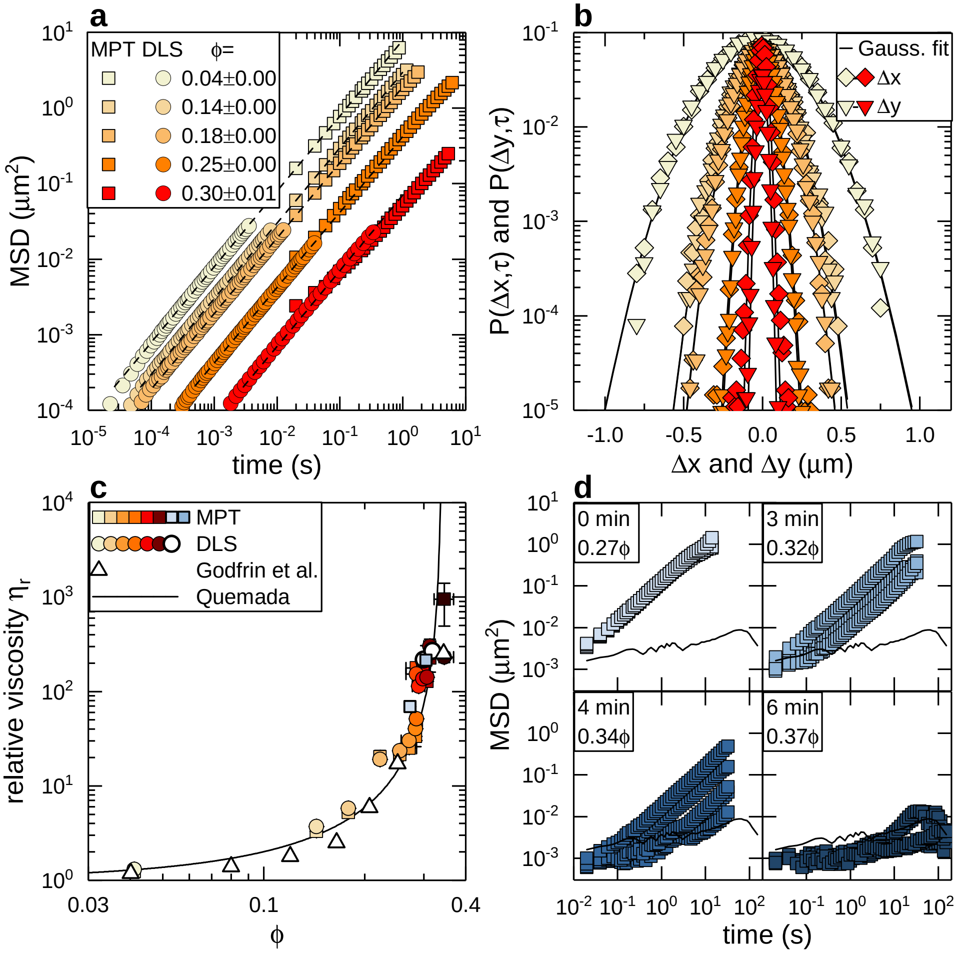

Figure 3.20: Tracer particle motion in lysozyme samples **a:** Tracer particle MSDs obtained via DLS-based microrheology (circles) and MPT-based microrheology (squares), where samples are colour coded according to lysozyme volume fraction. **b:** Corresponding Van Hove functions connected to the MSDs from MPT-based microrheology. **c:** Viscosity behaviour of lysozyme over a large concentration range. The solid line is a fit to the data with the Quemada model, which is used for repulsive colloids. **d:** The arrest transition of lysozyme captured experimentally: with increased evaporation time (from 0 to 6 min) the motion of the tracer particles comes to a full stop.

3.3.2 Patchy attractions dominate the macroscopic phase behaviour of γ_B-crystallin

The arrest transition for the eye lens protein γ_B-crystallin has been ill-researched, because sample is difficult to obtain and densify. Previous research indicates that γ_B-crystallin phase behaviour is driven by short ranged anisotropic attractions due to hydrophobic patches (117; 145). Attractions are often temperature dependent, yet the arrest line of γ_B-crystallin was suggested to be temperature independent.

Although the underlying interaction potential differs strongly from the previously studied lysozyme system, investigations into the arrest line of γ_B-crystallin are once again propelled by the latest advances in microlitre research. We take advantage of the minute sample requirements, and apply the same machinery as discussed earlier: the sample viscosity is measured indirectly via two passive microrheology techniques, and extremely concentrated samples were made via controlled evaporation.

Indeed, the resultant relation between volume fraction and viscosity behaves markedly different from lysozyme. A good fit with typical (repulsive) hard sphere models was impossible. Instead, a powerlaw dependence was found, in congruence with the predicted viscosity behaviour for attractive colloids (Figure 3.21a) according to:

$$\eta_r \propto |\phi - \phi_{\max}|^{-\nu} \tag{3.5}$$

where the exponent ν takes the value of 3.23 (174). These results suggest that the attractions between γ_B-crystallins drive the macroscopic viscosity. A more or less constant $\phi_{\max} = 0.3$ is found (Figure 3.21b), in contrast to the arrest line varying between $\phi_{\max} \sim 0.5 - 0.6$ for isotropically attractive colloids experiencing a comparable attraction strength (depending on the attractive model and attraction strength used) (174; 175). The early onset arrest is thus likely caused by the directional patchy attractions between γ_B-crystallin, which has been shown to lead to the formation of large transient clusters (117).

We also direct the reader's attention to the deviating DLS results in Figure 3.21a. Some measurements were performed close to the critical temperature ($T_c = 19°\text{C}$) and across the critical concentration ($\phi_{\text{crit}} = 0.154$), where the scattering contribution of the proteins to the total scattering becomes significant and obstructs a clean separation between the tracer decay and protein decay, necessary for adequate analysis. These kind of considerations are not relevant in MPT-based microrheology, which relies solely on the fluorescence signal of the tracer particles.

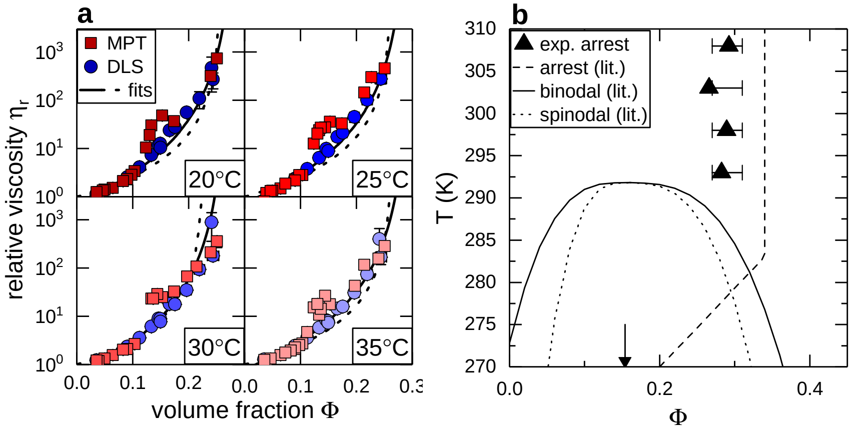

Figure 3.21: Viscosity and macroscopic phase behaviour for γ_B-crystallin. **a:** Viscosity curves obtained 20, 25, 30, 35 °C. Blue circles correspond to MPT results while red squares denote DLS results (the legend is incorrect). The unsuccessful Quemada fit is shown as dashed line, while the successful powerlaw fit is depicted with a solid line. **b:** Phase diagram for γ_B-crystallin adapted from (145) with the experimentally determined arrest transition included. The arrow indicates the critical concentration $\phi_{\text{crit}} = 0.154$.

3.3.3 Key conclusions

- DLS and MPT-based microrheology are powerful, complementary techniques which facilitate investigations into the rheological properties of precious material.
- Densification of microlitre samples via controlled evaporation is a straightforward, but powerful tool to create samples otherwise difficult to access experimentally. It also signals that when handling samples of minute volume, evaporation can already significantly alter the sample concentration.
- Using a combination of microrheology and evaporation-mediated sample preparation, we unambiguously demonstrated the cluster-driven glass arrest of lysozyme at low ionic strength.
- Within the same approach, the macroscopic arrest of γ_B-crystallin is driven by its attractive patches, which leads to early onset of the arrest and a concentration dependence of the viscosity that is described by a powerlaw.

4 Conclusions and outlook

The connection between macroscopic phase behaviour and microscopic particle interactions has been a frequently studied topic in soft matter research. The work described in this thesis has aimed to contribute to this research area, focusing on liquid-solid transition. Using confocal laser scanning microscopy, we characterised key structural and dynamic properties of neutral microgels, ionic microgels and proteins interacting via a complex potential.

A close inspection of neutral microgel phase behaviour has led us to develop a model based on elastic contributions, taking into consideration the considerable core repulsion at higher packing fraction. Surprisingly, although the core repulsion was imperative once a depletion attraction was introduced, in dense systems its effect could not be pinpointed. Evidently, further research is necessary to test how the inhomogeneous polymer distribution within the microgel as well as its flexible size will affect interactions at even higher concentration. Another key question is how the interaction potential evolves as the VPTT is transgressed: the microgel interactions will change from soft repulsive to attractive, but the precise evolution is, as of yet, unclear.

Whilst exploring the dense region of the neutral microgel phase diagram, we identified a peculiar heterogeneous state which is a result from sample preparation at room temperature: at 20°C, microgels were swollen and strongly interpenetrated, but once the temperature was elevated to 30°C, these polymer entanglements prevented network shrinkage, instead exerting large strain on the particles. Such a state will possess interesting rheological properties, which will depend strongly on the 'history' of the sample.

The investigation into the internal morphology of ionic microgels has been elucidating in many ways. We found that the loose polymer strands decorating the surface of the microgel are very sensitive to the salinity in the ambient environment, and can increase the hydrodynamic size of the microgels with several hundred nm even though the crosslinked network itself does not change. On the other hand, the swelling (and consequently, the size) of the crosslinked network can be altered via addition of deionising or deprotonating resins, so that the appearance and charge of the ionic microgel can be fully controlled using external parameters.

The dangling ends of ionic microgels are key players also in their interactions: testing of the proposed interaction model suggested that an additional short-range component due to dangling end interactions is currently lacking. Regardless, our in-depth analysis of the structural data resulted in an interaction radius which was used to calculate the 'true' volume fraction of the ionic microgel suspensions. We have thus presented the first realistic phase diagram for ionic microgels, which shows a narrowing crystal region with increasing softness.

These results allow us to suggest an answer to the long standing question of the 'missing' exotic crystal phases predicted from this theoretical model. Loosely crosslinked microgels were shown to posses a high effective charge, which is instrumental in obtaining the predicted exotic crystalline phases. However, these particles get kinetically trapped before any crystal state can be reached due to their long dangling ends. In contrast, stiff microgels possess short dangling ends, but their steric repulsion is too high to drive the system towards interesting crystal phases.

We also note that the generalised packing fraction, based on the hydrodynamic radius, is sometimes used to describe the phases of ionic microgels. Yet, our analysis reveals that such an approach has inherent issues: compared to stiff microgels, the hydrodynamic size of soft microgels is relatively larger than its interaction radius. Phase diagrams based on the generalised packing fraction will therefore always deviate more strongly for soft microgels.

Finally, we investigated the liquid-solid arrest for two proteins interacting via complex interaction potentials. Lysozyme is known to form equilibrium clusters caused by its short range attractions and long range repulsion, but the existing studies on its glass transition wae contradictory. We showcased a new evaporation-mediated technique, which allowed us to create liquid and solid lysozyme samples traversing the arrest. We can thus unambiguously confirm the existence of the cluster glass. The simple evaporation process is successful because we use it in combination with microrheology, for which minute amounts of sample are required. The combination of these approaches is a template, which can be easily applied for any investigation into dense dynamics of precious proteins. We thus open up new avenues into the arrest of biological proteins, which were previously experimentally inaccessible.

One of those proteins is γ_B-crystallin, an eye lens protein which is known to interact via an attractive interaction potential. Via the same approach as used for the lysozyme study, we found that γ_B-crystallin undergoes an arrest transition at quite low volume fraction, which is mediated by its attractive patches. These patches have been shown before to cause large transient cluster formation. The dependence of macroscopic viscosity on protein concentration differs from the corresponding behaviour found for lysozyme, and instead reflects a power law dependence predicted for attractive colloids.

5 | References

[1] Trinkle, D. R. & Woodward, C. The chemistry of deformation: How solutes soften pure metals. *Science* **310**, 1665–1667 (2005).

[2] Poon, W. Colloids as big atoms. *Science* **304**, 830–831 (2004).

[3] Pusey, P. & Van Megen, W. Phase behaviour of concentrated suspensions of nearly hard colloidal spheres. *Nature* **320**, 340–342 (1986).

[4] Pusey, P. N. & van Megen, W. Observation of a glass transition in suspensions of spherical colloidal particles. *Phys. Rev. Let.* **59**, 2083 (1987).

[5] Hoover, W. G. & Ree, F. H. Use of computer experiments to locate the melting transition and calculate the entropy in the solid phase. *J. Chem. Phys.* **47**, 4873–4878 (1967).

[6] Hoover, W. G. & Ree, F. H. Melting transition and communal entropy for hard spheres. *J. Chem. Phys.* **49**, 3609–3617 (1968).

[7] Sciortino, F. & Tartaglia, P. Glassy colloidal systems. *Adv. Phys.* **54**, 471–524 (2005).

[8] Cipelletti, L. & Ramos, L. Slow dynamics in glassy soft matter. *J. Phys-Condens. Mat.* **17**, R253 (2005).

[9] Hunter, G. L. & Weeks, E. R. The physics of the colloidal glass transition. *Rep. Prog. Phys.* **75**, 066501 (2012).

[10] Yunker, P. J. *et al.* Physics in ordered and disordered colloidal matter composed of poly (n-isopropylacrylamide) microgel particles. *Rep. Prog. Phys.* 77, 056601 (2014).

[11] Sacanna, S. & Pine, D. J. Shape-anisotropic colloids: Building blocks for complex assemblies. *Curr. Opin. Colloid In.* **16**, 96–105 (2011).

[12] Morphew, D. & Chakrabarti, D. Clusters of anisotropic colloidal particles: from colloidal molecules to supracolloidal structures. *Curr. Opin. Colloid In.* **30**, 70–80 (2017).

[13] Kratz, K., Hellweg, T. & Eimer, W. Structural changes in pnipam microgel particles as seen by sans, dls, and em techniques. *Polymer* **42**, 6631–6639 (2001).

[14] Saunders, B. R. & Vincent, B. Microgel particles as model colloids: theory, properties and applications. *Adv. Colloid Interfac.* **80**, 1–25 (1999).

[15] Wu, J., Zhou, B. & Hu, Z. Phase behavior of thermally responsive microgel colloids. *Phys. Rev. Let.* **90**, 048304 (2003).

[16] Rey, M. *et al.* Isostructural solid–solid phase transition in monolayers of soft core–shell particles at fluid interfaces: structure and mechanics. *Soft Matter* **12**, 3545–3557 (2016).

[17] Lyon, L. A. & Fernandez-Nieves, A. The polymer/colloid duality of microgel suspensions. *Annu. Rev. Phys. Chem.* **63**, 25–43 (2012).

[18] Vlassopoulos, D. & Cloitre, M. Tunable rheology of dense soft deformable colloids. *Curr. Opin. Colloid In.* **19**, 561–574 (2014).

[19] van der Scheer, P., van de Laar, T., van der Gucht, J., Vlassopoulos, D. & Sprakel, J. Fragility and strength in nanoparticle glasses. *ACS Nano* **11**, 6755–6763 (2017).

[20] Senff, H. & Richtering, W. Temperature sensitive microgel suspensions: Colloidal phase behavior and rheology of soft spheres. *J. Chem. Phys.* **111**, 1705–1711 (1999).

[21] Fernández-Nieves, A., Fernández-Barbero, A., Vincent, B. & De Las Nieves, F. Charge controlled swelling of microgel particles. *Macromol.* **33**, 2114–2118 (2000).

[22] Rasmusson, M., Routh, A. & Vincent, B. Flocculation of microgel particles with sodium chloride and sodium polystyrene sulfonate as a function of temperature. *Langmuir* **20**, 3536–3542 (2004).

[23] Wang, Z., Wang, F., Peng, Y., Zheng, Z. & Han, Y. Imaging the homogeneous nucleation during the melting of superheated colloidal crystals. *Science* **338**, 87–90 (2012).

[24] Hilhorst, J. & Petukhov, A. Variable dislocation widths in colloidal crystals of soft thermosensitive spheres. *Phys. Rev. Lett.* **107**, 095501 (2011).

[25] Peng, Y., Wang, Z., Alsayed, A. M., Yodh, A. G. & Han, Y. Melting of colloidal crystal films. *Phys. Rev. Lett.* **104**, 205703 (2010).

[26] Alsayed, A. M., Islam, M. F., Zhang, J., Collings, P. J. & Yodh, A. G. Premelting at defects within bulk colloidal crystals. *Science* **309**, 1207–1210 (2005).

[27] Mohanty, P. S., Bagheri, P., Nöjd, S., Yethiraj, A. & Schurtenberger, P. Multiple path-dependent routes for phase-transition kinetics in thermoresponsive and field-responsive ultrasoft colloids. *Phys. Rev. X* **5**, 011030 (2015).

[28] Purnomo, E. H., van den Ende, D., Vanapalli, S. A. & Mugele, F. Glass transition and aging in dense suspensions of thermosensitive microgel particles. *Phys. Rev. Lett.* **101**, 238301 (2008).

[29] Zhang, Z. *et al.* Thermal vestige of the zero-temperature jamming transition. *Nature* **459**, 230–233 (2009).

[30] Caswell, T. A., Zhang, Z., Gardel, M. L. & Nagel, S. R. Observation and characterization of the vestige of the jamming transition in a thermal three-dimensional system. *Phys. Rev. E* **87**, 012303 (2013).

[31] Rivas-Barbosa, R. *et al.* Different routes into the glass state for soft thermo-sensitive colloids. *Soft Matter* (2018).

[32] Sacanna, S., Irvine, W., Chaikin, P. M. & Pine, D. J. Lock and key colloids. *Nature* **464**, 575–578 (2010).

[33] William, T. *et al.* Lock and key colloids through polymerization-induced buckling of monodisperse silicon oil droplets. *Soft Matter* **7**, 1631–1634 (2011).

[34] Månsson, L. K., Immink, J. N., Mihut, A. M., Schurtenberger, P. & Crassous, J. J. A new route towards colloidal molecules with externally tunable interaction sites. *Faraday Discuss.* **181**, 49–69 (2015).

[35] Paloli, D., Mohanty, P. S., Crassous, J. J., Zaccarelli, E. & Schurtenberger, P. Fluid–solid transitions in soft-repulsive colloids. *Soft Matter* **9**, 3000–3004 (2013).

[36] Mohanty, P. S., Paloli, D., Crassous, J. J., Zaccarelli, E. & Schurtenberger, P. Effective interactions between soft-repulsive colloids: Experiments, theory, and simulations. *J. Chem. Pys* **140**, 094901 (2014).

[37] Iyer, A. S. J. & Lyon, L. A. Self-healing colloidal crystals. *Angew. Chem. Int. Edit.* **48**, 4562–4566 (2009).

[38] Gottwald, D., Likos, C., Kahl, G. & Löwen, H. Phase behavior of ionic microgels. *Phys. Rev. Let.* **92**, 068301 (2004).

[39] Pàmies, J. C., Cacciuto, A. & Frenkel, D. Phase diagram of hertzian spheres. *J. Chem. Phys.* **131**, 044514 (2009).

[40] Mohanty, P. S., Yethiraj, A. & Schurtenberger, P. Deformable particles with anisotropic interactions: unusual field-induced structural transitions in ultrasoft ionic microgel colloids. *Soft Matter* **8**, 10819–10822 (2012).

[41] Nöjd, S., Mohanty, P. S., Bagheri, P., Yethiraj, A. & Schurtenberger, P. Electric field driven self-assembly of ionic microgels. *Soft Matter* **9**, 9199–9207 (2013).

[42] Colla, T. *et al.* Self-assembly of ionic microgels driven by an alternating electric field: Theory, simulations, and experiments. *ACS Nano* **12**, 4321–4337 (2018).

[43] Cloitre, M., Borrega, R., Monti, F. & Leibler, L. Structure and flow of polyelectrolyte microgels: from suspensions to glasses. *C. R. Physique* **4**, 221–230 (2003).

[44] Gasser, U. *et al.* Form factor of pnipam microgels in overpacked states. *J. Chem. Phys.* **141**, 034901 (2014).

[45] Pelaez-Fernandez, M., Souslov, A., Lyon, L., Goldbart, P. M. & Fernandez-Nieves, A. Impact of single-particle compressibility on the fluid-solid phase transition for ionic microgel suspensions. *Phys. Rev. Let.* **114**, 098303 (2015).

[46] Conley, G. M., Aebischer, P., Nöjd, S., Schurtenberger, P. & Scheffold, F. Jamming and overpacking fuzzy microgels: Deformation, interpenetration, and compression. *Sci. Adv.* **3**, e1700969 (2017).

[47] Mohanty, P. S. *et al.* Interpenetration of polymeric microgels at ultrahigh densities. *Sci. Rep.* **7**, 1487 (2017).

[48] Hendrickson, G. R. & Lyon, L. A. Microgel translocation through pores under confinement. *Angew. Chem. Int. Edit.* **49**, 2193–2197 (2010).

[49] Heskins, M. & Guillet, J. E. Solution properties of poly (n-isopropylacrylamide). *J. Macromol. Sci. Chem.* **2**, 1441–1455 (1968).

[50] Halperin, A., Kröger, M. & Winnik, F. M. Poly (n-isopropylacrylamide) phase diagrams: Fifty years of research. *Angew. Chem. Int. Edit.* **54**, 15342–15367 (2015).

[51] Wu, C., Zhou, S., Au-yeung, S. C. & Jiang, S. Volume phase transition of spherical microgel particles. *Angew. Makromol. Chem.* **240**, 123–136 (1996).

[52] Pelton, R. Temperature-sensitive aqueous microgels. *Adv. Colloid Interfac.* **85**, 1–33 (2000).

[53] Lele, A., Hirve, M., Badiger, M. & Mashelkar, R. Predictions of bound water content in poly (n-isopropylacrylamide) gel. *Macromol.* **30**, 157–159 (1997).

[54] Reufer, M., Dıaz-Leyva, P., Lynch, I. & Scheffold, F. Temperature-sensitive poly (n-isopropyl-acrylamide) microgel particles: A light scattering study. *Eur. Phys. J. E* **28**, 165–171 (2009).

[55] Sierra-Martin, B. *et al.* Microscopic signature of a microgel volume phase transition. *Macromol.* **38**, 10782–10787 (2005).

[56] Romeo, G., Fernandez-Nieves, A., Wyss, H. M., Acierno, D. & Weitz, D. A. Temperature-controlled transitions between glass, liquid, and gel states in dense p-nipa suspensions. *Adv. Mat. Res.* **22**, 3441–3445 (2010).

[57] Pelton, R. & Chibante, P. Preparation of aqueous latices with n-isopropylacrylamide. *Colloid. Surface.* **20**, 247–256 (1986).

[58] Peppas, N., Bures, P., Leobandung, W. & Ichikawa, H. Hydrogels in pharmaceutical formulations. *Eur. J. Pharm. Biopharm.* **50**, 27–46 (2000).

[59] de las Heras Alarcón, C., Pennadam, S. & Alexander, C. Stimuli responsive polymers for biomedical applications. *Chem. Soc. Rev.* **34**, 276–285 (2005).

[60] Oh, J. K., Drumright, R., Siegwart, D. J. & Matyjaszewski, K. The development of microgels/nanogels for drug delivery applications. *Prog. Pol. Sci.* **33**, 448–477 (2008).

[61] Hamidi, M., Azadi, A. & Rafiei, P. Hydrogel nanoparticles in drug delivery. *Adv. Drug Deliver. Rev.* **60**, 1638–1649 (2008).

[62] Gan, T., Guan, Y. & Zhang, Y. Thermogelable pnipam microgel dispersion as 3d cell scaffold: effect of syneresis. *J. Mater. Chem.* **20**, 5937–5944 (2010).

[63] Stieger, M., Richtering, W., Pedersen, J. S. & Lindner, P. Small-angle neutron scattering study of structural changes in temperature sensitive microgel colloids. *J. Chem. Phys.* **120**, 6197–6206 (2004).

[64] Wu, X., Pelton, R., Hamielec, A., Woods, D. & McPhee, W. The kinetics of poly (n-isopropylacrylamide) microgel latex formation. *Colloid Polym. Sci.* **272**, 467–477 (1994).

[65] Virtanen, O. & Richtering, W. Kinetics and particle size control in non-stirred precipitation polymerization of n-isopropylacrylamide. *Colloid Polym. Sci.* **292**, 1743–1756 (2014).

[66] Meyer, S. & Richtering, W. Influence of polymerization conditions on the structure of temperature-sensitive poly (n-isopropylacrylamide) microgels. *Macromol.* **38**, 1517–1519 (2005).

[67] Smith, M. H., Herman, E. S. & Lyon, L. A. Network deconstruction reveals network structure in responsive microgels. *J. Phys. Chem. B* **115**, 3761–3764 (2011).

[68] Boon, N. & Schurtenberger, P. Swelling of micro-hydrogels with a crosslinker gradient. *Phys. Chem. Chem. Phys.* **19**, 23740–23746 (2017).

[69] Gnan, N., Rovigatti, L., Bergman, M. & Zaccarelli, E. In silico synthesis of microgel particles. *Macromolecules* **50**, 8777–8786 (2017).

[70] Acciaro, R., Gilanyi, T. & Varga, I. Preparation of monodisperse poly (n-isopropylacrylamide) microgel particles with homogenous cross-link density distribution. *Langmuir* **27**, 7917–7925 (2011).

[71] Still, T., Chen, K., Alsayed, A. M., Aptowicz, K. B. & Yodh, A. Synthesis of micrometer-size poly (n-isopropylacrylamide) microgel particles with homogeneous crosslinker density and diameter control. *J. Colloid Interf. Sci.* **405**, 96–102 (2013).

[72] Tiwari, R. *et al.* A versatile synthesis platform to prepare uniform, highly functional microgels

via click-type functionalization of latex particles. *Macromol,* **47**, 2257–2267 (2014).

[73] Wei, J., Li, Y. & Ngai, T. Tailor-made microgel particles: Synthesis and characterization. *Colloid. Surface A* **489**, 122 – 127 (2016).

[74] Mueller, E. *et al.* Dynamically cross-linked self-assembled thermoresponsive microgels with homogeneous internal structures. *Langmuir* **34**, 1601–1612 (2018).

[75] Varga, I., Gilányi, T., Meszaros, R., Filipcsei, G. & Zrinyi, M. Effect of cross-link density on the internal structure of poly (n-isopropylacrylamide) microgels. *J. Phys. Chem. B* **105**, 9071–9076 (2001).

[76] Wu, J., Huang, G. & Hu, Z. Interparticle potential and the phase behavior of temperature-sensitive microgel dispersions. *Macromol.* **36**, 440–448 (2003).

[77] Stieger, M., Pedersen, J. S., Lindner, P. & Richtering, W. Are thermoresponsive microgels model systems for concentrated colloidal suspensions? a rheology and small-angle neutron scattering study. *Langmuir* **20**, 7283–7292 (2004).

[78] Heyes, D. & Brańka, A. Interactions between microgel particles. *Soft Matter* **5**, 2681–2685 (2009).

[79] Zaccone, A., Crassous, J. J. & Ballauff, M. Colloidal gelation with variable attraction energy. *J. Chem. Phys.* **138**, 104908 (2013).

[80] Zaccone, A., Crassous, J. J., Béri, B. & Ballauff, M. Quantifying the reversible association of thermosensitive nanoparticles. *Phys. Rev. Let.* **107**, 168303 (2011).

[81] Scheffold, F. *et al.* Brushlike interactions between thermoresponsive microgel particles. *Phys. Rev. Let.* **104**, 128304 (2010).

[82] Romeo, G. & Ciamarra, M. P. Elasticity of compressed microgel suspensions. *Soft Matter* **9**, 5401–5406 (2013).

[83] Zhu, Y.-L. & Lu, Z.-Y. Phase diagram of spherical particles interacted with harmonic repulsions. *J. Chem. Phys* **134**, 044903 (2011).

[84] Landau, L. D. & Lifshitz, E. M. *Quantum Mechanics: Non-relativistic Theory. V. 3 of Course of Theoretical Physics* (Pergamon Press, 1958).

[85] Hoare, T. & Pelton, R. Functional group distributions in carboxylic acid containing poly (n-isopropylacrylamide) microgels. *Langmuir* **20**, 2123–2133 (2004).

[86] Hoare, T. & Pelton, R. Electrophoresis of functionalized microgels: morphological insights. *Polymer* **46**, 1139–1150 (2005).

[87] Hoare, T. & McLean, D. Kinetic prediction of functional group distributions in thermosensitive microgels. *J. Phys. Chem. B* **110**, 20327–20336 (2006).

[88] Hoare, T. & Pelton, R. Titrametric characterization of ph-induced phase transitions in functionalized microgels. *Langmuir* **22**, 7342–7350 (2006).

[89] Hoare, T. & Pelton, R. Functionalized microgel swelling: comparing theory and experiment. *J. Phys. Chem. B* **111**, 11895–11906 (2007).

[90] Lietor-Santos, J., Gasser, U., Vavrin, R., Hu, Z. & Fernandez-Nieves, A. Structural changes of poly (n-isopropylacrylamide)-based microgels induced by hydrostatic pressure and temperature studied by small angle neutron scattering. *J. Chem. Phys.* **133**, 034901 (2010).

[91] Romeo, G., Imperiali, L., Kim, J.-W., Fernández-Nieves, A. & Weitz, D. A. Origin of de-swelling and dynamics of dense ionic microgel suspensions. *J. Chem. Phys.* **136**, 124905 (2012).

[92] Gasser, U. *et al.* Transient formation of bcc crystals in suspensions of poly (n-isopropylacrylamide)-based microgels. *Phys. Rev. E* **88**, 052308 (2013).

[93] Hyatt, J. S. *et al.* Charge segregation in weakly ionized microgels. *Phys. Rev. E* **95**, 012608 (2017).

[94] Kratz, K., Hellweg, T. & Eimer, W. Influence of charge density on the swelling of colloidal poly (n-isopropylacrylamide-co-acrylic acid) microgels. *Colloid. Surface. A* **170**, 137–149 (2000).

[95] Jones, C. D. & Lyon, L. A. Shell-restricted swelling and core compression in poly (n-isopropylacrylamide) core- shell microgels. *Macromol.* **36**, 1988–1993 (2003).

[96] Nöjd, S. *et al.* Deswelling behaviour of ionic microgel particles from low to ultra-high densities. *Soft Matter* **14**, 4150–4159 (2018).

[97] Oliveira, C. L. *et al.* Gaussian deconvolution: a useful method for a form-free modeling of scattering data from mono-and multilayered planar systems. *J. Appl. Crystallogr.* **45**, 1278–1286 (2012).

[98] Oliveira, C. L., Santos, P. R., Monteiro, A. M. & Neto, A. M. F. Effect of oxidation on the structure of human low-and high-density lipoproteins. *Biophys. J.* **106**, 2595–2605 (2014).

[99] Virtanen, O., Mourran, A., Pinard, P. & Richtering, W. Persulfate initiated ultra-low cross-linked poly (n-isopropylacrylamide) microgels possess an unusual inverted cross-linking structure. *Soft Matter* **12**, 3919–3928 (2016).

[100] Poon, W. C., Weeks, E. R. & Royall, C. P. On measuring colloidal volume fractions. *Soft Matter* **8**, 21–30 (2012).

[101] Muluneh, M. & Weitz, D. A. Direct visualization of three-dimensional crystallization behavior in microgels. *Phys. Rev. E* **85**, 021405 (2012).

[102] Sierra-Martin, B. & Fernandez-Nieves, A. Phase and non-equilibrium behaviour of microgel suspensions as a function of particle stiffness. *Soft Matter* **8**, 4141–4150 (2012).

[103] Mohanty, P. & Richtering, W. Structural ordering and phase behavior of charged microgels. *J. Phys. Chem. B* **112**, 14692–14697 (2008).

[104] Gottwald, D., Likos, C. N., Kahl, G. & Löwen, H. Ionic microgels as model systems for colloids with an ultrasoft electrosteric repulsion: Structure and thermodynamics. *J. Chem. Phys.* **122**, 074903 (2005).

[105] Riest, J., Mohanty, P., Schurtenberger, P. & Likos, C. N. Coarse-graining of ionic microgels: Theory and experiment. *Z. Phys. Chem.* **226**, 711–735 (2012).

[106] Moncho-Jordá, A. Effective charge of ionic microgel particles in the swollen and collapsed states: The role of the steric microgel-ion repulsion. *J. Chem. Phys.* **139**, 064906 (2013).

[107] Denton, A. R. & Tang, Q. Counterion-induced swelling of ionic microgels. *J. Chem. Phys.* **145**, 164901 (2016).

[108] Mohanty, P. *et al.* Dielectric spectroscopy of ionic microgel suspensions. *Soft Matter* **12**, 9705–9727 (2016).

[109] Alberts, B. *et al.* *Molecular Biology of the Cell* (Garland Science, New York, US, 2002), 4th edn.

[110] Stradner, A. *et al.* Equilibrium cluster formation in concentrated protein solutions and colloids. *Nature* **432**, 492–495 (2004).

[111] Liu, J., Nguyen, M. D. H., Andya, J. D. & Shire, S. J. Reversible self-association increases the viscosity of a concentrated monoclonal antibody in aqueous solution. *J. Pharm. Sci.* **94**, 1928–

1940 (2005).

[112] Stradner, A., Cardinaux, F. & Schurtenberger, P. A small-angle scattering study on equilibrium clusters in lysozyme solutions. *J. Phys. Chem. B* **110**, 21222–21231 (2006).

[113] Cardinaux, F., Stradner, A., Schurtenberger, P., Sciortino, F. & Zaccarelli, E. Modeling equilibrium clusters in lysozyme solutions. *Europhys. Lett.* 77, 48004 (2007). 0607264.

[114] Liu, Y. *et al.* Lysozyme protein solution with an intermediate range order structure. *J. Phys. Chem. B* **115**, 7238–7247 (2011).

[115] Cardinaux, F. *et al.* Cluster-driven dynamical arrest in concentrated lysozyme solutions. *J. Phys. Chem. B* **115**, 7227–7237 (2011).

[116] Yearley, E. J. *et al.* Observation of small cluster formation in concentrated monoclonal antibody solutions and its implications to solution viscosity. *Biophys. J.* **106**, 1763–1770 (2014).

[117] Bucciarelli, S. *et al.* Dramatic influence of patchy attractions on short-time protein diffusion under crowded conditions. *Sci. Adv.* **2**, e1601432 (2016).

[118] Braun, M. K. *et al.* Crowding-controlled cluster size in concentrated aqueous protein solutions: Structure, self-and collective diffusion. *J. Phys. Chem. Lett.* **8**, 2590–2596 (2017).

[119] Nawrocki, G., Wang, P.-h., Yu, I., Sugita, Y. & Feig, M. Slow-down in diffusion in crowded protein solutions correlates with transient cluster formation. *J. Phys. Chem. B* **121**, 11072–11084 (2017).

[120] Zhang, Z. & Liu, Y. Recent progresses of understanding the viscosity of concentrated protein solutions. *Curr. Opin. Chem. Eng.* **16**, 48–55 (2017).

[121] Kowalczyk, P., Ciach, A., Gauden, P. A. & Terzyk, A. P. Equilibrium clusters in concentrated lysozyme protein solutions. *J. Colloid Interf. Sci.* **363**, 579–584 (2011). 1106.0597.

[122] Sweatman, M. B., Fartaria, R. & Lue, L. Cluster formation in fluids with competing short-range and long-range interactions. *J. Chem. Phys.* **140**, 03B626_1 (2014).

[123] Baumketner, A. & Cai, W. Equilibrium clusters in suspensions of colloids interacting via potentials with a local minimum. *arXiv preprint arXiv:1603.02176* (2016).

[124] Pini, D. & Parola, A. Pattern formation and self-assembly driven by competing interactions. *Soft Matter* **13**, 9259–9272 (2017).

[125] Baumketner, A. & Cai, W. Clusters of lysozyme in aqueous solutions. *Phys. Rev. E* **98**, 032419 (2018).

[126] Carter, P. Improving the efficacy of antibody-based cancer therapies. *Nat. Rev. Cancer* **1**, 118 (2001).

[127] Burckbuchler, V. *et al.* Rheological and syringeability properties of highly concentrated human polyclonal immunoglobulin solutions. *Eur. J. Pharm. Biopharm.* **76**, 351–356 (2010).

[128] Veretout, F. & Tardieu, A. The protein concentration gradient within eye lens might originate from constant osmotic pressure coupled to differential interactive properties of crystallins. *Eur. Biophys. J.* **17**, 61–68 (1989).

[129] Petitt, P. & Forciniti, D. Cold cataracts: a naturally occurring aqueous two-phase system. *J. Chromatogr. B* **743**, 431–441 (2000).

[130] Zhao, H., Magone, M. T. & Schuck, P. The role of macromolecular crowding in the evolution of lens crystallins with high molecular refractive index. *Phys. Biol.* **8**, 046004 (2011).

[131] Cicuta, P. & Donald, A. M. Microrheology: a review of the method and applications. *Soft Matter* **3**, 1449–1455 (2007).

[132] Moschakis, T. Microrheology and particle tracking in food gels and emulsions. *Curr. Opin. Colloid In.* **18**, 311–323 (2013).

[133] Moschakis, T., Murray, B. S. & Dickinson, E. Particle tracking using confocal microscopy to probe the microrheology in a phase-separating emulsion containing nonadsorbing polysaccharide. *Langmuir* **22**, 4710–4719 (2006).

[134] Imoto, T. & Yagishita, K. A simple activity measurement of lysozyme. *Agr. Biol. Chem. Tokyo* **35**, 1154–1156 (1971).

[135] Liu, Y., Fratini, E., Baglioni, P., Chen, W.-R. & Chen, S.-H. Effective long-range attraction between protein molecules in solutions studied by small angle neutron scattering. *Phys. Rev. Lett.* **95**, 118102 (2005). 0508162.

[136] Stradner, A., Cardinaux, F. & Schurtenberger, P. Comment on "effective long-range attraction between protein molecules in solution studied by small angle neutron scattering". *Phys. Rev. Lett.* **96**, 219801 (2006).

[137] Porcar, L. *et al.* Formation of the dynamic clusters in concentrated Lysozyme protein solutions. *J. Phys. Chem. Lett.* **1**, 126–129 (2010).

[138] Barhoum, S. & Yethiraj, A. NMR detection of an equilibrium phase consisting of monomers and clusters in concentrated lysozyme solutions. *J. Phys. Chem. B* **114**, 17062–17067 (2010).

[139] Falus, P. *et al.* Distinguishing the monomer to cluster phase transition in concentrated lysozyme solutions by studying the temperature dependence of the short-time dynamics. *J. Phys.-Condens. Mat.* **24**, 064114 (2012).

[140] Godfrin, P. D., Valadez-Pérez, N. E., Castañeda-Priego, R., Wagner, N. J. & Liu, Y. Generalized phase behavior of cluster formation in colloidal dispersions with competing interactions. *Soft Matter* **10**, 5061–5071 (2014).

[141] Godfrin, P. D. *et al.* Short-Time Glassy Dynamics in Viscous Protein Solutions with Competing Interactions. *Phys. Rev. Lett.* **115**, 228302 (2015).

[142] Riest, J., Nägele, G., Liu, Y., Wagner, N. J. & Godfrin, P. D. Short-time dynamics of lysozyme solutions with competing short-range attraction and long-range repulsion: Experiment and theory. *J. Chem. Phys.* **148**, 065101 (2018).

[143] Bucciarelli, S. *A scattering study of concentrated lens protein solutions and mixtures-Towards understanding the molecular origin of presbyopia* (Physical Chemistry, Lund University, 2015).

[144] Tardieu, A., Vérétout, F., Krop, B. & Slingsby, C. Protein interactions in the calf eye lens: interactions between β-crystallins are repulsive whereas in γ-crystallins they are attractive. *Eur. Biophys. J.* **21**, 1–12 (1992).

[145] Bucciarelli, S. *et al.* Unusual dynamics of concentration fluctuations in solutions of weakly attractive globular proteins. *J. Phys. Chem. Lett.* **6**, 4470–4474 (2015).

[146] Pawley, J. *Handbook of biological confocal microscopy* (Springer Science & Business Media, 2010).

[147] Heintzmann, R. & Ficz, G. Breaking the resolution limit in light microscopy. *Brief. Funct. Genomics* **5**, 289–301 (2006).

[148] Jenkins, M. C. & Egelhaaf, S. U. Confocal microscopy of colloidal particles: towards reliable,

optimum coordinates. *Adv. Colloid Interfac.* **136**, 65–92 (2008).

[149] Crocker, J. C. & Grier, D. G. Methods of digital video microscopy for colloidal studies. *J. Colloid Interf. Sci.* **179**, 298–310 (1996).

[150] Han, Y., Ha, N., Alsayed, A. & Yodh, A. Melting of two-dimensional tunable-diameter colloidal crystals. *Phys. Rev. E* 77, 041406 (2008).

[151] Royall, C. P., Louis, A. A. & Tanaka, H. Measuring colloidal interactions with confocal microscopy. *J. Chem. Phys.* **127**, 044507 (2007).

[152] Cho, J. K., Meng, Z., Lyon, L. A. & Breedveld, V. Tunable attractive and repulsive interactions between ph-responsive microgels. *Soft Matter* **5**, 3599–3602 (2009).

[153] Savin, T., Spicer, P. T. & Doyle, P. S. A rational approach to noise discrimination in video microscopy particle tracking. *Appl. Phys. Lett.* **93**, 024102 (2008).

[154] Urban, C. & Schurtenberger, P. Characterization of turbid colloidal suspensions using light scattering techniques combined with cross-correlation methods. *J. Colloid Interf. Sci.* **207**, 150–158 (1998).

[155] Peña-Rodríguez, O., González Pérez, P. P. & Pal, U. Mielab: a software tool to perform calculations on the scattering of electromagnetic waves by multilayered spheres. *Int. J. Spectrosc.* **2011** (2011).

[156] Gillespie, D. T. & Seitaridou, E. *Simple Brownian diffusion: an introduction to the standard theoretical models* (Oxford University Press, 2013).

[157] Allen, M. P. & Tildesley, D. J. *Computer simulation of liquids* (Oxford university press, 2017).

[158] Savin, T. & Doyle, P. S. Static and dynamic errors in particle tracking microrheology. *Biophys. J.* **88**, 623–638 (2005).

[159] Valentine, M. T. *et al.* Investigating the microenvironments of inhomogeneous soft materials with multiple particle tracking. *Phys. Rev. E.* **64**, 061506 (2001).

[160] Josephson, L. L., Furst, E. M. & Galush, W. J. Particle tracking microrheology of protein solutions. *J. Rheol.* **60**, 531–540 (2016).

[161] Tuson, H. H., Renner, L. D. & Weibel, D. B. Polyacrylamide hydrogels as substrates for studying bacteria. *Chem. Commun.* **48**, 1595–1597 (2012).

[162] Cheng, C.-J., Chu, L.-Y., Zhang, J., Wang, H.-D. & Wei, G. Effect of freeze-drying and rehydrating treatment on the thermo-responsive characteristics of poly (n-isopropylacrylamide) microspheres. *Colloid Pol. Sci.* **286**, 571–577 (2008).

[163] Bergman, M. J. *et al.* A new look at effective interactions between microgel particles. *Nature Comm.* **9**, 5039 (2018).

[164] De Aguiar, I. B. *et al.* Deswelling and deformation of microgels in concentrated packings. *Sci. Rep.* 7, 10223 (2017).

[165] Ghosh, A. *et al.* Linear and nonlinear rheology and structural relaxation in dense glassy and jammed soft repulsive pnipam microgel suspensions. *Soft Matter* (2019).

[166] Rovigatti, L., Gnan, N., Ninarello, A. & Zaccarelli, E. On the validity of the hertzian model: the case of soft colloids. *arXiv preprint arXiv:1808.04769* (2018).

[167] Lopez, C. G. & Richtering, W. Does flory–rehner theory quantitatively describe the swelling of thermoresponsive microgels? *Soft Matter* **13**, 8271–8280 (2017).

[168] Hirotsu, S. Softening of bulk modulus and negative poisson?s ratio near the volume phase transition of polymer gels. *J. Chem. Phys.* **94**, 3949–3957 (1991).

[169] Huang, C., Kobayashi, H., Moritaka, M. & Okubo, M. Hollow particles are produced by the burying of sulfate end-groups inside particles prepared by emulsion polymerization of styrene with potassium persulfate as initiator in the absence/presence of a nonionic emulsifier. *Polym. Chem.-UK* **8**, 6972–6980 (2017).

[170] Rojas, L., Urban, C., Schurtenberger, P., Gisler, T. & von Grünberg, H.-H. Reappearance of structure in colloidal suspensions. *EPL* **60**, 802 (2002).

[171] Holmqvist, P., Mohanty, P., Nägele, G., Schurtenberger, P. & Heinen, M. Structure and dynamics of loosely cross-linked ionic microgel dispersions in the fluid regime. *Phys. Rev. Let.* **109**, 048302 (2012).

[172] Garting, T. & Stradner, A. Optical Microrheology of Protein Solutions Using Tailored Nanoparticles. *Small* DOI:10.1002/smll.201801548 (2018).

[173] Quemada, D. Rheology of concentrated disperse systems and minimum energy dissipation principle - I. Viscosity-concentration relationship. *Rheol. Acta* **16**, 82–94 (1977).

[174] Puertas, A. M., De Michele, C., Sciortino, F., Tartaglia, P. & Zaccarelli, E. Viscoelasticity and stokes-einstein relation in repulsive and attractive colloidal glasses. *J. Chem. Phys.* **127**, 144906 (2007).

[175] Bergenholtz, J. & Fuchs, M. Nonergodicity transitions in colloidal suspensions with attractive interactions. *Phys. Rev. E* **59**, 5706 (1999).

Appendix

IDL guide for dummies

M. J. Bergman and J.M. Meijer

Contents

1 Introduction

1.1 Microscopy and image analysis

The confocal microscope is a very powerful tool for the investigation of phenomena and structures in the colloidal dispersions of interest. By using image analysis routines one can turn the obtained qualitative images of the structures into quantitative data on the particle motion or on the structural properties. The pioneering microscopy study of Perrin in 1920 on the diffusion of colloidal particles to verify Albert Einsteins theory on the Brownian motion in terms of atoms, is a very nice example of extracting physics from microscopy images. Today the advancement of the confocal microscopes and the detectors offers possibilities to do fast time and space resolved measurements of colloidal dispersions. Therefore, it is not surprising that the confocal microscope is abundantly used to study: diffusion, by measuring the mean square displacements; interactions, by determining the pair-correlation functions in dilute suspensions; phase transitions, by determining the local particle structures; and crystal or glassy structures formed by colloidal self-assembly, by tracking the particle positions in three dimensions (3D).

For the analysis numerous routines are available of which the most established method for particle tracking and analysis are the routines from Crocker and Grier ("Methods of Digital Video Microscopy for Colloidal Studies", John C. Crocker and David G. Grier, J. Colloid Interface Sci. 179, 298, 1996) that has been cited already $\sim$ 4000 times. These routines are written in Interactive Data Language (IDL) which is a vectorized, numerical and interactive programming language that can process a large amount of data (typical for image analysis). Most of today's data treatment of confocal images is still done in IDL just like in this manual. Although, for those who prefer other methods the Crocker and Grier routines also have been made available in other programs such as Matlab, Python, GDL (free version of IDL), LabView and C++.

During image acquisition and data treatment there are many things to take into account to make sure that the data treatment is successful. The main purpose of this manual is to instruct you how to get the best data possible using a Leica confocal microscope and how to analyse your data with the IDL routines available at https://github.com/MaximeBergman/IDL-wrappercodes. In the next chapters we will discuss in a detailed step-by-step overview the important points to consider during a confocal experiment and the particle tracking process in IDL. Figure 1.1 shows already an example of the process of finding and tracking bowl-shaped particles using the analysis routines we will describe in this manual.

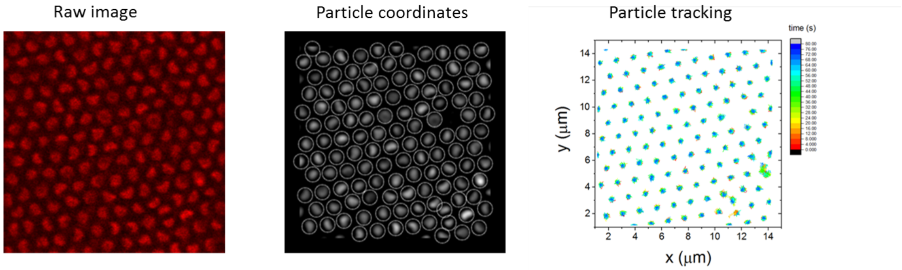
Raw image

Particle coordinates

Particle tracking

Figure 1.1: Example of analysis of confocal images of bowl-shaped particles and the particle tracking done with IDL.

1.2 Previous knowledge

In this tutorial we expect you already have some knowledge about the image analysis. We assume that you have read the following background information:

- the online tutorial of Crocker and Grier managed by Eric Weeks at http://www.physics.emory.edu/faculty/weeks//idl/tracking.html
- the (first part of the) paper by Matthew Jenkins about how to get the best data from the confocal and how the image analysis in IDL works. M.C. Jenkins and S.U. Egelhaaf, 'Confocal microscopy of colloidal particles: Towards reliable, optimum coordinates', Advances in Colloid and Interface Science, 136, (2008), 65-92

Also, we recommend first reading through this complete tutorial before you start the analysis process.

1.3 Image analysis process step-by-step

The image analysis process that we will present here is more than just running the IDL routines provided by Crocker and Grier and includes the optimised acquisition of confocal datasets. The whole image analysis procedure can be described as a 4-step process:

- **Step 1: Get good experimental data.**
  Your starting point, the data, needs to be of the highest quality possible.
- **Step 2: Convert to .lif to .tif.**
  In the Leica LAS AF software the data is saved as a '.lif'. This has to be converted to a tiffstack via ImageJ. This is necessary as the 'overhead' info stored in ImageJ is used in our IDL routines!
- **Step 3a: Image analysis - optimisation of finding coordinates.**
  In this part you optimise the analysis parameters for the particle coordinate finding scripts for the first image of the image series. This part can be tricky but over time you will develop a feeling for it.
- **Step 3b: Image analysis - extract all coordinates.**
  Run feature finding procedure with optimised parameters for a a selection of images or full image serie(s).
- **Step 4: Analysis of the coordinates.**
  Once you have the particle coordinates of each image it is time to do further analysis, such as particle tracking to obtain the mean square displacement (MSD) or pair-correlations to obtain the radial distribution function ($g(r)$, and many other analyses.

In the following sections we will describe the important aspects of each of these steps in detail. To make things clearer, we have decided to divide the steps over two Chapters: *Chapter 2. Confocal Measurements* (Step 1 & 2) and *Chapter 4. IDL Image analysis* (Step 3 & 4). In between you will find *Chapter 3. Introduction to IDL* that will cover the basics of IDL.

2 | Confocal measurements

Step 1: Get good experimental data

For quantitative image analysis, your starting point needs to be good - and thus step 1 is to get confocal images of the highest quality possible. It is important to realize that quantitative image analysis is very different from the qualitative analysis you do by eye. Therefore, there are several things to take into account to optimise the data you collect for the image analysis process.

First of all you need to achieve a good signal-to-noise ratio. There are several rules of thumb for making the images of the proper quality to make the image analysis process smooth. Secondly, you will need to think about what it is that you want to extract from the data. Are you interested in dynamics or structural properties? Because the goal changes what makes a good quality dataset for the image analysis. For instance, when you are trying to determine short time dynamics this requires images with a short time step that can be achieved with small image sizes. However, the same data is not very suitable for the analysis of the overall sample structure. In this case you want large overview images to also get information on the long-range correlations between particles. Lastly, it is very important in microscopy that you get proper statistics. In contrast to scattering methods you are only imaging a small part of your sample and therefore it is important to take the following into account. Below information is given on each of these three points.

Signal-to-noise:

- Visible particles. It is very important that the particles are distinguishable from the background noise. If you cannot distinguish the particles, then the software can't either!
- 10 pixel diameter. The IDL routines work best when particles are $\sim$ 10 pixels is diameter. For anisotropic particles a higher number is usually preferred.
- Use the whole dynamic range. Any given pixel has a grey scale value between 0 and 255. Using the whole dynamic range means you make sure you get pixels with value 0 all the way to pixels with value 255 (see also the Jenkins paper for an excellent explanation).This can be checked with the 'Exposure (O)' filter setting in the Leica LAS AF software. This shows you the range of grey values in your image, with overexposed pixels in blue. Try to get the full range by changing the dynamic gain. There is also an auto gain button on the confocal settings which can be used.
- Reduce noise. Or in other words get a good dark background. This can be checked with the 'Exposure (U)' filter setting. This shows you the range of grey values + underexposed pixels in green. Try get a good green background by changing the dynamic offset.

Measurement settings:

- Short time dynamics: Faster is better. Try to scan as fast as possible with still good signal-to-noise ratio. This can be achieved with low (1-4) line averaging, no frame-averaging, high zoom + small image size. Note that due to the way the analysis routines work square image sizes are preferred! For statistics take many images ($\sim$4000) but keep in mind that for 512x512 pixels x 4000 images the data file will be 1 GB(!) which not all computers can handle.
- Long time dynamics: This is of interest for dense systems but can also be useful for truly 2D systems. Take care to not make the time step between images to long. It should be chosen such that a particle does not move to far away from its position in the previous image. Otherwise tracking will not be possible. Line averaging and frame averaging of the images is advised for very long time steps and dense systems to reduce errors in the particle positions.

- Structural analysis: Larger and more is better. Try to take quite large field of views because particles at image edges can cause distortions in the radial distribution profiles. In a fluid it is advised to take a time series while for a crystal it is advised to take many large images at different positions and xyz-series.
- Measurement "in the bulk": If you want to claim you are e.g. 5 μm away from the cover slip to exclude wall interactions, make sure to check the position of the cover slip for each separate measurement. The cover slip is not 100% smooth and variations in the z-position of the cover slip can be large.

Statistics:

- Never base any conclusions on a single image or on one image series.
- For a dilute sample in 2D, take at least 6x4000 frames (xyt).
- For a concentrated sample in 3D, take at least 10 z-stacks (xyz).

Typical experiment

To give an idea of what kind of settings we usually employ in a confocal measurement we now describe the proper acquisition and analysis of a 2D xyt-series of confocal images that you can use as starting point.

List of settings:

- 100x oil immersion objective
- 8000Hz resonance scanner: on
- Bidirectional scanning: on with phase correction: 3.21.
  But check for other magnifications(!), seems to be slightly different
- pixel size: 512x512
- Zoom: 8-10 or 15-20μm x 15-20 μm image dimensions
- Airy unit: 1

- Microgel spheres: Line average: 2, frame average: 1
  Core-shell bowls: Line average: 4, frame average: 1
- After you obtained your data, save as *.lif.

Step 2: From .lif to .tif

Download ImageJ and Bioformats plugin

Before we can analyse the data we have to convert the obtained .lif file of the Leica LAS AF software into single .tif files for image series. The way to do this is by using ImageJ and the BioFormats plugin. This is a major upgrade from LAS AF which only allows you to save each image as a separate .tif and thus makes it very difficult to keep an overview of your data.

Another useful program to download is Irfanview. This is again a freely available program with which you can look quickly (much faster than with Windows photo viewer) through .tif files. In addition, Irfanview has very handy batch conversion tools, to change filenames quickly etc.

- ImageJ is a freely available image processing program developed at the National Institues of Health and can be downloaded at: http://imagej.net/Downloads.
- The BioFormats plugin can be found at: https://www.openmicroscopy.org/site/support/bio-formats5.1/users/imagej/.
- Irfanview can be downloaded at: http://www.irfanview.com/

ImageJ and Bio-Formats procedure

With ImageJ and the Bio-Formats plugin you can open the .lif file directly and save the different images as .tif and the image series (xyt,xyz etc.) as tiff-stacks (a single .tif file with multiple frames). In addition, the Bio-Formats plugin allows many other data manipulations directly from the .lif file, such as splitting channels. One of the improvements of using this conversion routing it that overhead information - including dimensions, time step etc.- is stored in the .tif-file, which are directly extracted in the IDL routines used in this manual and save you time and effort by specifying it for each different image series.

Figure 2.1 shows how to import files via the Bio-Formats plugin and the options menu where you can select different features. Here you should select Hyperstack (or Standard ImageJ) and for instance split channels if you have 2 colours in your images. Once you have selected the options, ImageJ will show you the images and series present in the .lif file, as shown in figure 2.2. Select the series of interest and click OK. This will open the files in different windows. Figure 2.2 also displays the size information of the image at the top, in this case the images are 15.5×15.5 μm.

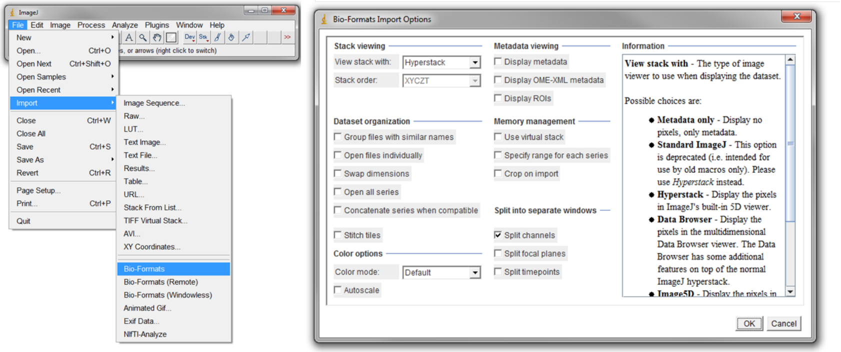

Stack viewing

View stack with: Hyperstack

Stack order: XYCZT

Dataset organization

☐ Group files with similar names

☐ Open files individually

☐ Swap dimensions

☐ Open all series

☐ Concatenate series when compatible

☐ Stitch tiles

Color options

Color mode: Default

☐ Autoscale

Metadata viewing

☐ Display metadata

☐ Display OME-XML metadata

☐ Display ROIs

Memory management

☐ Use virtual stack

☐ Specify range for each series

☐ Crop on import

Split into separate windows

☑ Split channels

☐ Split focal planes

☐ Split timepoints

Information

View stack with - The type of image viewer to use when displaying the dataset.

Possible choices are:

- **Metadata only** - Display no pixels, only metadata.
- **Standard ImageJ** - This option is deprecated (i.e. intended for use by old macros only). Please use *Hyperstack* instead.
- **Hyperstack** - Display the pixels in ImageJ's built-in 5D viewer.
- **Data Browser** - Display the pixels in the multidimensional Data Browser viewer. The Data Browser has some additional features on top of the normal ImageJ hyperstack.
- **Image5D** - Display the pixels in

Figure 2.1: How to run the Bioformat plugin and the options menu. Hyperstack or Standard ImageJ and split channels are advised to be selected for image xyt- or xyz-series of the confocal.

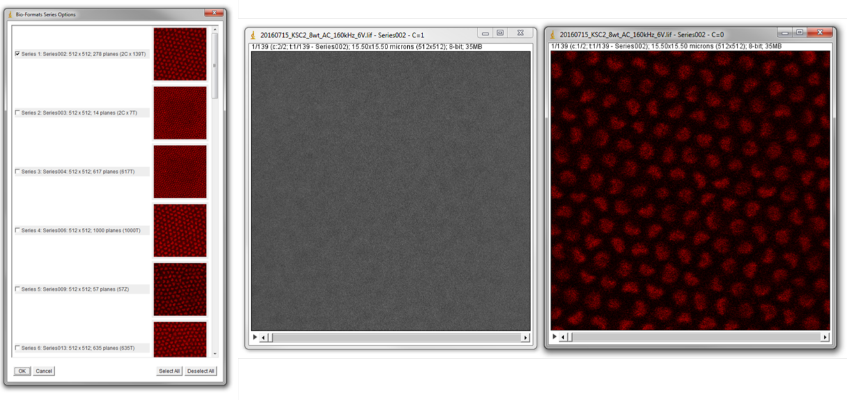

☑ Series 1: Series002: 512 x 512; 278 planes (2C x 139T)

☐ Series 2: Series003: 512 x 512; 14 planes (2C x 7T)

☐ Series 3: Series004: 512 x 512; 617 planes (617T)

☐ Series 4: Series006: 512 x 512; 1000 planes (1000T)

☐ Series 5: Series009: 512 x 512; 57 planes (57Z)

☐ Series 6: Series013: 512 x 512; 635 planes (635T)

```
1/139 (c:2/2; t:1/139 - Series002); 15.50x15.50 microns (512x512); 8-bit; 35MB
```

```
1/139 (c:1/2; t:1/139 - Series002); 15.50x15.50 microns (512x512); 8-bit; 35MB
```

Figure 2.2: Selecting the series and produced files by ImageJ providing two image stacks for the two different detector channels and size information.

3 | Introduction to IDL

3.1 Install IDL

Now that we have optimised the image quality it's IDL time. For the routines to work properly you need to have IDL 8.4 installed and licensed. This is something to ask whomever is in charge of the IDL licenses.

3.2 Download image analysis routines

Download all three zip-packages with the standard image analysis routines from here: http://www.physics.emory.edu/faculty/weeks//idl/download.html.
It is important that you unpack the files in a sensible directory, e.g. D:/Mydata/IDLprogs.
Due to the way the routines were written there can be **NO** spaces in the folder names!

Next, download the wrapper codes from https://github.com/MaximeBergman/IDL-wrappercodes.

3.3 Starting IDL

IDL is started by clicking the item in the startup menu or the shortcut on the desktop or wherever you decided to place the program. When the programs starts up it will ask you to specify a working directory, to see how to handle this see Section 3.3.2. After this has been selected the IDL program will open.

3.3.1 IDL Workspace

The interface of IDL is divided into two parts; the console and the editor. In the console you can type direct commands and directly get a result. In the editor you can write scripts, or in IDL terminology procedures or functions, that consist of several commands that will be executed. Figure 3.1 shows a screen shot of the IDL interface where the console and the editor are indicated.

3.3.2 Change working directory

You have to change your working directory in IDL to make sure it will find the correct procedures during the image analysis process. Go to window and select preferences, see figure 3.2, left panel. A window will open, select IDL on the left. This will show you a number of settings including 'Initial working directory', see figure 3.2, right panel. This is the working directory every time you start up IDL. Change this to the folder where you have saved all the IDL procedures you downloaded before. Next, make sure that all the paths are loaded. This is done by selecting paths in the preferences window, as shown in Figure 3.3. Now all the procedures should be in your library and when called upon IDL should recognise the procedures.

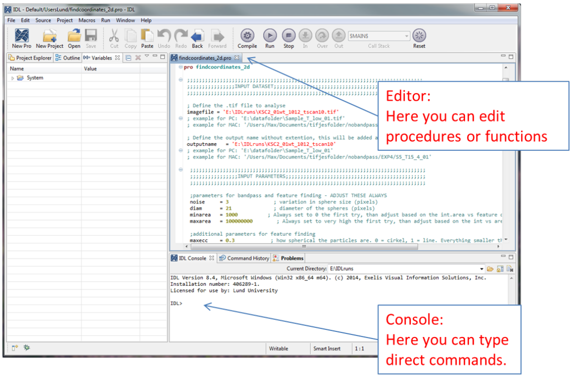

```
pro findcoordinates_2d

;;;;;;;;;;;;;;;;;;;;;;;;;;;;;;;;;;;;;;;;;;;;;;;;;;;;;;;;;;;;;;;;;;;;;;;;;;;;;;;;
;;;;;;;;;;;;;;;;INPUT DATASET;;;;;;;;;;;;;;;;;;;;;;;;;;;;;;;;;;;;;;;;;;;;;;;;;;
;;;;;;;;;;;;;;;;;;;;;;;;;;;;;;;;;;;;;;;;;;;;;;;;;;;;;;;;;;;;;;;;;;;;;;;;;;;;;;;;

; Define the .tif file to analyse
imagefile = 'E:\IDLruns\KSC2_01wt_1012_tscan10.tif'
; example for PC: 'E:\datafolder\Sample_T_low_01.tif'
; example for MAC: '/Users/Max/Documents/tifjesfolder/nobandpass

; Define the output name without extention, this will be added a
outputname   = 'E:\IDLruns\KSC2_01wt_1012_tscan10'
; example for PC: 'E:\datafolder\Sample_T_low_01'
; example for MAC: '/Users/Max/Documents/tifjesfolder/nobandpass/EXP4/S5_T15_4_01'

 ;;;;;;;;;;;;;;;;;;;;;;;;;;;;;;;;;;;;;;;;;;;;;;;;;;;;;;;;;;;;;;;;;;;;;;;;;;;;;;
 ;;;;;;;;;;;;;;;;INPUT PARAMETERS;;;;;;;;;;;;;;;;;;;;;;;;;;;;;;;;;;;;;;;;;;;;;;;
 ;;;;;;;;;;;;;;;;;;;;;;;;;;;;;;;;;;;;;;;;;;;;;;;;;;;;;;;;;;;;;;;;;;;;;;;;;;;;;;

 ;parameters for bandpass and feature finding - ADJUST THESE ALWAYS
 noise     = 3              ; variation in sphere size (pixels)
 diam      = 21             ; diameter of the spheres (pixels)
 minarea   = 1000         ; Always set to 0 the first try, than adjust based on the int.area vs feature c
 maxarea   = 100000000        ; Always set to very high the first try, than adjust based on the int vs are

 ;additional parameters for feature finding
 maxecc    = 0.3            ; how spherical the particles are. 0 = cirkel, 1 = line. Everything smaller th
```

```
IDL Version 8.4, Microsoft Windows (Win32 x86_64 m64). (c) 2014, Exelis Visual Information Solutions, Inc.
Installation number: 406289-1.
Licensed for use by: Lund University

IDL>
```

Editor:
Here you can edit procedures or functions

Console:
Here you can type direct commands.

Figure 3.1: Startup screen IDL

3.4 IDL syntax

Before you start with running the routines we first explain the IDL programming language and the syntax that is used. This will allow you to understand what is hap-

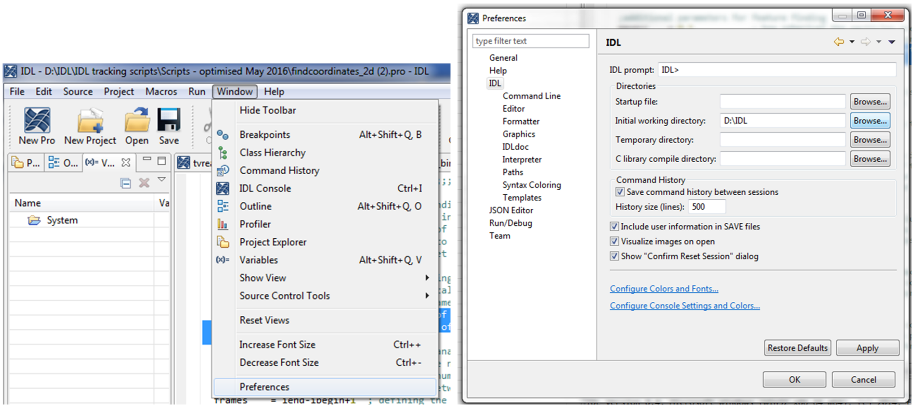

IDL - D:\IDL\IDL tracking scripts\Scripts - optimised May 2016\findcoordinates_2d (2).pro - IDL

IDL prompt: IDL>

Startup file:

Initial working directory: D:\IDL

Temporary directory:

C library compile directory:

☑ Save command history between sessions

History size (lines): 500

☑ Include user information in SAVE files

☑ Visualize images on open

☑ Show "Confirm Reset Session" dialog

Figure 3.2: How to change working directory.

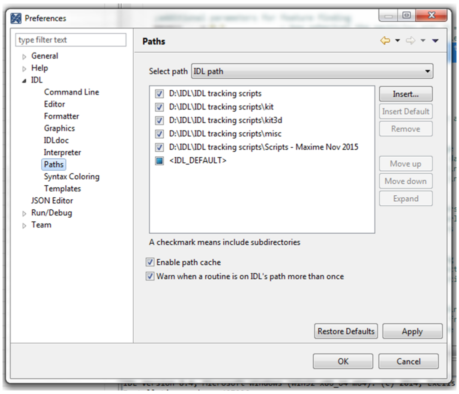

Select path: IDL path

☑ D:\IDL\IDL tracking scripts
☑ D:\IDL\IDL tracking scripts\kit
☑ D:\IDL\IDL tracking scripts\kit3d
☑ D:\IDL\IDL tracking scripts\misc
☑ D:\IDL\IDL tracking scripts\Scripts - Maxime Nov 2015
<IDL_DEFAULT>

A checkmark means include subdirectories

☑ Enable path cache

☑ Warn when a routine is on IDL's path more than once

Figure 3.3: How to add new scripts to your library.

pening during running the routines and will give you the tools to fix small problems that you might encounter during the runs. There are many more things one can do with IDL than we will detail here, but these are beyond the scope of this guide.

3.4.1 Programming language

As the name Interactive Data Language suggests the routines are written in a programming language. For those that are unfamiliar with this term: a programming language is a formal constructed language designed to communicate instructions to a machine, particularly a computer. Programming languages can be used to create programs to control the behaviour of a machine or to express algorithms. A programming language's surface form is known as its syntax. In the case of IDL the programming language is purely textual; it uses sequences of text including words, numbers, and punctuation, much like written natural language.

The syntax of IDL is based on Fortran and some from C. So for those familiar with these languages many things will be self-explanatory. For those that have no experience with programming here we will explain a few of the basics of IDL syntax.

3.4.2 Special characters

In IDL certain characters have special functions. Some of these seem simple, like the equation sign that prompts a evaluation of the expression on the right side and will store it in the left variable. In addition, there are other special signs that will cause a specific effect in IDL. Table 3.1 contains the most commonly used characters in the IDL procedures:

Table 3.1: Special characters and their function in IDL

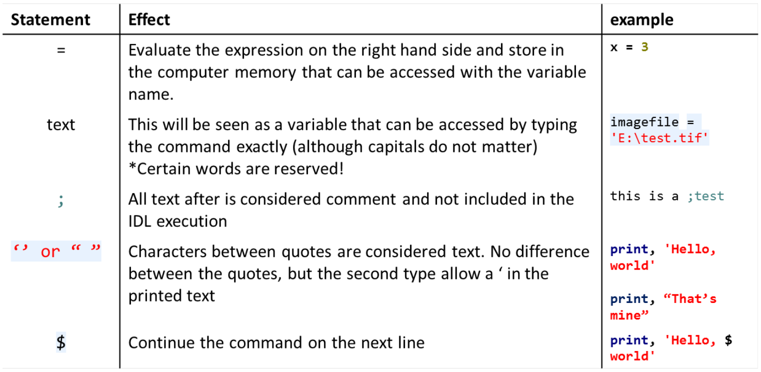

Statement	Effect	example
=	Evaluate the expression on the right hand side and store in the computer memory that can be accessed with the variable name.	`x = 3`
text	This will be seen as a variable that can be accessed by typing the command exactly (although capitals do not matter) *Certain words are reserved!	`imagefile = 'E:\test.tif'`
;	All text after is considered comment and not included in the IDL execution	`this is a ;test`
‘’ or “ ”	Characters between quotes are considered text. No difference between the quotes, but the second type allow a ‘ in the printed text	`print, 'Hello, world'` `print, “That’s mine”`
$	Continue the command on the next line	`print, 'Hello, $ world'`

3.4.3 Numbers

IDL distinguishes between two different number types: integers and floating numbers. The integer numbers are defined as numbers with no fractional part and a finite number of digits. In Table 3.2 the three different types of integers are defined, BYTE, INT and LONG. The difference between the numbers is how much space they will take up in the memory and how long the numbers can be. Floating numbers are numbers that have decimal numbers. There is only one way to store these in the memory, namely as a FLOAT and are practically unlimited in size, as shown in Table 3.3.

Table 3.2: Syntax of integer numbers and the values IDL can assign

Notation	Statement	Number type
BYTE	#B	8-bit integer 8-bit binary numbers: 2^8 = 256 numbers, range: 0-255
INT	#S	16-bit (2-byte) integer Range; -32768 to 32767
LONG	#L	32-bit (4-byte) integer Range: -2^{31} to 2^{31}-1

Table 3.3: Syntax of decimal numbers and the values IDL can assign

Notation	Statement	Number type
FLOAT	#.#	Single precision floating-point number Seven to eight decimal digits, range: ~-3.4x10^{38} to ~ 3.4x10^{38}

The reason we specify this nature of IDL is very practical. IDL automatically interprets the values that are put into a script as one of these types. For instance, IDL automatically interprets the input: `x = 2` as an INT and `x = 2.2` as a FLOAT. Additionally, an INT will be turned into a LONG if needed. However, this automatic interpretation can give problems, especially with calculations. The main importance is that in the procedures that will be discussed later, you will be asked to provide certain values for calculations and it is important to keep in mind that a 1 can be used for iterations, but a 1.0 cannot. Vice versa, in calculations using a 1 might lead to rounded off values (integers only) so using 1.0 is best. Many of the typical errors seen during running of the routines are caused by incompatible number types. Another example is exceeding the maximum value of 32767 for INT. IDL will simply continue counting starting at -32768 which will lead to strange results.

Note: Another thing that has to be remarked about IDL is that counting starts at 0. So the first image in an image series will be identified as 0.

3.4.4 (Reserved) variables

Essentially, you can define any variable name in IDL and you are only limited by your own imagination. Although for obvious reasons, one might want to keep variable names short and self-explanatory. Also important to note here is that IDL is **case insensitive** (and indentation insensitive). So the commands: ”print, ” ”PRINT, ” and

”PrInT,” will all result in the same action. It is therefore also not cucial to remember capitals in the procedure names (like one has to do in Matlab for instance and this makes programming much easier!). There are however several variable names that are reserved for commands or functions in IDL. Table 3.4 shows the list of these words.

Table 3.4: List of IDL reserved words.

AND
BEGIN
BREAK
CASE
COMMON
COMPILE_OPT
CONTINUE
DO
ELSE
ENDCASE
ENDELSE
ENDFOR
ENDIF
ENDREP
ENDSWITCH
EQ
FOR
FORWARD_FUNCTION
FUNCTION
GE
GOTO
GT
IF
INHERITS
LE
LT
MOD
NE
OF
ON_IOERROR
OR
PRO
REPEAT
SWITCH
THEN
WHILE
XOR

3.4.5 Procedures and functions

IDL has hundreds of built-in procedures, functions and calculations that make it easy to display and analyse your data. Table 3.5 shows you some of the procedures and functions that are available and their names are quite self-explanatory. Note that the colour will tell you about the nature of the statement; dark blue: procedure, light blue: function, and bright blue: calculation on array. Of course there are many more options available but for those we refer you to the IDL help function. The scripts that are used for image analysis be used are mainly procedures that can be recognized by the .pro ending of the files.

Table 3.5: Examples of procedures and statements in IDL

Command	Action
`print,`	Prints the following statements
`help,`	Provides information on the following statements

Function	Action
`plot,`	Plots the following array
`window,`	Opens a window

Calculation	Action
`max()`	Determines the maximum of an array
`mean()`	Determines the mean of an array

3.4.6 IDL syntax in use

Here we show a few examples of how commands typed into IDL will be processed. We recommend you to try the commands yourself in the console window.

You can make IDL print a text:

```
IDL> print, 'Hello, world'
Hello, world
```

Do a calculation and print the result:

```
IDL> print, 3 + 5
       8
```

Define a variable, check the variable and print the result:

```
IDL> x = 3 + 5
IDL> help, x
X               LONG       = 8
IDL> print, x
       8
```

(variable name, type and value)

In IDL one mainly uses arrays of numbers. Note that a single array is also called a vector. In this example we first define an integer array:

Do a calculation with the integer array, transforming it into a floating point array:

```
IDL> A = [1, 2, 3, 4, 5, 6]
IDL> help, A
A                INT       = Array[6]
IDL> print, A
       1       2       3       4       5       6
```

```
IDL> B = COS(A)
IDL> help, B
B                FLOAT     = Array[6]
IDL> print, B
     0.540302    -0.416147    -0.989992    -0.653644     0.283662     0.960170
```

```
IDL> plot, A, B
```

Plot one array versus the other:

The plot function will open a window and plot the result:

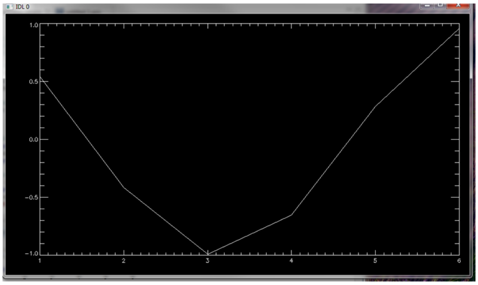

3.5 Running IDL - basics

3.5.1 Editing procedures

The analysis routines of Crocker and Grier, and of Maxime and Janne-Mieke are provided as procedures and can be edited in the editor window. IDL distinguishes between two types of scripts, namely procedures and functions (as mentioned earlier). There is a slight difference but this is unimportant for now. In the editor they are defined by 'pro' or 'function' followed by the filename, different commands or statements and an 'end' statements as shown in figure 3.4. If one of these four items is missing or encountered too late or too soon an error message will be given by IDL during the run. Also, if the filename is not **exactly** the same as the name used to save it on the hard disk, IDL will not be able to find the script, resulting in another error message.

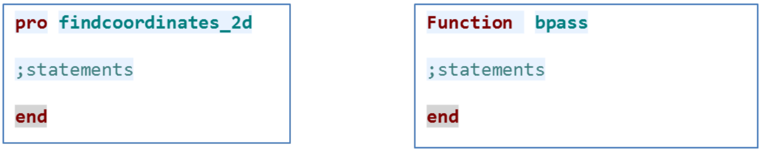

```
pro findcoordinates_2d

;statements

end
```

```
Function  bpass

;statements

end
```

Figure 3.4: The way procedure and function are defined in a script in the IDL editor.

3.5.2 Naming and saving procedures

It is important to note here that due to the way IDL handles variables and file names IDL will recognize two .pro files with the same name in different folders as the same. Therefore, **never save scripts under the same name!** If you call on one of these procedures IDL will search through its workspace and use the first file it finds and if these two scripts are different it will lead to different results. So make sure you do not store the same files at different places and not to rename scripts with previously used names!

Luckily, IDL is interactive and automatically provides a colour for the typed text, according to the type of file it is associated with. So typing the handle for a '.pro' file will turn it light blue and bold, because IDL has found a procedure named the same. This is also a handy feature to avoid using variable names that refer to a procedure or function.

3.5.3 Running procedures

To execute the statements written in a procedure you have to take two steps. 1. The procedure must be compiled, in this step IDL checks the code to see if there are no errors in the statements and saves the current version. 2. The procedure must be run, in this step all the statements are executed in a row.

The compilation step is necessary after each modification of the procedure. If you don't compile, IDL will use the last saved version from the hard disk that contains the old variables. You can tell by the asterisk after the procedure name in the editor that the script was modified after the last compilation and that you need to compile again. If a procedure calls on other procedures these will be automatically compiled by IDL before they are executed.

The compiling and running in IDL are relatively easy, just press the buttons as shown in Figure 3.5. In case you know something is wrong, you can stop the execution with the stop button. In case you prefer to type the commands in the console you should use the commands shown in the table in Figure 3.5.

Once a procedure is running it will produce output in the form of text in the console window, windows that are opened and in which data is plotted and files that are saved directly to the hard drive.

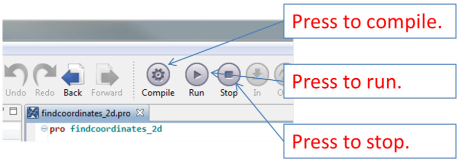

Press to compile.

Press to run.

Press to stop.

Action	Console command
Compile	`.compile` or `.com` + procedure name
Run	`.run` or `.r` + procedure name
Stop	`crtl + c`

Figure 3.5: (a) Buttons and (b) commands in IDL to compile, run and stop a procedure.

3.5.4 Saving data

There are many commands available in the IDL language to write away data as .tiff, .jpg, .txt, etc. While most of these data types can be opened by other programs, the optimal file type for IDL is the .gdf file, which cannot be opened by other programs so readily. Therefore, often we create the output twice - once as a .gdf file and once as a .dat file in case we want to have a quick look.

4 | IDL image analysis

Step 3a: Image analysis - Optimisation of finding coordinates.

The process of image analysis consists of running several different procedures in a row. It is crucial that you optimise the result from each routine before you move to the next. In the following sections we will walk you through all the routines and the optimisation to be performed in each procedure.

- Before you start make sure that the proper working directory (folders where the .pro files are saved, as discussed above) is selected in IDL.
- Also remember that for simplicity here we describe the analysis of a 2D xyt-image series.

Overview of analysis procedures

The analysis we performed is based on the freely available procedures of Crocker and Grier. The analysis process of confocal images consists of several different steps. Although we assume you have gone through the explanation of the image analysis process online, we want to make sure that you understand the most important steps that are taken in the analysis process that can be performed using the codes of Crocker and Grier:

- Bandpass filter: improving the image quality. The noise in the images is reduced by averaging the neighbouring pixels and features of interest are enhanced by a top-hat filter. This should lead to well-defined and separated particles in the images.

- Feature finding: finding the particles. In this step features in the images are identified and by using selection criteria, you can select the particles of interest.
- Radial distribution $g(r)$ function: Determines the radial distribution of the feature coordinates. This requires the coordinate file as input. For stacks of images it can determine an average $g(r)$.
- Particle tracking: Link the coordinates found in each frame together to form trajectories. Requires the coordinate file of a series of images.
- Mean square displacement: Calculates the mean square displacement for a series of images in which the particles have been tracked. Requires the tracked file as input.

Although excellent explanations of the procedures and how to run them are available, the loose procedures require you to type many commands before the desired result is obtained. For this reason we have written several macro-procedures that call on the procedures of Crocker and Grier. These macros make it easier to compile, run and check the image analysis process as well as optimising the analysis parameters based on a more or less 'click and go' principle. This means you change parameters in the Janne-Mieke & Maxime procedures, and you do not change anything in the Crocker & Grier procedures. Figure 4.1 shows a flowchart of the macro-procedures we wrote and the order these have to be run in, as certain procedures require the output from others. Here we also specify which Crocker and Grier procedures are called upon in the macro-procedures and what the input and output of each of the macros is.

In the next sections we describe in detail for each of the procedures which parameters have to be changed in the IDL editor and what the effect of these parameters is on the image analysis.

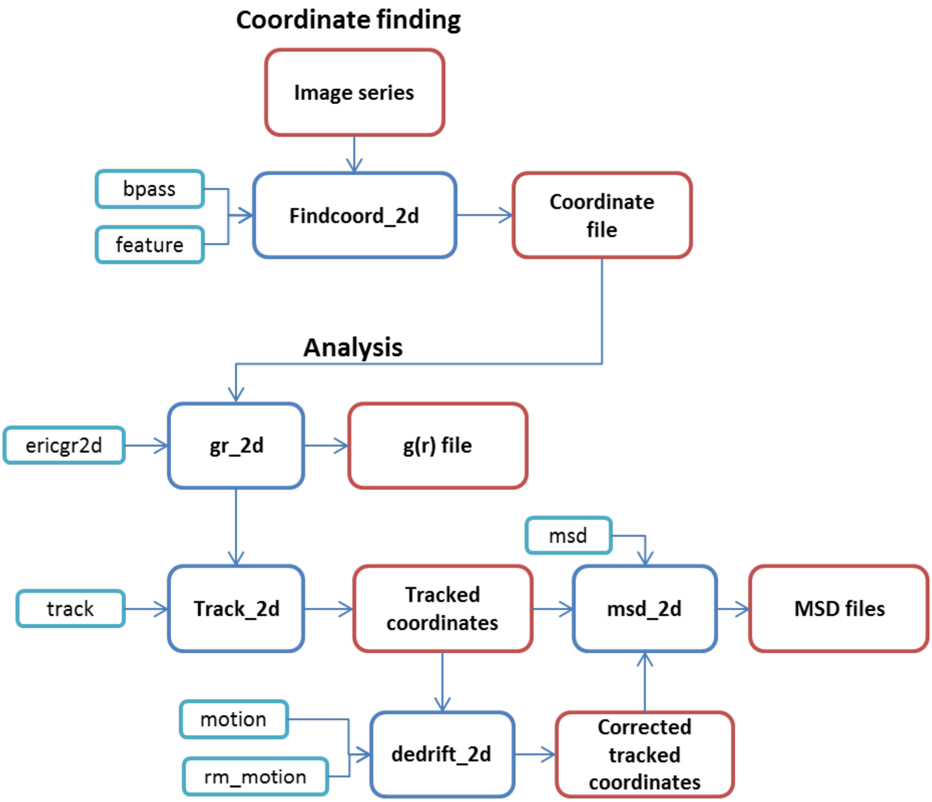

Figure 4.1: Flowchart of the IDL analysis routines for a 2D confocal image series and the different procedures (dark blue) that should be used, which rely on the routines of Crocker and Grier (light blue) and the data that is used and produced (dark red).

Finding coordinates - `findcoord_2d.pro`

The first - and most important - of the image analysis procedures is `findcoord_2d.pro`. In this procedure both the bandpass filter and feature finding procedure are used. The input files are the image series you wish to analyse as a tiffstack (*.tif) made with ImageJ and the output will be the following:

- two coordinate files (*_crd.dat and *_crd.gdf) with the x- and y-coordinates in μm and image number of the identified particles among some other information.
- (Coordinates of the first image are saved as '*_fr0_0_crd.dat' while any other image selection is saved as '*_fr##_##_crd.dat', to avoid mixing up datasets. Here fr stands for frame, which refers to an image in the image series. We use this terminology in the procedure scripts.)
- an info file with the settings used (*_crd_info.dat)
- a file with the total number of particles (*_npt.dat)
- a file with the time step between images (*_tstep.dat)
- six windows that will display the data that is analysed, the particles that are found and certain aspects of the analysis.

The input parameters of `findcoord_2d.pro` that have to be optimised can be divided in two groups; (i) those that **have** to be adjusted for each series and (ii) those that **could** be adjusted if needed. The latter parameters function as additional selection parameters or for special cases such as inverted images etc. In Table 4.1 we go through each of the parameters of group (i) and in Table 4.2 for group (ii). In the Tables the function of the parameters is given together with suggestions on how to define the values for your image series and what things to consider before selecting the values.

Table 4.1: List of parameters that HAVE to be adjusted

Parameter	**Explanation**
`imagefile = 'C:/Path/Filename.tif'`	Defines the full image path plus file with extension between apostrophes. Example: 'E:/IDLruns/KSC2_9wt_tscan06.tif'. **Note:** Due to the way the procedures create filenames, the filenames cannot contain spaces.
`outputname = 'C:/Path/Filename'`	Defines the full path with start of filename for the saved files without file extension. Example: 'E:/IDLruns/KSC3_9wt_tscan06'. File extension will be added later in the procedure automatically.
`noise = 2`	Parameter for smoothing the high frequency noise in the images by averaging intensities from surrounding pixels. `Noise` dictates the range of the averaging, e.g. a value of 2 will average over all the pixels within <2 pixels around. A value of `noise = 1` is advised for particles of 10 pixels in diameter. However, due to oversampling (smaller pixels than true confocal resolution) `noise = 2` can also be used.
`diam = 17`	Size used for gaussian top-hat filter and should always be uneven. Here you fill in the approximate diameter of your particles in pixels. Best way to determine the particle size is by drawing 10 boxes around your particles in ImageJ and taking the average length of these. `Diam` should be ± 2 pixels from the boxes average.
`minarea = 100`	Selection criteria for minimum area of integrated brightness that a found feature should posses, in the Crocker and Grier code this corresponds to the parameter `masscut`. This is needed to exclude noise that is identified as a feature. However, it is also used for distinguishing between out-of-focus and in-focus particles. At start of optimisation this value should be set relatively low `minarea = 100-1000` to exclude noise features but include all particles and see which value would be the best.
`ibegin = 0`	First frame to use for analysis. Please note IDL starts counting at 0.
`iend = 0`	Last frame to use for analysis. In step 3a we advise you to start with `iend = 0` or `1`. In step 3b set it to the number of images you have. However, the `findcoord_2d` procedure is written such that if the number is too high (e.g. 10000) it will automatically reduce `iend` to the total number of images that are present in the tiffstack.

Table 4.2: List of additional parameters that COULD to be adjusted

Parameter	**Explanation**
`step = 1`	Defines step size between frames, usually not adjusted `step = 1`. Changing the value is only useful for specific image series if you want to check different times.
`lowlimit` `uplimit`	If you have a high background noise, you can use `lowlimit` to take only into account pixel intensities higher than the specified value. If your background has an intensity of 50 (check this with ImageJ), you set `lowlimit = 50` and every pixel with intensity <50 gets reset to intensity=0.
`maxecc = 0.1`	Eccentricity indicates how spherical your particles need to be, 0 = perfect spheres, 1 = line. Usually out-of-focus particles and noise are not spherical at all (eccentricity > 0.5). Typical values are 0.1 for spheres and 0.7 for bowl-shaped particles. Please note that if all feature eccentricities in a frame are > `maxecc`, nothing is thrown away.
`mindiam = 0` `maxdiam = 1000000`	Minimum and maximum diameter required to take a particle into account. Standard set to these values. You could use this to filter small noise and also to filter large objects. Often mindiam helps to remove features at the edge of the frame. Please note that if all feature diameters in a frame are < `mindiam`, nothing is thrown away.
`maxarea = 200000`	Maximum area of integrated brightness for a found feature. In case you want to exclude some large objects.
`invertimage = 'no'`	The procedure assumes a dark background and bright features. If you have a bright background and dark features, make this 'yes'.
`quiet = 'yes'`	In case you want to see printing of the data in IDL during the analysis, set to 'no'.
`corrx = 1.0` `corry = 1.0`	Correction factors for *x*- and *y*-scale of the images. This has been added for the case that the confocal calibration is known to be off.
`saved = 'yes'`	If you want to save the bandpassed frames with the found coordinates in them. This directly visualises how well-chosen your parameters are, since you can determine for yourself if you think the software is finding the right particles.
`splitco = 'no'`	In case you want to save the coordinates of each frame separately.
`ballview = 'no'`	In case you want to save the coordinates to use in the program ballviewer, change to 'yes'. This is a easy viewer to look at FCC, HCP or BCC stacking in your crystals.

`clustercheck = 'no'`
`clustervalue = 1.25`
`throwclusters = 'no'`
	If your sample contains clusters, you need to turn on the clustercheck routine, starting by putting `clustercheck` to `` `yes' ``. The additional text in the `findcoord_2d` procedure will inform you about this.

`intcorr = 'no'`
`intcorr_step = 100`
`intcorr_rep = 5`
	If you have bleaching, you need to set to `` `yes' ``. When dye bleaching occurs the intergrated brightness of your particles decreases. We build in a routine that will automatically decrease `minarea` with 5% for a the `intcorr_step` number of frames and will repeat the 5% step `intcorr_rep` times.

Run and optimise parameters

The most important parameters you always need to adjust in `find_coord2d.pro` are `noise`, `diam` and `minarea` (see also Table 4.1). These play a role in the bandpass filter and the feature finding and have the following effects:

- `Noise`.If `noise` is set too low, your particles will still look jagged around the edges in the smoothed image. Too high and your particles become too smoothed out and particle edges are hard to define. This also means that your particle centre is less well defined, leading a decreased accuracy in the particle coordinates.
- `Diam`. If this value is set properly, spherical particles will appear round and slightly homogeneous. If this value is too high, the particles will start to be smeared and 'stick' together, while if this value is too low it can cause the software to create 'donuts' of your particles and it will find multiple features in one particle.
- `Minarea`. This is used to exclude noise and out-of-focus particles. This parameter only works well when the data is of proper quality. For instance overexposed particles result in particles with the same intensity in and out of focus and no selection can be made. It is important to make sure that particles have ranges of total area of integrated brightness. The `minarea` value is highly dependent on the image settings used during acquisition and needs to be checked for each image series.

After you have set all the parameters it is time to run the procedure by clicking `compile` followed by clicking `run`. During the run IDL will open three windows in which it will display the result of the analysis procedure. Figure 4.2 shows from left to right the original image, the bandpass filtered image + found features, and original image + found features.

- The first thing to check is the bandpass filter in window 2. The particles should look round and well-separated. If jagged edges are present the `noise` is set too low and when particles are not well separated then `diam` is too high. You have to find the balance between increased roundness of the particles and staying as close to the data as possible. Putting `noise` and `diam` both too high, will lead to a decreased accuracy of the particle coordinates as the images becomes to smeared. However, untreated data will also lead to a decreased accuracy due to noise and difficulty in identifying the particles.

- The second thing to check is that features that are identified correspond to real particles. The feature positions the procedure has found are identified by circles. The size of the circles is set to the feature diameter and helps to establish if this is chosen correctly. Adjust this if necessary. If too many particles are found the first step is to increase `minarea`. If no particles are found start by decreasing `minarea`.

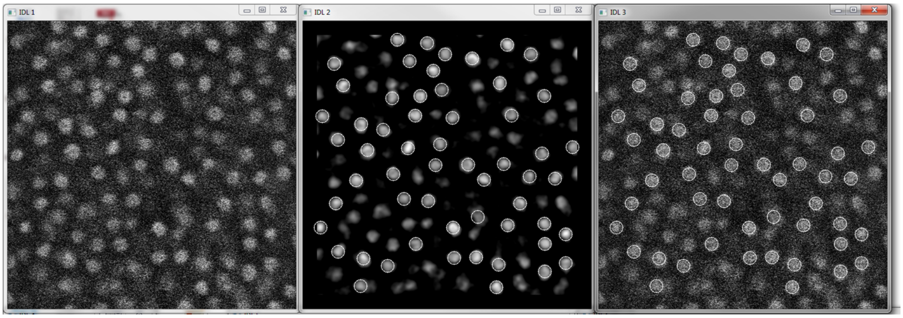

Figure 4.2: Output from IDL: from left to right original data, bandpassed data + found features and original data + found features

Optimising `minarea`

One of the most difficult parameters to tune is `minarea`, which unfortunately also has the biggest effect on the final feature selection. Our way of checking the selection of `minarea` is by running the image analysis first with `minarea` set quite low; in this case `minarea = 1000`. Next, we take a look at the second row of three windows IDL produces. Figure 4.3 shows the three windows with from left to right: sub-pixel accuracy, integrated area of brightness histogram, and integrated area of brightness versus radius plot, which we refer to as the particle cloud.

The particle cloud is also a good check for the quality of your data: good data produces a linear (horizontal) cloud of similar radius but different brightness, while bad data will produce a diagonal cloud that increases in intensity while increasing in brightness at the same time. **Note:** For diluted samples it might be needed to increase `iend` to analyse multiple images to get a proper particle cloud. The analysis shown in figure 4.3 is actually obtained from the first 10 images of a 4000 image series. Here the data is of good quality but due to some oversampling the particle cloud is not fully linear.

The method to refine and determine the best value of `minarea` is the following:

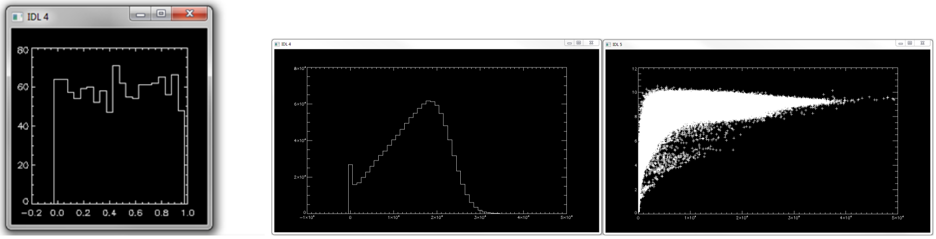

Figure 4.3: Output from IDL. (top) subpixel accuracy (bottom left) integrated are of brightness histogram and (bottom right) integrated area of brightness versus radius plot.

- Check the histogram of the sub-pixel accuracy in the *x*-coordinate because it tells you how good the resolution in is your images (i.e. Figure 4.3, top). If you find clear peaks around 0 and 1 this indicates that the sub-pixel resolution is not high and you might want to change some of the other parameters. It might also be related to the quality of your data. For particles with ∼10 pixels in diameter sub-pixel accuracy should be achievable. Setting `diam` higher will lead to increased sub-pixel accuracy, but you should not stray too far from your original data. In that case, just accept you do not have sub-pixel accuracy and don't try to resolve anything below 1 pixel.

- Check the particle cloud (Figure 4.3, bottom right). The features of interest will in general have the same radius and different intensities depending on their focal position. Features originating from noise and out-of-focus particles will have a lower brightness and radius and thus fall in the lower left part of the particle cloud. From the position of the cloud we can get a first estimate of a proper `minarea` and if needed also determine a `mindiam` value.

- Use the maximum of the histogram to determine at which brightness, $\mathrm{I}_{\mathrm{max}}$, the highest number of particles is found (Figure 4.3, bottom left). These particles are the ones in-focus. Of course some particles will be slightly less bright and we employ `minarea = ` 0.7 - 0.8 × $\mathrm{I}_{\mathrm{max}}$, for selecting the in-focus particles and excluding the out-of-focus particles.

Fine-tuning `minarea` using $g(r)$

In the case of dilute samples selecting a proper `minarea` can be difficult even with the particle cloud and brightness histogram. This is problematic as these measurements are usually done to measure particle interactions and thus need to be very trustworthy. Another fine-tuning method that can be performed involves an examination of the evolution of the radial distribution function, $g(r)$, for different `minarea` values. How exactly to run the $g(r)$ procedure is explained below, but we skip over that for now.

You will need to run your image analysis at increasing `minarea` (e.g. steps of 10000, or 5000), followed by the $g(r)$ procedure (make sure to change the output name to be able to compare the data later!). By reducing the number of out-of-focus particles the $g(r)$ peaks will become sharpened (Figure 4.4a). In addition, the first $g(r)$ peak will also shift slightly to higher r, as out-of-focus particles appear closer in the 2D projection. If your peak height decreases or your peak position does not stabilise with increasing `minarea`, finding an objective, quantitative $g(r)$ will very challenging (Figure 4.4b).

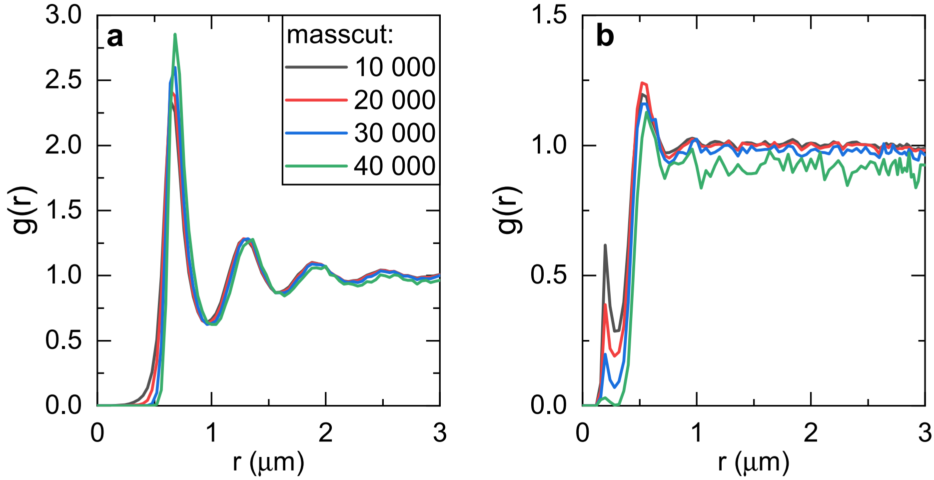

Figure 4.4: Evolution of g(r) with increasing minarea (legend reflect minarea values) for good dataset (panel a) and challenging dataset (panel b)

Good data: The `minarea` selection in the case of the good data in figure 4.4a is done as follows:

- Check the `minarea = 0` curve. In this case there is a shoulder at $r <$ diameter of the particles. We see this shoulder disappear with increasing `minarea`. Therefore, we can conclude that the shoulder is caused by out-of-focus particles.
- With increasing `minarea` the first peak position shifts to larger r until it stabilises. This is again an indication that out-of-focus particles are removed.

- However, at very high `minarea` the $g(r)$ is becoming very noisy due to the low statistics and the peak will shoot up.
- The best `minarea` is high enough to remove the shoulder and have a stable $g(r)$ peak position and that does not make the $g(r)$ curve too noisy. This `minarea` should be comparable to the values you have found with the methods described above.

There is thus four different approaches to determining the correct `minarea`; these should all converge and lend some objectivity to your chosen value. If you want, you can also play around with the other parameters but using `minarea` to discard out-of-focus particles has shown to be the most efficient. For example, the maximum eccentricity can be set higher to allow more erratically shaped particles to be included. Also if needed, you can include either the cluster exclusion algorithm or the bleaching correction algorithm. If you do so, you will need to play around again with the relevant parameters in order to find the optimum settings.

Challenging data: A typical example of difficult data is shown in Figure 4.4b. Here we see that increasing the masscut does not improve the quality of the $g(r)$. Instead, with increasing masscut, the peak height decreases, the shoulder remains and the peak position does not stabilise. Clearly it will be very challenging to find a convergent value for `minarea`. Because of the stringent settings, it is likely that you are throwing away out-of-focus particles, or slightly too eccentric particles, which are necessary due to low statistics. If your $g(r)$ behaves like this, there are two options. The first is the least time-consuming: go back to the confocal and repeat the measurements with different settings and higher image quality. For instance, at high temperatures particles move faster, and it might be advisable to use a higher zoom so that particles can be tracked better. Perhaps faster scanning speed can also alleviate the problems, if it does not impact the resolution, i.e. reducing the image size from 512x512 pixels to 512x256 or 256x256 pixels. The second option is to play around with eccentricity, minimum diameter, bandpass filtering, etc. Because the data does not really converge, it can take a lot of time before you arrive at a $g(r)$ that you are confident in. We therefore recommend taking the first option.

Step 3b: Image analysis - extract all coordinates

Once all the parameters have been optimised for the image series, run `findcoord_2d.pro` with these settings for the full image series by increasing `iend` and make sure to save the data in a proper location. However, sometimes this is the step where you realize that the selected parameters were not properly chosen and you should repeat the optimisation procedure of step 3a.

Figure 4.5 shows the brightness histogram and particle cloud for the full analysis of the 4000 images with `minarea` properly set, showing that a large part of the particles is now excluded.

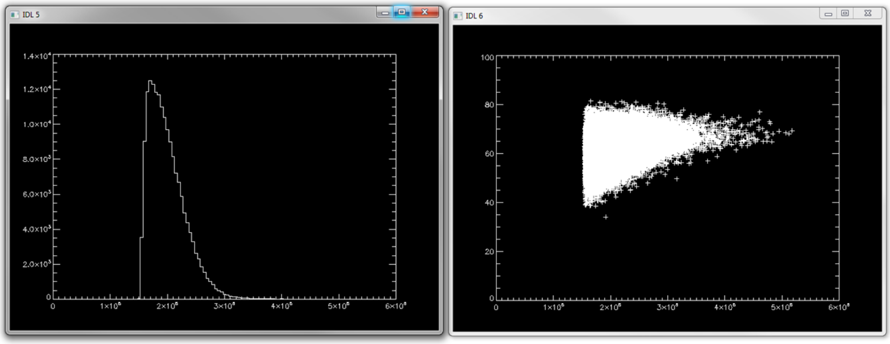

Figure 4.5: IDL output of full series analysis for brightness histogram and particle cloud where the minarea is properly set.

Step 4: Analysis of the coordinates

Pair correlation function - `gr_2d.pro`

The pair correlation function or radial distribution function, $g(r)$, is a probability density function for finding a particle at a certain distance r from a reference particle positioned at $r = 0$ and thus informs you about the structural ordering and interaction in the system studied. In practice the $g(r)$ curve is extracted by calculating the number of particles within thin shells of thickness Δr around each particle. Figure 4.6 shows the schematic representation of a concentrated liquid of hard spheres with diameter σ together with the expected $g(r)$ curves. Here several things can be observed:

> For $r < \sigma$, $g(r) \rightarrow 0$ because it is physically impossible for particles to overlap.
>
> At $r \approx \sigma$, a sharp peak is found originating from the first shell of particles that cannot inter-penetrate the centre particle.
>
> At $r \approx 2\sigma, 3\sigma ... n\sigma$, peaks are observed that related to the other shells of particles around the centre particle, n depends on concentration and/or interactions between the particles.
>
> At $r >> \sigma$, $g(r) \rightarrow 1$, as there are no interaction over such large distances in a liquid and the probability to find a particle at exactly this position is high.

Figure 4.6 shows a confocal image of a layer in a crystal with the corresponding the $g(r)$ curve. In this case many sharp peaks are observed that are related to the hexagonal order in the layer. As a crystal possesses long-range order we still observed peaks in the $g(r)$ curve for $r >>> \sigma$.

As input `gr_2d.pro` requires the coordinate file (*_crd.gdf) you have created with `findcoord_2d.pro`. The procedure will create a single averaged $g(r)$ for all the coordinates from each of the images from the series. This will be saved as a *_gr.gdf and *_gr.dat file and saved in the same folder as the input data. The procedure will also open a window in which it will show the process of averaging the $g(r)$ curve and in the end the final $g(r)$. The quality of the $g(r)$ depends on the accuracy of your coordinates but also on the statistics, especially at low concentration, you will need to take image series of many images, i.e. ~ 4000-10000 or even 20000, to get enough statistics.

The input parameters that have to be adjusted are:

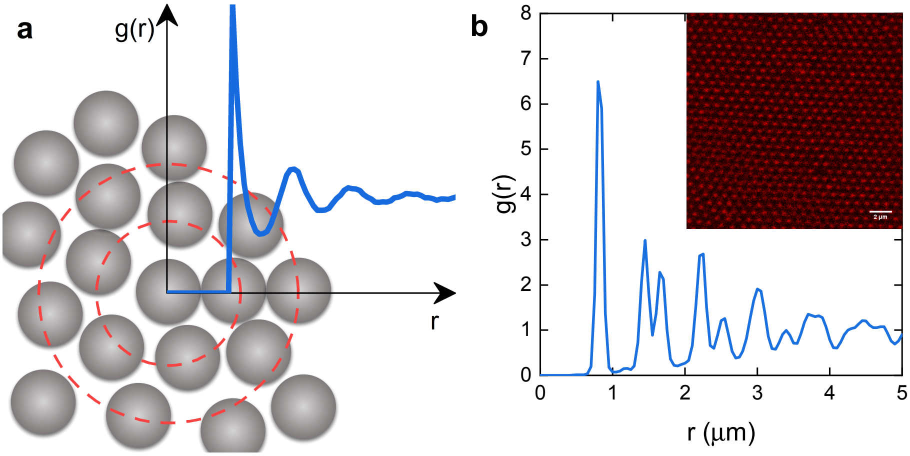

Figure 4.6: $g(r)$ for liquid with short-range order (panel a) and for crystal, showing long-range order (panel b).

- `rmin = 0`. Minimum r (in μm) of the $g(r)$ curve. Usually set to 0.
- `rmax = 5`. Maximum r (in μm). Typically set to half of the size of your image because statistics at higher r are low. A good indication of a too large distance is when the $g(r) \rightarrow 0$ at large r.
- `deltar = 0.05`. Δr (in μm). Typically set to $0.1\times$ pixel size in μm or in the case of bad sub-pixel resolution you can use $0.5\times$ pixel size.
  If this value is set unreasonably low, you will introduce artificial noise in the $g(r)$ curve. If it is set too high, you lose information and smooth out the graph. It is also important for proper comparison between image series to use the same Δr (relative to pixel size), which of course also requires you to take the images with the same resolution.

Figure 4.7 shows the output window of the `gr_2d` for the previously discussed image series of a fluid.

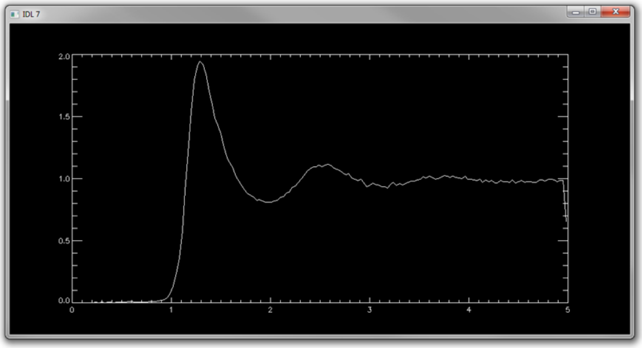

Figure 4.7: IDL output for $g(r)$ calculation of a fluid.

Particle tracking - `track_2d.pro`

This section will describe how to use the particle tracking procedure `track_2d.pro` that will track the particles between the different images to create particle tracks. The procedure uses the coordinate file '*_crd.gdf' you have created with `findcoordinates_2d.pro`. The output data will be saved in the same folder as the input data. The output for this procedure will produce a '*_tracked.gdf' file and open two windows. Figure 4.8 shows the two windows with left: the found probability for a particles to move a distance Δr between successive images and right: identified particle tracks.
The `track_2d` procedure has the following parameters:

- `maxdist = 0.7`. Maximum distance between particle coordinates in successive images to be considered the same particle and be tracked as the same. Simply stated, the distance a particle is 'allowed' to move between images.
  A good estimate is $\frac{3}{4}r$ of the first $g(r)$ peak. The value can be checked by looking at the left window. If the curve goes to 0 before it reaches the set `maxdist`, it is good. If it doesn't go to 0 increase `maxdist` or if the probability shows a plateau decrease `maxdist`. If it is set too high, the procedure will 'paste' tracks together.
- `goodenough = 2`. Minimum track length any tracked particle needs to have in order to be taken into account. In this way very short track lengths are excluded.
- `memory = 0`. Number of images a particle can disappear but still be considered the same particle after returning at the same place. For a liquid it should be set to 0. For a crystal plane in which particles sometimes move out of focus it can be set high.

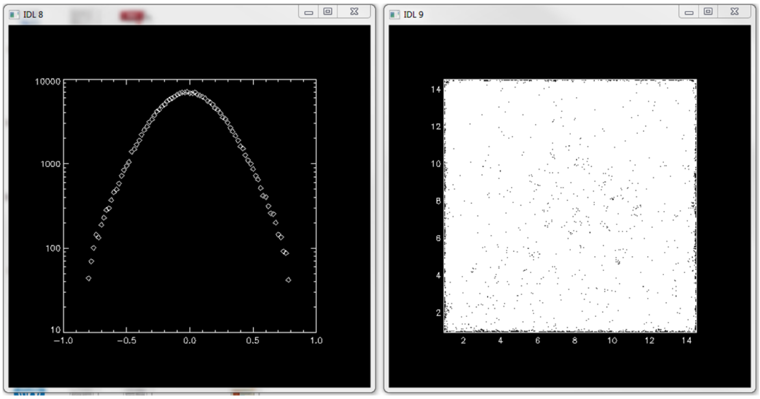

Figure 4.8: Left: found probability to move a distance Δr between images. Right: plot of identified particle tracks.

Correcting drift during imaging - `dedrift_2d.pro`

This is a procedure that should only be used when you notice during `track_2d.pto` that the particle tracks show slow drifting (collective motion) of the sample. This procedure allows you to correct the constant drift. The procedure determines the average displacement in x and y over the time-series and then corrects the x- and y-coordinates for each image. The procedure will produce a '*_tracked_corr.gdf' file and open three windows, as shown in Figure 4.9. The windows show the original tracks, the drift in x and y per image together with a smoothed curve for each, and the corrected tracks.

In the procedure you can change only two parameters:

- `sm_size = 30`. The drift in x and y can be quite noisy per frame as the particles move due to the Brownian motion of the particles. If you would just take the average motion in each frame to dedrift your image stack you will introduce additional noise. Instead, as the drift usually is a slow continuous process, the correction value is determined by smoothing the drift in x and y over several frames, as determined by the `sm_size`.
- `good = 5`. Set this value to show only tracks with a length > `good` in the two track windows. This is useful for image series with a large number of tracks in which the individual tracks overlaps making the assessment of the success of the dedrifting procedure difficult.

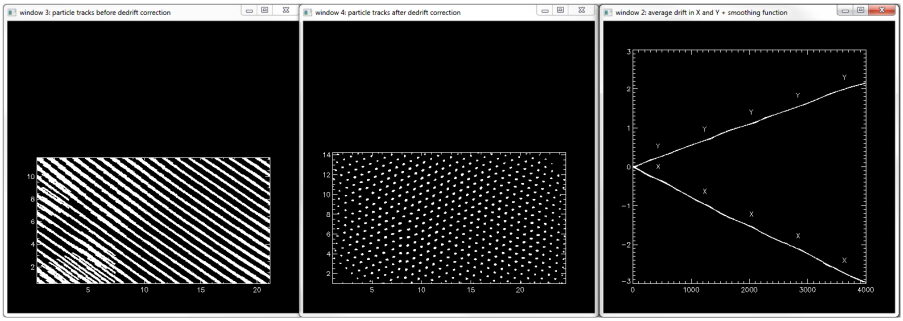

Figure 4.9: From left to right: particle tracks before (left) and after (middle) dedrifting, average motion in x- and y-direction plotted per frame + the smoothed function used to apply dedrifting (right).

Mean square displacement - `msd_2d.pro`

After particle tracking and possible correction for drifting, the mean square displacement can be calculated from the tracked trajectories. This section describes the procedure `msd_2d.pro`, which requires the tracked or corrected dataset '*_tracked.gdf' or '*_tracked_corr.gdf' and the time step '*_tstep.dat' file as input. It will produce an output file '*_msd.dat' and one window in which the calculated msd is plotted as shown in Figure 4.10.

It has the following input parameters:

- `dedrifted = 'no'`. Indicate whether you have used the `dedrift_2d.pro` procedure. If set to 'yes' it will use '*_tracked_corr.gdf' and the output will be saved as '*_msd_corr.dat'.
- `maxframe = 20`. This is the maximum number of time steps to calculate, i.e. this depends on your average trajectory length. Usually you only have a few extremely long particle tracks. You can always set this very high and then decide your own cut off value later. The procedure will automatically stop calculating when it does not have enough statistics, this threshold is quite stringent.
- `;timestep = 0.036`. This parameter can be set to define the time step between frames in seconds. This should be turned on (by removing ;) in case the '*_tstep.dat' file is missing. When `findcoord_2d.pro` was used this is automatically created from the overhead data stored in your tiffstack made using the Bio-Formats plugin and ImageJ.

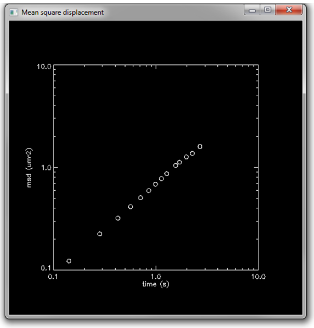

Figure 4.10: Mean square displacement for analysed fluid image series

5 | Troubleshooting

Many times during a compilation IDL will produce errors. Usually it will specify exactly in which line the error was found and you can click the error and you are immediately taken to the part of the script where the error is present. Often the error is a result from a mistake in your code several lines up. Typical mistakes are:

- `syntax error`: eg. on line `im = bpass(aa,noise,diam)`. In this case, IDL does not recognise the Crocker & Grier subroutine `bpass` as a procedure. Cause: subroutines have not been added to the IDL library or wrong working directory.
- `No files matched specification`: There is an error in the filepath or filename you specified. Did you use spaces or make a typo?
- `Attempt to call undefined procedure`: You are trying to call a procedure that IDL cannot find. Possible causes: wrong working directory, procedure not in the IDL path, or a typo and you were not even trying to call any procedure.
- `Variable is undefined`: A variable that is called upon has not been defined by the user. This can be the result of a typo (most often), or wrong working directory/IDL path.
- `No features found! Attempt to subscript PNTS with <INT ( 1)> is out of range`: Typical error in `findcoordinates_2d.pro`. The procedure did not find any features because your selection criteria are too strict. Try again using 'easier' settings.

Sometimes the message `Illegal floating point operation: divide by zero` is displayed after the procedure is finished. In practice, this does not affect your analysis.

The provided information above should allow you to execute the confocal image analysis procedures and to fix some of the problems that you will encounter. In addition, we have tried to intercept many of the problems that you can encounter by providing an additional error message in the console window that informs you what the problem is and how to fix it.

6 | Further reading

This guide is aimed at providing the absolute basics in 2D image analysis. If you would like to learn more, we recommend the following resources:

- the online tutorial of Crocker and Grier managed by Weeks at http://www.physics.emory.edu/faculty/weeks//idl/tracking.html
- the online resources on particle tracking but also microrheology provided by Savin at http://web.mit.edu/savin/Public/.Tutorial_v1.2/
- the (first part of the) paper by Jenkins and Egelhaaf about how to get the best data from the confocal and how the image analysis in IDL works.

  M. C. Jenkins and S. U. Egelhaaf, 'Confocal microscopy of colloidal particles: Towards reliable, optimum coordinates', Advances in Colloid and Interface Science, 136, (2008), 65-92.
- the paper by Savin, Spicer and Doyle on the particle cloud and how to select in-focus particles.

  T. Savin, P. T. Spicer and P. S. Doyle, 'A rational approach to noise discrimination in video microscopy particle tracking', Applied Physics Letters, 93, (2008), 024102.
- the paper by Savin and Doyle on how different types of experimental error will affect the resultant mean squared displacement.

  T. Savin and P. S. Doyle, 'Static and Dynamic Errors in Particle Tracking Microrheology', Biophysical Journal, 88, (2005), 623-638.

- the (first part of the) paper by Mohanty *et al.* on how 2D $g(r)$s are affected by out-of-focus particles and why they should be discarded.

  P. S. Mohanty, D. Paloli, J. J. Crassous, E. Zaccarelli and P. Schurtenberger, 'Effective interactions between soft-repulsive colloids: Experiments, theory, and simulations', Journal of Chemical Physics, 140, (2014), 094901.

The effect of microscopic colloid interactions on the resultant macroscopic phase behaviour is a frequently studied topic in soft matter resarch, and lies at the heart of this thesis. Key structural and dynamic properties of colloidal model systems across liquid-solid transitions are tracked using optical imaging techniques.

The first studied system comprises of thermosensitive microgels. These are soft, crosslinked polymer networks of colloidal size, which have been used as model systems to investigate various phase transitions. They display a rich phase behaviour due to their soft potential and internal core-corona structure. Especially, their thermosensitivity allows us to use temperature as an external control to tune particle size, volume fraction and effective interaction potential in situ. However, a thorough understanding of the effective interactions between microgels is lacking, and constitutes a key research question in this thesis.

We therefore quantitatively compare experimental and numerical pair correlation functions (g(r)s) across the phase diagram, obtained from confocal microscopy and simulations. We find that neutral, swollen microgel interactions are temperature-dependent, but also hinge on whether the core or corona of the microgel is explored.

This approach is repeated for ionic microgels with varying crosslinker density, where the introduction of acrylic acid complicates the resultant swelling behaviour. For this reason, we start by decoupling the core and corona swelling response to various charge regimes via light scattering experiments, and found that dangling polymer strands can extend up to several 100 nm outside of the network. Dangling ends had a pronounced effect on the interactions and phase behaviour of ionic microgels, but their contribution is missing within the current theoretical framework.

Finally, liquid-solid transitions in concentrated protein solutions are investigated. Two well studied globular proteins, lysozyme and γB-crystallin, were used as model systems with completely different interactions. No unambiguous experimental demonstration of the existence of an arrested glassy state had been published so far for either protein. A combination of two passive microrheology techniques now allowed us to confirm the formation of a glass phase at concentrations above a critical arrest concentration, and to obtain quantitative insight into the concentration dependence of the zero shear viscosity prior to arrest.

Printed by Media-Tryck, Lund 2019 NORDIC SWAN ECOLABEL 3041 0903

LUND UNIVERSITY

ISBN: 978-91-7422-626-3

Physical Chemistry
Faculty of Science
Lund University

9 789174 226263